7   STORAGE RING SYSTEM

7.1   Storage Ring Magnets

7.1.1   Parameters and Tolerances

The DBA (15×2) lattice consists of 60 dipole magnets with uniform magnetic field and a maximum field of 4 kiloGauss at 3.0 GeV. The dipoles are planned to be run in series with a common power supply. The ring quadrupoles consist of a total of 360 magnets with two different lengths: 30 and 40 cm. These quadrupoles have a maximum gradient strength of 21 T/m at 3.0 GeV. The quadrupoles are individually powered, but the current lattice design assumes 10 families. With an undulator or wiggler installed in a straight section, the pair of four quadrupoles in the ID straight will be used to adjust locally for the tune shift and beta-beat modulation induced by the undulators. This was shown in Chapter 6 to be quite useful in reducing the impact of the IDs on the dynamic aperture of the ring and improving the lifetime and injection efficiency. The four dispersion-region quadrupoles are tuned as two families in the design, but the individual power supplies on each quadrupole will allow tuning out any dispersion beating resulting from differences between the dipoles. With the dispersions below 5 mm (H) and ~1 mm (V), the DW reduction in emittance will be within 10% of the expected values and will decouple energy modulation from the user's x-ray beam.

The sextupoles include 390 magnets with three different lengths: 20, 25, and 30 cm (Table 7.1.1). However, for most tunes found so far, the 25 cm sextupoles could be replaced by 20 cm sextupoles, saving some space for other components. Also, some tunes show that some sextupoles are running at quite low values. These may be eliminated in future designs, but the extra knobs have proven useful for now. The sextupoles are individually powered but the design tuning has assumed 11 families of sextupoles.

Table 7.1.1   List of Storage Ring Magnet Parameters at a 3 GeV Beam Energy, with Basic Tolerances.

Qty.	Magnet Type	Length [m]	B, B', B" [T,T/m,T/m²]	Field Tol.	Alignment Tol.
60	Dipole	2.62	0.4, 0, 0	0.01%	0.1 mm, 0.5 mrad
330	Quadrupole (S)	0.30	0, 21, 0	0.02%	0.03 mm, 0.2 mrad
30	Quadrupole (L)	0.40	0, 21, 0	0.02%	0.03 mm, 0.2 mrad
30	Sextupole (L)	0.30	0 , 0 , 500	0.05%	0.03 mm, 0.2 mrad
120	Sextupole (M)	0.25	0 , 0 , 500	0.05%	0.03 mm, 0.2 mrad
240	Sextupole (S)	0.20	0 , 0 , 500	0.05%	0.03 mm, 0.2 mrad
120	H & V	0.35	0.03, 0		0.1 mm, 0.02 mrad
30	H & V	0.25	0.03, 0		0.1 mm, 0.02 mrad
30	H only	0.25	0.03, 0		0.1 mm, 0.02 mrad
30	H & V & SQ corrector	0.25	0.03, 0.36, 0		0.1 mm, 0.2 mrad
≤20	Fast H & V corrector	0.20	0.01, 0		
150	Magnet girders				0.1 mm, 0.5 mrad

The alignment and field tolerance errors are still being studied. However, initial testing of the lattice with tolerance that has been achieved at other light sources has shown the DA is robust for individual errors. As with most synchrotrons, the **c**losed-**o**rbit **a**mplification **f**actors contribute the most significant tolerance to be handled. COAFs give the RMS closed-orbit distortion around the ring per unit of RMS alignment error (assumed to be a random Normal distribution) for all the quadrupoles in the ring. The COAF for this lattice is shown in Figure 7.1.1 for one cell and has an average value in each plane of greater than 50. This means a 100

μm RMS alignment error in the quadrupoles will yield an average closed-orbit distortion of >5 mm. This closed orbit error in the sextupoles contributes to a nonlinear focusing error in the lattice, which breaks the sextupole strength settings that yield the large DA.
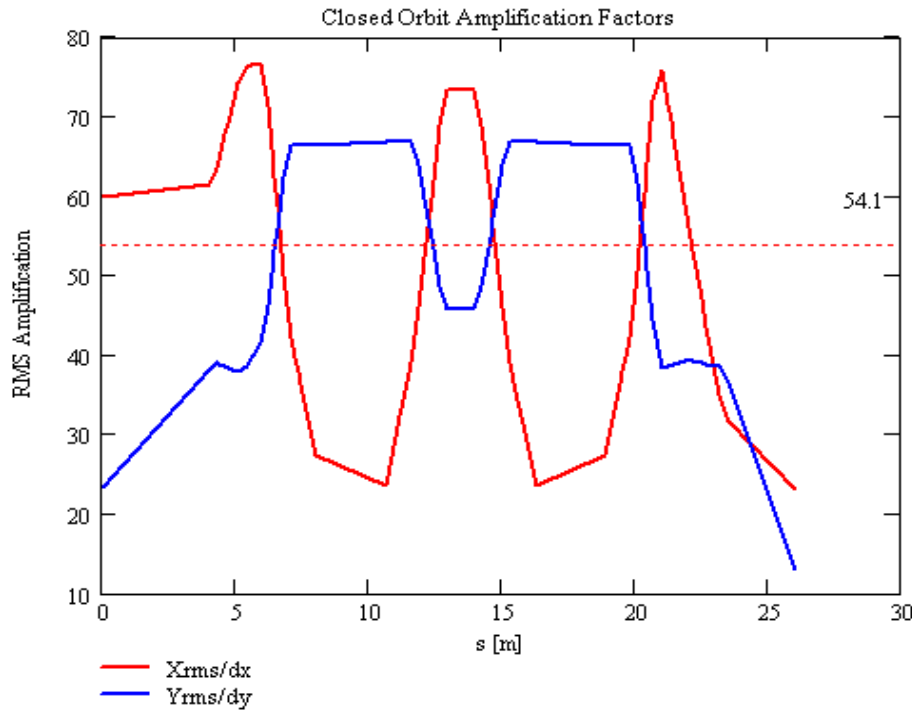

Figure 7.1.1 RMS expected closed-orbit amplification factors for random alignment errors in the quadrupoles of the lattice.

Figure 7.1.2 shows the impact of random quadrupole alignment errors of 100 μm with correction to the BPMs located close to the high beta-function quadrupole magnets. We have corrected the orbit to the BPMs with an assumed ideal Beam-Based Alignment. The DAs for 20 different starting seeds for the random alignment offsets are shown. The DA remains adequately large and is more than sufficient for injection and lifetime.
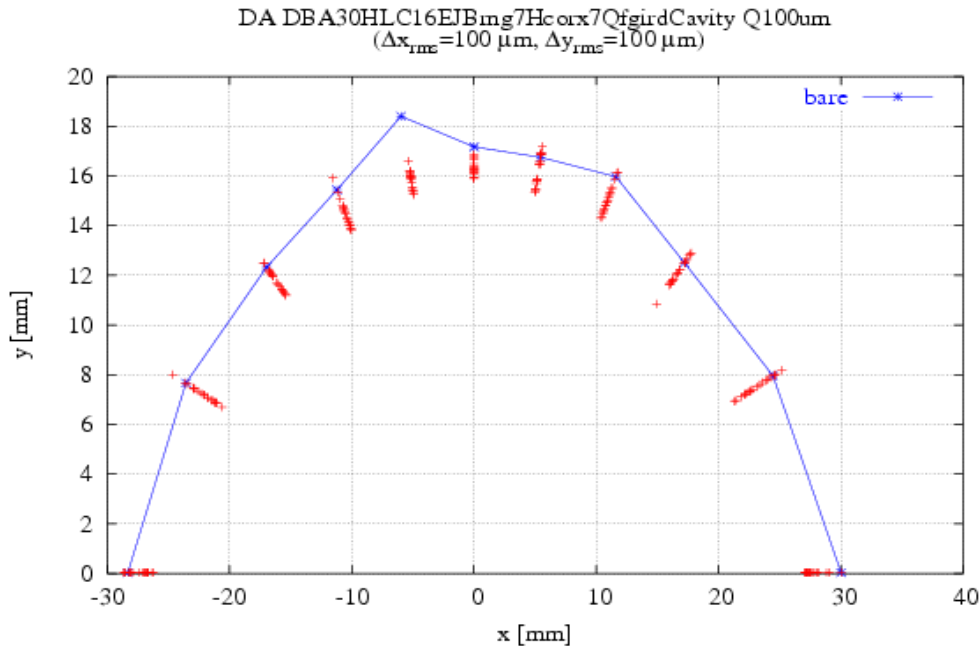
DA DBA30HLC16EJBrng7Hcorx7QfgirdCavity Q100um
(Δx_{rms}=100 μm, Δy_{rms}=100 μm)

Figure 7.1.2   DA with 100 μm quadrupole alignment tolerances corrected with ideal BBA (zero relative alignment error) BPMs located at the quadrupoles. Each point represents the DA for one of 20 seeds (sample lattices). It includes synchrotron oscillations, and is for 2 K turns around the lattice.

Adding a 30 μm random alignment tolerance of the BPM-to-quadrupole magnetic center yields little additional reduction of the DA, as shown in Figure 7.1.3, and is more than adequate. This random offset of the BPMs is equivalent to a BBA resolution of the BPM center relative to the quadrupole magnetic center, which could be much better than the 30 μm assumed in Figure 7.1.3, as described below.
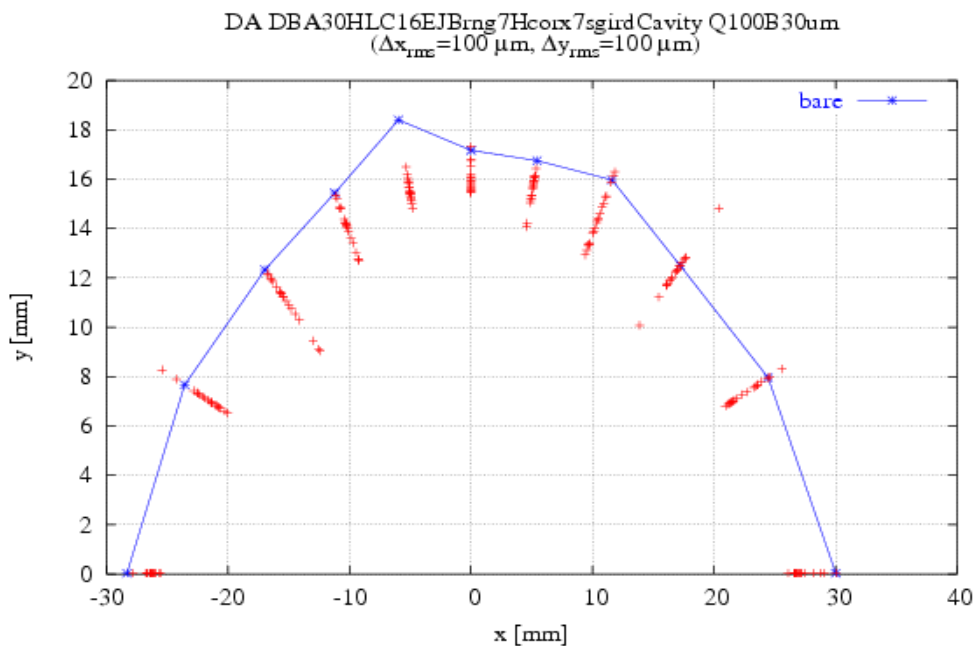
DA DBA30HLC16EJBrng7Hcorx7sgirdCavity Q100B30um
(Δx_{rms}=100 μm, Δy_{rms}=100 μm)

Figure 7.1.3   DA with 100 μm quadrupole alignment tolerances corrected with 30 μm BBA tolerance for BPMs (20 random seeds shown, with synchrotron oscillations).

We have assumed that the BPMs are close to the quadrupoles, since they are the source of the closed-orbit distortions in the sextupole magnets that cause the reduction of the DA. The two BPMs on a girder are aligned to the centers of the neighboring quadrupole magnetic center using the BBA procedure, which has become common at many synchrotrons. This method uses a beam bump to vary the beam position (x, y) in the quadrupole and its neighboring BPM. If that quadrupole has its strength modulated (ΔK_2), then the magnitude of the closed-orbit distortion measured by the BPMs is (X_m, Y_m). The BPM reading that yields a null in (X_m,

Y_m) is then the magnetic center of this quadrupole, as measured by the BPM. With two BPMs on a girder, the beam can be magnetically centered to all elements on the girder using the magnetic alignment instruments: pulsed wire, vibrating wire, and/or rotating coils. Therefore we specify the alignment tolerances for the magnetic elements in terms of: 1) an alignment tolerance of centers one to another, 2) alignment of girder ends one to another and a common roll error of the girder, and 3) a BBA alignment tolerance of the BPMs to their neighboring quadrupole. The sensitivity of the closed-orbit distortion amplitude to the quadrupole modulation ($\Delta K_2 L$) and beam offset relative to the quadrupole center position, (x_c, y_c), is given by:

$$X_m(s) = \frac{\sqrt{\beta_x(s)\,\beta_x(quad)}}{2\sin(\pi Q_x)} \left(\Delta K_2\, L\right) x \geq 5.2 \left(\Delta K_2\, L\right) x$$

(7.1.1-1)

and

$$Y_m(s) = \frac{\sqrt{\beta_y(s)\,\beta_y(quad)}}{2\sin(\pi Q_y)} \left(\Delta K_2\, L\right) y \geq 7.2 \left(\Delta K_2\, L\right) y$$

(7.1.1-2)

where we assume the smallest beta function at a quadrupole and the average beta function at the BPMs. We assume that the closed-orbit amplitude is measurable to the resolution of the BPMs, ~1 μm, and the modulation is 3% of the quadrupole strength; the magnetic center should be measured in the neighboring BPM with an accuracy of better than

$$\sigma_{xc} \leq 8\, to\, 10\, \mu m \quad and\, \sigma_{yc} \leq 15\, \mu m\,.$$

(7.1.1-3)

Consequently, the random tolerances on the magnet-to-magnet alignment in Table 7.1.1 will be greater than the BBA resolution. However, we have assumed the BBA resolution of 30 μm in Figure 7.1.3, which is two to three times greater than achievable.

The impact of the larger values for the girder alignment tolerances were evaluated assuming that either end of the girder is aligned to an RMS level (random Normal distribution Δx, Δy). This misalignment of the girders contributes a correlated misalignment error in all magnets and BPMs on the girder. The sensitivity to this type of error is shown in Figure 7.1.4, where the Girder Amplification Factor is shown. The GAF is defined as the RMS closed-orbit distortion per unit of RMS girder misalignment. This shows a reduction in the averaged COAF (Figure 7.1.1) by a factor of 4X (H) and 5X (V). The GAF values at the center of the short straight section are 4.8 in the horizontal and 2.3 in the vertical plane, compared to 22.5 and 12.0 for the COAF, respectively. However, correcting for the assumed 100 μm girder alignment tolerances yields almost complete restoration of the DA (without BPM errors), since the correlations of the quadrupole misalignments are easier to remove by BBA alignment to the quadrupoles on the misaligned girders.
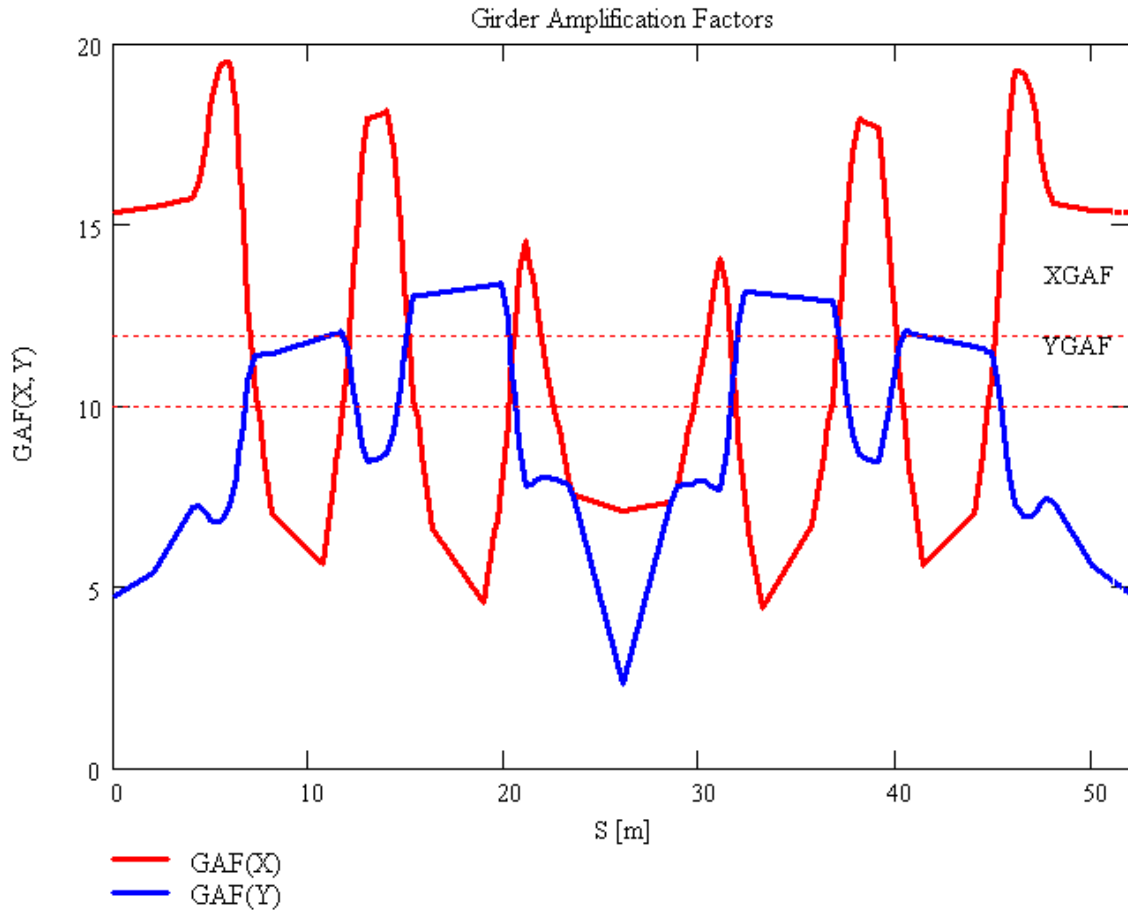
Figure 7.1.4   Girder Amplification Factors for one period of the storage ring. The average GAF values are 12 (H) and 10 (V).

The corrected DA is shown in Figure 7.1.5 for 100 µm RMS random girder alignment tolerances, where no other errors are assumed in the BBA resolution for the BPMs, nor for quadrupole misalignments on the girder. The complete analysis of the DA with all alignment and field tolerances is presented in Section 61.2. The COAF and GAF presented here will also be used to estimate the orbit stability resulting from magnet vibrations in Section 7.2.2.
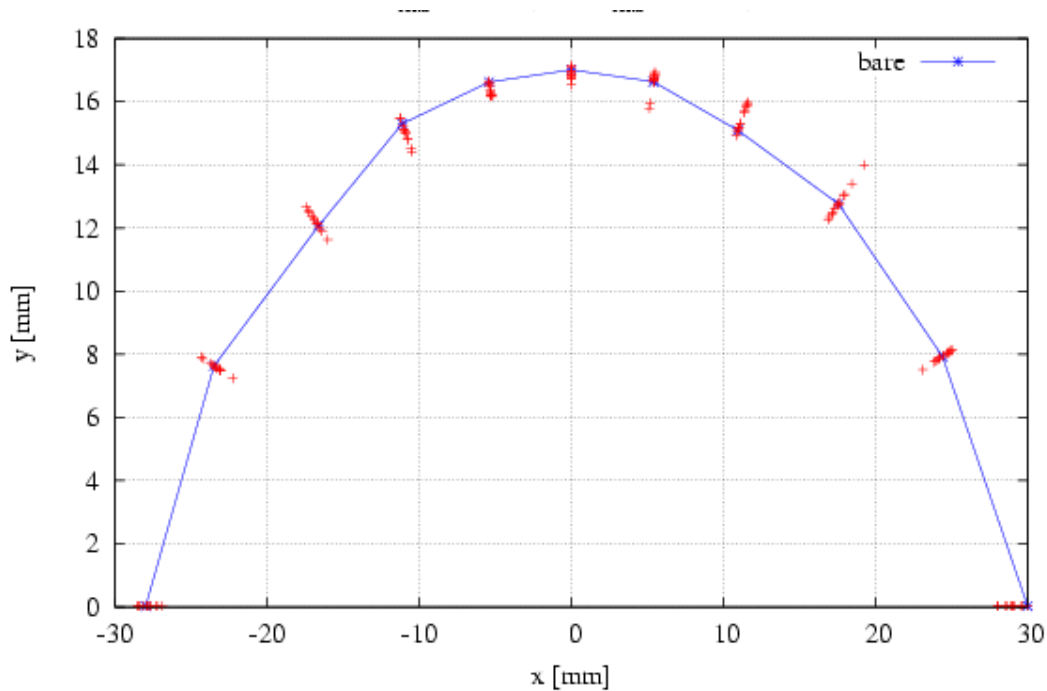
Figure 7.1.5 DA for 10 seeds (lattices) with 100 µm RMS girder alignment tolerances corrected using the BPMs with zero error in the BBA resolution.

7.1.2   Conceptual Magnet Design

7.1.2.1   Storage Ring Lattice Magnet Design Considerations

The magnet lattice is designed with a 30 superperiod DBA (double bend achromat) structure for a machine with 3.0 GeV full-energy top-off injection and a beam emittance of 0.5 nm-rad. The 780 m storage ring will contain 1,040 magnets. This quantity is comprised of 60 bending dipoles, 360 quadrupoles, 390 sextupole magnets, and 230 corrector magnets. To ensure acceptable dynamic aperture for the electron beam, the required magnetic field and alignment tolerances are the two primary considerations in the design. All the dipole magnets are connected in series and are energized by a single power supply. Individual trim power supplies will be used to provide 1% field adjustment. All quadrupoles and sextupoles will be individually powered. Storage ring magnets are summarized in Table 7.1.2.

Table 7.1.2 Storage Ring Magnet Specifications at 3.0 GeV.

| | Dipole | | | | Slow | Fast |
	35 mm	63 mm	Quadrupole	Sextupole	Corrector	Corrector
Number of units	50	10	360	390	210	<20
Bending angle [deg]	6	6	0	0	±0.07	±0.01
Clear bore aperture [mm]	35	63	55	64	150	150
Dipole field [T]	0.4	0.4	0	0	0.04	**0.01
Field gradient [T/m]	0	0	21	0	*0.36	0
Sextupole field [T/m^2]	0	0	0	500	0	0
Field quality in GFR - 20x40 [mm]	1×10^{-4}	1×10^{-4}	2×10^{-4}	5×10^{-4}	1×10^{-3}	1×10^{-2}
Nominal operating current [A]	360	360	108	182	20	20
Cooling type	water	water	water	water	air	air
Maximum temperature rise [°C]	10	10	10	10	20	20

*Skew quadrupole component, 30 each required

** At 100 Hz

In this section, we present designs of the individual magnets. Optimization and refinements will occur during the next phase of detailed design.

The following paragraphs in this section present a partial list of lattice magnet design considerations. For the conceptual design these considerations are global in nature and will evolve into specific design parameters for the next phase of preliminary or "reference" design.

The average current density in the coil cross-section of the storage ring magnets was selected to be less than or equal to 2 A/mm^2.

Deionized water will be used to limit the magnet coil temperature rise to within 10ºC, with a pressure drop across each magnet of less than 4 bar.

The NSLS-II storage ring multipole field quality and alignment requirements preclude the use of multifunctional sextupoles; therefore, only discrete corrector magnets are used in the storage ring. However, the corrector magnets are designed to be multifunctional.

The magnetic alignment requirements of the multipoles exceed those of achievable assembly tolerances. Therefore, these magnets are aligned magnetically and then fixed to a rigid girder for installation in the storage ring tunnel.

The storage ring magnet reference designs are being developed to minimize fabrication costs, provide high operational reliability, and minimize the power consumption by individual components as well as overall magnet systems.

To assure magnetic field quality and stable alignment it is necessary to produce a reference design that will be an extremely accurate, stable, and robust mechanical assembly.

The supports for the multipoles will be optimized to reduce vibration amplification.

Methods will be developed to precisely monitor magnet position in the tunnel and assure the required multipole magnetic alignment, despite environmental effects such as variations in tunnel temperature and local tunnel settling.

The detailed design will address a low-cost yet reliable means to integrate the multipole magnets into a vibrating wire magnet-to-magnet alignment system and a means to transfer magnetic field center locations precisely to survey targets on the magnet girder.

Handling and rigging safety issues for magnet testing and installation personnel will be addressed and the reference design will comply with BNL's Critical Lift Policy.

Electrical and all other safety issues will be addressed in the next phase of design. The design of the magnets, the power cabling from the magnet-to-cable connections on the girders, and the magnet instrumentation and controls will be fully NRTL compliant.

We anticipate further optimization of magnetic length and increase in drift space between the multipoles to accommodate corrector magnets without altering the lattice.

Electrical, magnetic, and mechanical design optimization will be performed for the reference design of the relatively low-field-strength 0.4 T dipole magnet to assure high field quality requirements for the C-type magnet cross-section.

3D magnetic modeling will be performed to determine what level of effect, if any, the ramping of the NSLS-II booster ring may have on the magnetic fields of the storage ring magnets. The results of this modeling study will be appropriately incorporated into the reference designs for the storage ring and booster ring magnets.

Extensive 3D modeling and design optimization is anticipated for both the 21 T/m gradient quadrupole and the 500 T/m^2 gradient sextupole to assure high field quality and extremely critical alignment requirements for both multipoles while accommodating the synchrotron's x-ray extraction lines and the vacuum chamber, as well as to minimize or eliminate the effects of crosstalk between neighboring magnets and correctors.

These design concepts and considerations will be refined by both the Laboratory and Industrial resources during the next phase of design, resulting in a preliminary or "reference" design. The final magnet design will be developed by the magnet manufacturer and approved by the Laboratory.

First-order 2D magnetic modeling, as well as mechanical fabrication and assembly methods, have been studied, resulting in conceptual magnet designs that are shown in the following sections.

7.1.2.2   Dipole Magnet Conceptual Design

### 7.1.2.2.1   Scope and Physics Design Parameters

A unique attribute of NSLS-II is the use of dipole magnets with two different size apertures. This requirement is necessary to accommodate a significant and growing community of users that require lower energy infrared and THz radiation. To serve this important community, a 63 mm aperture concept has been chosen, to allow the extraction of long-wavelength light from the dipole magnet [7.1.1, 7.1.2].

The NSLS-II storage ring will be equipped with 10 dipole magnets having a gap of 63 mm, and 50 dipoles having a gap of 35 mm. Each dipole will have a magnetic length of 2.62 m with a field 0.4 T at an electron energy of 3.0 GeV. The radius of curvature of the bending magnet is 25 m; it bends the electron beam 6.0° with a sagitta of 35 mm. The dipole magnets are C-type with a curved laminated flux return yoke (Figure 7.1.6).

Investigations of beam dynamics have established that the good-field region accommodates the dynamic aperture. The designed magnetic cross-section will accommodate the vacuum chamber with a 1 mm clearance between the magnetic poles and either side of the vacuum chamber.

Calculations of the magnetic field were made to optimize the pole contours and the quality of the magnetic field, which for a dipole magnet must have a field nonhomogeneity of $\Delta B/B \leq \pm 0.01\%$ over a good-field region of 40×20 mm.

Figure 7.1.6
Ring Dipole Flux
model.
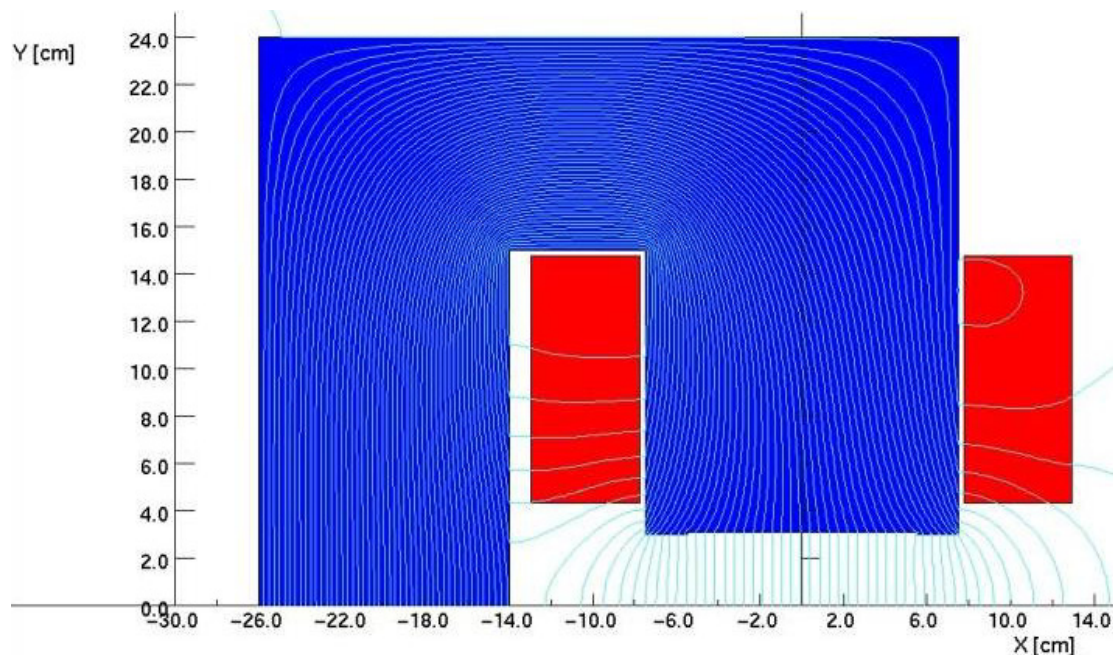
The storage ring dipoles are designed so that both aperture magnets may be connected in series with a single power supply. Minor differences between the two aperture magnets shall be corrected by independently powered trim coils located on each dipole The ten large aperture dipoles will be installed into the storage ring in pairs; each pair shall comprise the adjacent bending magnets in a single cell, and there will be five cells equally distributed around the storage ring.

A list of the conceptual design dipole parameters is found in Table 7.1.3.

Table 7.1.3   Dipole Magnet Conceptual Base Line Design Parameters

	Storage Ring 35 mm Dipole	Storage Ring 63 mm Dipole
Number of units	50	10
Energy [GeV]	3.0	3.0
Bending angle [deg]	6	6
Clear bore aperture [mm]	35	63
Dipole field [T)	0.4	0.4
Field quality	1×10^{-4}	1×10^{-4}
Good-field region [mm]	40 x20	40 x20
Magnetic length [mm]	2,620	2,620
Nominal operating current [A]	360	360
Number of Ampere-turns	11,520	20,160
Number of turns / magnet	32	56
Total Inductance of the magnet [mH]	13	38
Current density in conductor [A/mm²]	3.5	2.4
Max. temperature rise [°C]	10	10
Max. pressure drop [bar]	4.0	4.0
Voltage/magnet	11.4	14.5
Nom. power per magnet [kW]	4.2	5.4
Iron length [mm]	2,585	2,557
Lamination thickness [mm]	1.5	1.5

7.1.2.2.2   Mechanical Design of the Dipole

Fabrication and assembly concepts have been studied, resulting in the magnet design concepts shown in Figures 7.1.7 and 7.1.8.

The laminated magnet yokes are composed of 1.5 mm thick AISI 1006 low-carbon steel sheet. The permeability of the core material deviates by about 5% from the production value. The laminations must be shuffled to ensure a uniform magnetic property.

The coils for the 35 mm dipoles are made up of square hollow copper conductors, 13×13 mm, with an interior diameter of 9 mm. The coils for the 63 mm dipoles are made up of rectangular hollow copper conductors, 13×16 mm, with an interior diameter 8.5 mm. The water channels of the hollow conductor coil pancakes are connected in parallel to provide adequate cooling to maintain the increase in coil temperature to less then 10°C.

Fiberglass that is vacuum impregnated with highly radiation-resistant epoxy exceeding 1.0 mm in thickness will provide interstitial conductor insulation. An additional 1.5 mm (minimum) of vacuum-impregnated epoxy fiberglass will provide ground plane insulation. The magnet will be high-potted up to 5 kV to detect defects in the insulation.

Dipoles of either aperture that are not used as SR sources will use a single dipole vacuum chamber design. The chamber will allow damping wiggler radiation to pass through. The larger aperture IR dipole vacuum chamber will have a minimum internal aperture of 50 mm.
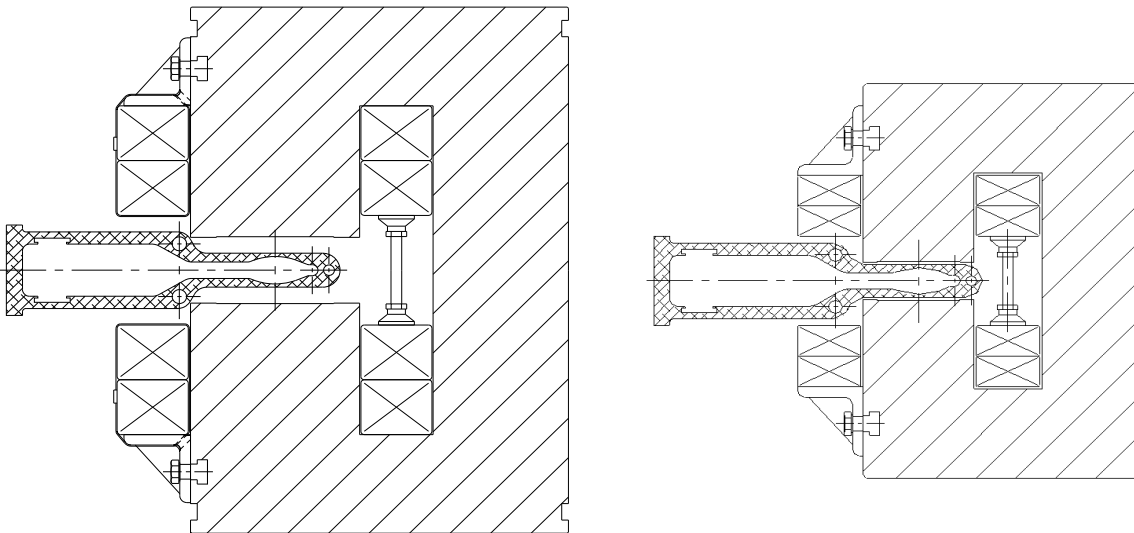

Figure 7.1.7   Storage Ring Dipole cross-sections, aligned on the centerlines, with coil, coil support system, and vacuum chamber. On the left is the 63 mm dipole; on the right is the 35 mm dipole.
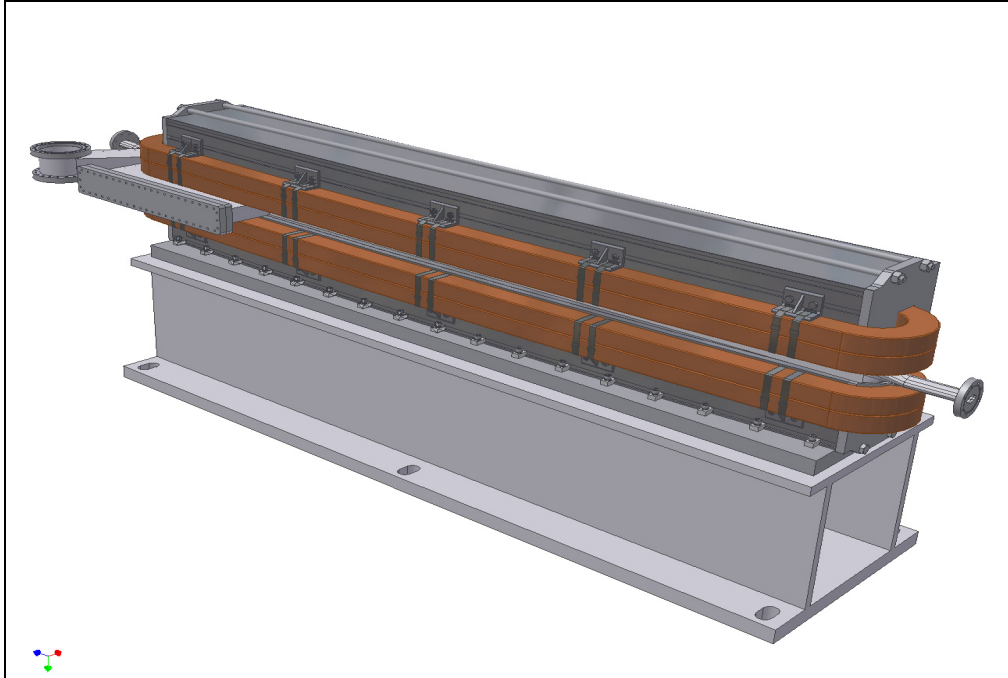
Figure 7.1.8 The 63 mm aperture dipole design concept with an IR beam extraction vacuum chamber installed.

The 60 dipole magnets are connected in series with a single highly stable magnet power supply with low-ripple current. The dipole magnet and its power supply are connected by 650 MCM power cables. The dipole cabling will be designed to avoid loops that could induce errors in the dipole circuit.

7.1.2.3   Quadrupole Magnet Conceptual Design

7.1.2.3.1   Scope and Physics Design Parameters

The storage ring has 360 quadrupole magnets, each with an individual power supply. The field gradient homogeneity in a region 40×20 mm is required to be better than 0.02%. The geometry of the vacuum chamber determines the bore radius of the quadrupole magnet. In modeling studies (Figure 7.1.9), the design of the quadrupole magnet is constrained by the need to accommodate the antechamber of vacuum vessel.
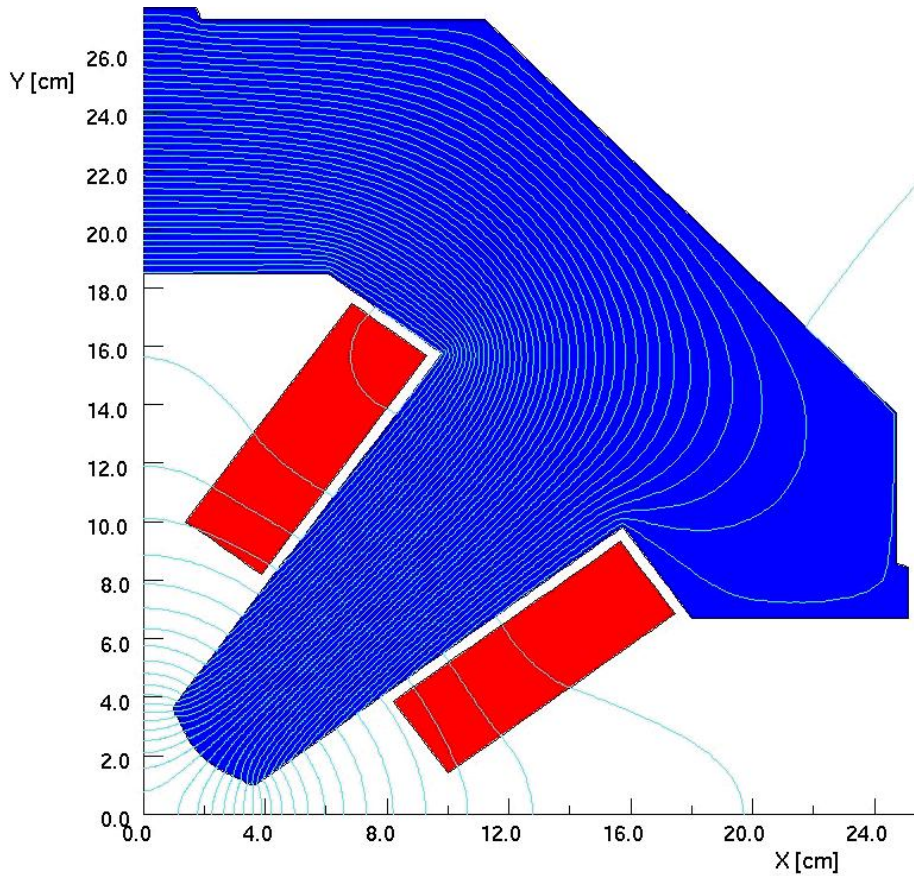
Figure 7.1.9 Quadrupole Magnet Analytical Model.

To provide a path for synchrotron radiation exiting dipoles and insertions devices, the antechamber must extend into the horizontal mid-plane of the magnet yoke. To assure symmetry, the horizontal back leg on either side of the quadrupole has been removed to accommodate the antechamber of the vacuum chamber. Therefore, the top and bottom halves of the quadrupoles are not connected with a flux-return yoke; each half is connected mechanically with nonmagnetic stainless steel spacers accommodating the vacuum chamber. The quality of the gradient in one-quarter of the geometry has been examined. The poles and shims are optimized with a 2D approximation. Further modeling will be done to ensure that the requirements for higher-order multipoles (Table 6.1.9) are met. Figure 7.1.10 presents the mechanical design. Table 7.1.4 lists the conceptual design parameters.
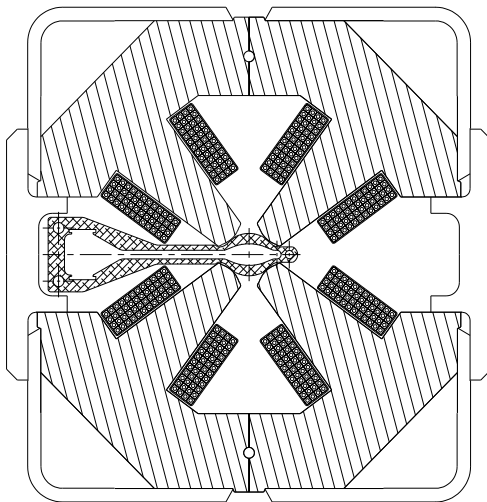

Figure 7.1.10 Conceptual design for NSLS-II storage ring quadrupole magnet cross-section with water-cooled coil and vacuum chamber.

Table 7.1.4   Quadrupole Magnet Conceptual Design Parameters

	30 cm SR-Quadrupole	40 cm SR-Quadrupole
Number of units	330	30
Energy [GeV]	3.0	3.0
Clear bore aperture [mm]	55	55
Maximum field gradient at 3.0 GeV [T/m]	21	21
Field quality	2×10^{-4}	2×10^{-4}
Good field region [mm]	40 x20	40 x20
Magnetic length [mm]	300	400
Nominal operating current [A]	108.2	108.2
Number of Ampere-turns	25,956	25,956
Number of turns / magnet	192	192
Total resistance of the magnet at 30°C [Ω]	0.092	0.112
Total inductance of the magnet [mH]	51.8	68.8
Current density in conductor [A/mm^2]	2.7	2.7
Number of parallel cooling circuits	4	4
Temperature rise [°C]	5	7
Pressure drop [bar]	4	4
Voltage / magnet [V]	9.95	12.12
Iron core length [mm]	245	345
Lamination thickness [mm]	1.5	1.5
Quadrupole alignment tolerance [μm]	30	30

7.1.2.3.2   Mechanical Design of the Quadrupole

The magnetic cores are made of low-carbon steel sheet, AISI 1006, 1.5 mm thick. To install the coil on the magnet the magnet core is divided into four quadrants. A 2 mm (minimum) clearance between the vacuum chamber and the adjacent poles is used to maintain thermal isolation during chamber baking. This gap is maintained to prevent the transmission of vibration from the vacuum chamber. A hollow copper conductor, 7.4×7.4 mm, with a 4 mm diameter water channel, was selected as a base for winding the excitation coils. Fiberglass that is vacuum impregnated with radiation-resistant epoxy at least 1.0 mm thick will provide interstitial conductor insulation. An additional 1.5 mm of vacuum-impregnated epoxy fiberglass will provide ground plane insulation. The magnet will be high-potted up to 5 kV to detect defects in the insulation. Four water channels are connected in parallel to maintain the temperature increase of the coil to be less than 10°C.

7.1.2.4   Sextupole Magnet Conceptual Design

7.1.2.4.1   Scope and Physics Design Parameters

The storage ring is equipped with 390 sextupole magnets, each connected to an individual power supply. The sextupole field homogeneity in a region 40×20 mm is required to be better than 0.05%. The geometry of the vacuum chamber determines the bore radius of the sextupole magnet. The design of the sextupole magnet is constrained by the need to accommodate an antechamber. The sextupole has been designed with three-fold symmetry with one horizontal air gap where the back leg has been removed to accommodate the antechamber of the vacuum chamber. Therefore the three segments of the sextupole are not connected with a flux-return yoke; each triplet is connected mechanically with a stainless steel spacer to accommodate the vacuum chamber.

The poles and shims are optimized with a 2D approximation. Further modeling will be done to ensure that the requirements for higher-order multipoles (Table 6.1.9) are met.

Table 7.1.5   Sextupole Magnet Conceptual Design Parameters.

	20 cm Sextupole	25 cm Sextupole	30 cm Sextupole
Number of units	240	120	30
Clear Bore aperture [mm]	66	66	66
Sextupole field [T/m^2]	500	500	500
Field quality	5 x10^{-4}	5 x10^{-4}	5 x10^{-4}
Good-field region [mm]	40 x20	40 x20	40 x20
Magnetic length[mm]	200	250	300
Nominal operating current [A]	199.7	199.7	199.7
Number of Ampere-turns	28,757	28,757	28,757
Number of turns / magnet	144	144	144
Conductor cross-sectional area [mm^2]	51.3	51.3	51.3
Total resistance of the magnet at 30°C [Ω]	0.0276	0.0324	0.0372
Total inductance of the magnet [mH]	8.6	10.8	12.9
Current density in conductor [A/mm²]	3.9	3.9	3.9
Temperature rise [°C]	7.5	5.1	6.3
Pressure drop [bar]	4	4	4
Voltage / magnet	5.03	5.89	6.77
Iron length [mm]	136	186	236
Laminae thickness [mm]	1.5	1.5	1.5
Sextupole alignment tolerance [μm]	30	30	30

The quality of the sextupole field in one half of the geometry has been modeled (Figure 7.1.11). The field quality is consistent with the specified sextupole field throughout the required transverse region. The bore diameter of 66 mm was determined by specifications of field quality and the spatial constraint between the vacuum chamber and the poles and coil geometry. The base of the pole is widened to prevent saturation in that area at high field excitations.
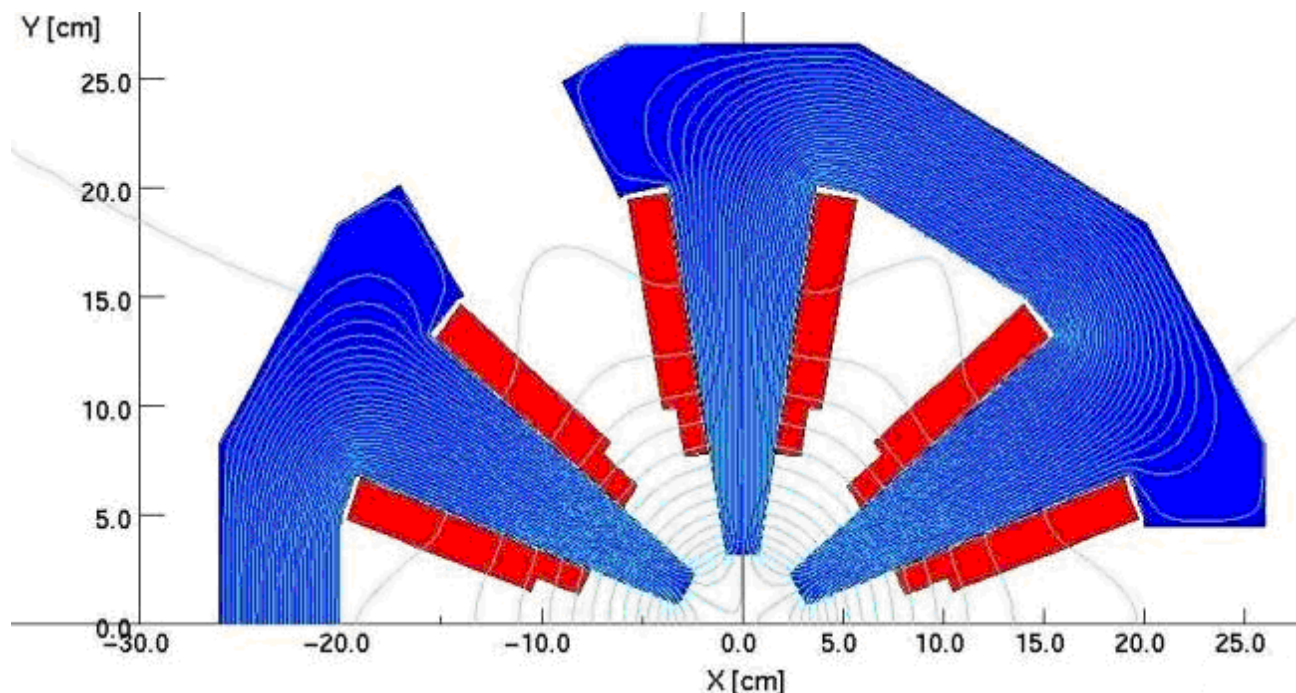
Figure 7.1.11   Sextupole magnet analytical model.

7.1.2.4.2   Mechanical Design of the Sextupole

The 390 sextupole magnets of the storage ring come in three lengths: 0.30 m, 0.25 m, and 0.2 m. To install the coils on a sextupole magnet, the magnet with three-fold symmetry must be divided into six identical segments (Figure 7.1.12). A 1 mm minimum clearance between the vacuum chamber and the adjacent poles is used to maintain thermal isolation during chamber baking. This gap is maintained to prevent the transmission of vibration from the vacuum chamber. The magnetic cores are made of steel sheet, AISI 1006 low-carbon, 1.5 mm thick. A square hollow copper conductor, 8×8 mm, inside diameter 4 mm, will be used in the coils, which are insulated with fiberglass at least 1.0 mm thick that is vacuum impregnated with highly radiation-resistant epoxy. Three water-cooling channels are connected in parallel on the sextupole magnet to distribute the power and to maintain the temperature increase of the coil to less than 10ºC.
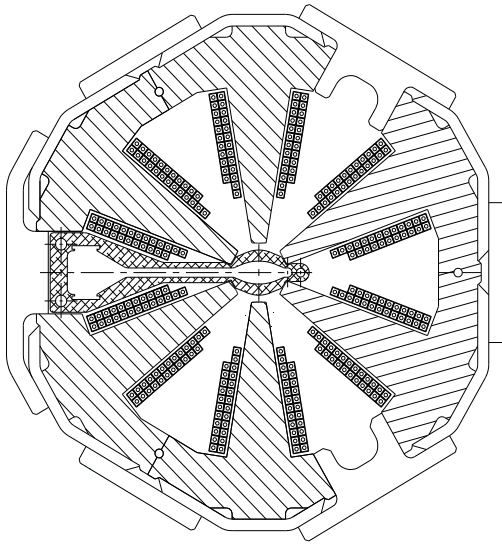
Figure 7.1.12   Conceptual design of the storage ring sextupole magnet cross-section depicting magnet yoke, the water-cooled coil, and the position of the vacuum chamber.

7.1.2.5   Correction Magnet Conceptual Design

In addition to the primary lattice magnets, the NSLS-II storage ring has corrector magnets. The correctors will be used to adjust the beam orbit and correct for alignment errors. The correctors will also be used as part of both global and local feedback systems. The conceptual design calls for 230 correctors to be installed at the start of operation.

Unlike other light sources, where steering correction can be integrated into combined-function lattice sextupoles, the precise alignment and field quality requirements of the NSLS-II sextupoles prevent the use of this combined function multipole, so only discrete correctors may be used.

There will be three types of correction magnets in the storage ring. The first type is a slow corrector operating with vertical and horizontal steering fields up to 400 Gauss from DC to less than 50 Hz. Ninety of these correctors will be located around the aluminum vacuum chamber. The maximum operational frequency of these correctors will be determined as part of the NSLS-II R&D program, as we study and optimize the corrector's field interaction with the vacuum chamber. Thirty of these correctors will possess skew quadrupole windings to deliver a maximum DC field gradient of 0.36 T/m.

A second type of corrector will be used for both static steering and dynamic global feedback. One-hundred-twenty of these correctors will have a DC component providing a maximum field of 320 Gauss for up to ±1.2 mrad vertical and horizontal steering as well as a dynamic component of ±0.15 mrad steering at up to 100 Hz. These correctors will be located around stainless bellows at either end of the dipole magnets.

A third type will be fast correctors providing a maximum field of 100 Gauss at a frequency up to or exceeding 100 Hz. At the start of operations twenty of these correctors will be used for local feedback and will be located around stainless steel sections of vacuum chamber or bellows. Two of these correctors will be located at either end of an insertion device, such as an undulator.

The geometry of the corrector magnets is highly dependent on the shape of the vacuum chamber around which they are assembled, and their location in the lattice. Several designs are being considered: the C-shaped dipole, a window frame-or box-shaped X–Y type corrector, and an APS-style corrector magnet. Silicon steel lamination 0.5 mm thick was selected for the magnet assembly, to suit the rate of charging of the corrector magnet.

Many factors must be considered in the corrector magnet design. The design of a corrector magnet will be specific to its required function, the space constraints of the specific locations in the lattice, and how the

corrector accommodates and interacts with the vacuum chamber design at its required location. Design options such as APS-style correctors are compact in size but tend to be rich in harmonics; the box-style correctors around the vacuum chamber have good field quality but tend not to use available space as efficiently, and have larger stray fields. Analytical modeling of the C-shaped correctors reveals that viable solutions exist for each corrector location. Specific design selection for each discrete corrector will be made during the next phase of design.

Injection magnets such as septum and kicker magnets are discussed in Section 5.9.

References

[7.1.1]   Creagh, D., et al., "An Infrared Beam-line at the Australian Synchrotron," SRI-2006.
[7.1.2]   Katoh, M., et al., "Coherent Terahertz Radiation at UVSOR-II," SRI-2006.

7.1.3   Storage Ring Power Supplies

These power supplies are designed to stay at a fixed current except for the fast dipole correctors. Most of the power supplies will be able to do simple ramps that will take 5 to 60 seconds from zero current to maximum current. These ramps will be software generated. The fast dipole correctors will be part of a beam-based feedback system. All power supplies will have at least a 20% margin in operating current. Listed below are the numbers of power supplies that will be required.

- B1-PS – 60 dipole magnets in series a circuit (50 small-aperture and 10 large-aperture magnets)
- Quad.3-PS1 to 330 – 330 quadrupole magnet circuits
- Quad.4-PS1 to 30 – 30 quadrupole magnet circuits
- Sext.2-PS1 to 240 – 240 sextupole magnet circuits
- Sext.25-PS1 to 120 – 120 sextupole magnet circuits
- Sext.3-PS1 to 30 – 30 sextupole magnet circuits
- B1Trim-PS1 to 60 – 60 B1 dipole trim magnet circuits (trim coils located on the B1 main dipoles)
- SKQ-PS1 to 30 – 30 skew quadrupole magnets circuits
- BH-PS1 to 90 – 90 intermediate speed horizontal dipole corrector magnet circuits
- BV-PS1 to 60 – 60 intermediate speed vertical dipole corrector magnet circuits
- FGBH-PS1 to 120 – 120 fast global horizontal correction dipole circuits
- FGBV-PS1 to 120 – 120 fast global correction dipole circuits
- FIBH-PS1 to 20 – 20 fast insertion horizontal correction dipole circuits
- FIBV-PS1 to 20 – 20 fast insertion vertical correction dipole circuits
- Total number of slow power supplies – 841
- Total number of intermediate-speed power supplies – 150
- Total number of fast power supplies – 280

7.1.3.1   B PS – Main Dipole Power Supply

This circuit consists of 50 small-aperture dipole magnets and 10 large-aperture dipole magnets, for a total of 60 magnets. The small-aperture magnets are 0.032 Ω and 13 mH. The large-aperture magnets are 0.040 Ω and 35 mH. The operating current for both magnets is ~360 A for 3.0 GeV. The cabling between magnets and the return will use 650 MCM flexible copper cable with a resistance of 0.162 Ω and inductance of 1.4 mH. The power supply load is 2.162 Ω and 1.001 H.

The power supply is a unipolar, two-quadrant, current-regulated supply. It will use two 12-pulse SCR converters in series with the center point connected to ground. This configuration will reduce the voltage to ground at the magnet load and reduce the voltage rating on various converter components. Each converter will

have a two-stage LCRL passive filter and a series pass active filter. This is required to reduce the ripple current to low levels (see Figure 7.1.13). The power supply will be able run in the invert mode while ramping down. This produces a negative voltage.

A combined digital and analog control system will control the operation of the power supply. The power supply will have a precision current regulator using a Direct Current Current Transformer as the current feedback device. The digital controls will use a feed-forward system to improve overall reproducability.

A PLC will be used for state control (on/off commands and interlocks).

Main Dipole Power Supply Specifications

|		
AC input power	■	3-phase 460 VAC ~683 AAC
DC maximum output current – Imax	■	450 ADC
DC minimum output current – Imin	■	~1 ADC
DC output voltage	■	1100 VDC
operating quadrants	■	2: (V+, I+) & (V-, I+)
small-signal – 3 db bandwidth	■	500 Hz
stability (8 h–10 s) – referred to Imax	■	40 ppm
stability (10s–300 ms) – referred to Imax	■	20 ppm
stability (300 ms–0 ms) – referred to Imax	■	10 ppm
absolute accuracy – referred to Imax	■	100 ppm
reproducability long term – referred to Imax	■	50 ppm
current ripple – referred to Imax	■	5 ppm 60 Hz and greater
resolution of reference current	■	18 bit ±1 LSB
resolution of current measured – fast sampling	■	16 bit ±1 LSB at 200 µsec
resolution of current measured – slow sampling	■	22 bit ±1 LSB at 16.67 msec
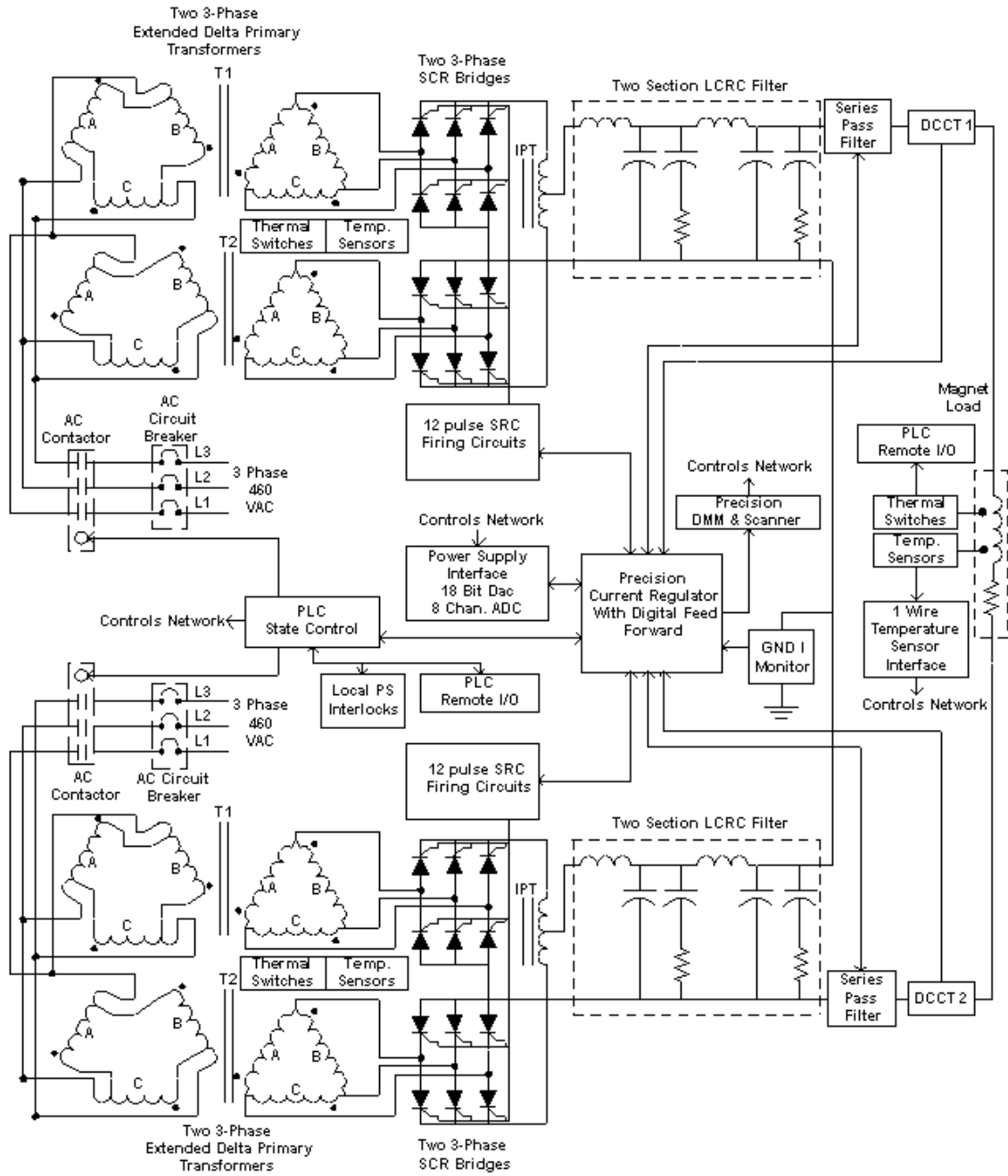
Figure 7.1.13 Dipole power supply block diagram.

7.1.3.2   Quad. 3 PS and Quad. 4 PS – Quadrupole Power Supplies

These circuits will use one power supply for each magnet. The magnet load parameters are close enough to use a single power supply for the two quadrupole magnet types. There are a total of 360 magnet circuits. The Quad.3 magnet is 90.0 mΩ and 50 mH. The Quad.4 magnet is 110.0 mΩ and 69 mH. The operating current is ~108 A for 3.0 GeV. The cabling between the magnets and power supply will be 250 MCM flexible copper cable. The power supplies will be located above the magnets in the equipment area. The cabling has a resistance of the 6 mΩ and an inductance of 0.1 mH. The worst-case power supply load is 116 mΩ and 69 mH.

The power supply is a unipolar, single-quadrant, current-regulated switch-mode design. The power section is a commercial voltage-controlled switch-mode programmable power supply with high output bandwidth (~1 kHz). These supplies have a 3 kW output power. They fit in a standard 19 inch electronics rack and are only 3.5 inches high. These power supplies are air-cooled. A precision analog regulator to control the current will be developed in-house. The power supply will use a DCCT as the current feedback device. To minimize current ripple, an additional output filter will be used. An AC input module will turn the power supply on and off. A microcontroller will be used for state control (on/off commands and interlocks). See Figure 7.1.14 for a block diagram of the Quad/Sext power supply.

Quadrupole Power Supply Specifications

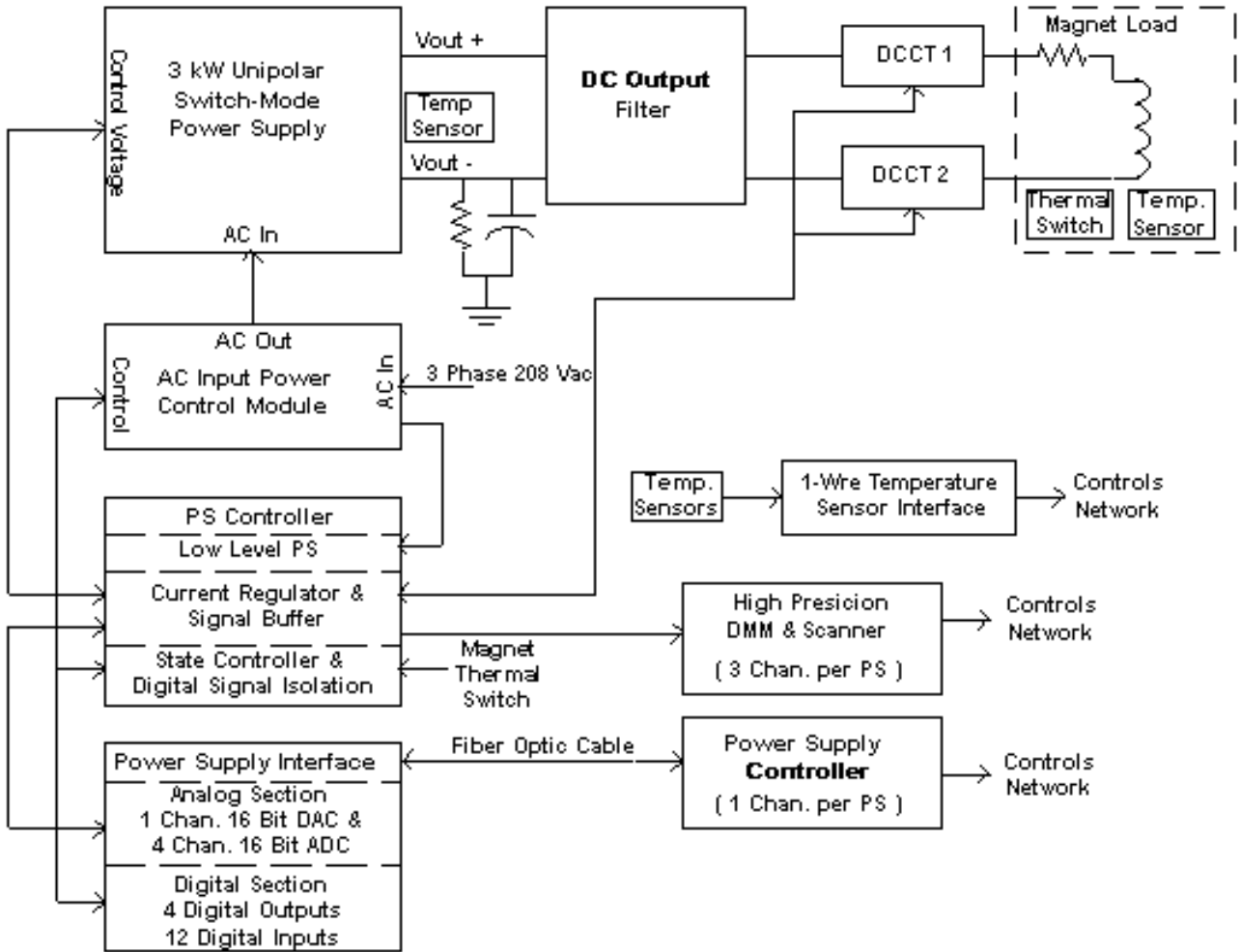|	
AC input power	■ 3-phase 208 VAC ~11 AAC
DC maximum output current - Imax	■ 150 ADC
DC minimum output current – Imin	■ ~0.5 ADC
DC output voltage	■ 20 VDC
operating quadrants	■ 1: (V+, I+)
small-signal – 3 db bandwidth	■ 300 Hz
stability (8 h–10 s) – referred to Imax	■ 200 ppm
stability (10s–300 ms) – referred to Imax	■ 200 ppm
stability (300 ms–0 ms) – referred to Imax	■ 100 ppm
absolute accuracy – referred to Imax	■ 200 ppm
reproducability long term – referred to Imax	■ 100 ppm
current ripple – referred to Imax	■ 15 ppm 60 Hz and greater
resolution of reference current	■ 16 bit ±1 LSB
resolution of current measured – fast sampling	■ 16 bit ±1 LSB at 200 μsec
resolution of current measured – slow sampling	■ 22 bit ±1 LSB at 16.67 msec

Figure 7.1.14   Unipolar current regulated switch-mode design power supply.

7.1.3.3   Sext. 2 PS, Sext. 25 PS, and Sext. 3 PS – Sextupole Power Supplies

These circuits will use one power supply for each magnet. The magnet load parameters are close enough to use a single power supply for the three sextupole magnet types. There are a total of 390 magnet circuits. The Sext.2 magnet is 27 mΩ and 9 mH. The Sext. 25 magnet is 32.0 mΩ and 11 mH. The Sext. 30 magnet is 37.0 mΩ and 13 mH. The estimated operating current is ~200 A for 3.0 GeV. The cabling between the magnets and power supply will be 350 MCM flexible copper with a resistance of 4 mΩ and inductance of 0.1 mH. The worst-case power supply load is 41.0 mΩ and 13 mH. The power supplies will be located above the magnets in the equipment area.

The supply is a unipolar, current-regulated switch-mode design, identical to that for the quadropoles. The power section is a commercial voltage-controlled, switch-mode programmable power supply with high output bandwidth (~1 kHz). These air-cooled power supplies have an output power rating of 3 kW. They fit in a standard 19 inch electronics rack and are only 3.5 inches high. A precision analog regulator to control the current will be developed in-house. The power supply will use a DCCT as the current feedback device. To minimize current ripple, an additional output filter will be used. An AC input module will turn the power supply on and off. A microcontroller will be used for state control (on/off commands and interlocks).

Sextupole Power Supply Specifications

AC input power	■	3-phase 208 VAC ~11 AAC
DC maximum output current – Imax	■	250 ADC
DC minimum output current – Imin	■	~0.5 ADC
DC output voltage	■	12 VDC
operating quadrants	■	1: (V+, I+)
small-signal – 3 db bandwidth	■	300 Hz
stability (8 h–10 s) – referred to Imax	■	200 ppm
stability (10s–300 ms) – referred to Imax	■	200 ppm
stability (300 ms–0 ms) – referred to Imax	■	100 ppm
absolute accuracy – referred to Imax	■	200 ppm
reproducability long term – referred to Imax	■	100 ppm
current ripple – referred to Imax	■	15 ppm 60 Hz and greater
resolution of reference current	■	16 bit ±1 LSB
resolution of current measured – fast sampling	■	16 bit ±1 LSB at 200 μsec
resolution of current measured – slow sampling	■	22 bit ±1 LSB at 16.67 msec

7.1.3.4   B1 Trim PS and SKQ PS – B1 Trim Coil Set Power Supplies

The B1 Trim PS circuit consists of the trim coil set located in the B1 dipole magnet. The coil set is 3.11 Ω and 26 mH. The SKQ power supply circuit consists of a corrector coil set located TBD; this coil set is estimated at 3.0 Ω and 5 mH. The operating current for both power supplies is ~2 A for 3.0 GeV. The cabling from the coil set to the power supply will be # 14 AWG flexible copper, routed through the tunnel ceiling into the equipment area above the main tunnel. The cabling has a resistance of 0.355 Ω and an inductance of 0.1 mH. The power supply is located above the magnet in the equipment area. The worst-case power supply load is 3.465 Ω and 0.026 H.

The bipolar, 4-quadrant, current-regulated linear power supply fits in a standard 19 inch electronics rack and is 5.25 inches high. An analog system will control its operation. The power supply will have a precision current regulator using a shunt as the current feedback device. A microcontroller will be used for state control (on/off commands and interlocks).

B1 Trim PS and SKQ PS Power Supply Specifications

AC input power	■	1-phase 120 VAC ~1.1 AAC
DC maximum output current – Imax	■	+5 ADC
DC minimum output current – Imin	■	−5 ADC
DC output voltage	■	±20 VDC
operating quadrants	■	4: (V+, I+), (V−, I+) , (V−, I-) & (V+, I−)
small-signal – 3 db bandwidth	■	10 kHz
large-signal bandwidth	■	~5 Hz
stability (8 h–10s) – referred to Imax	■	1000 ppm
stability (10s–300 ms) – referred to Imax	■	500 ppm
stability (300 ms–0 ms) – referred to Imax	■	100 ppm
absolute accuracy – referred to Imax	■	2000 ppm
reproducability long term – referred to Imax	■	1000 ppm
current ripple – referred to Imax	■	20 ppm 60 Hz and greater
resolution of reference current	■	16 bit ±1LSB
resolution of current measured – fast sampling	■	14 bit ±1 LSB at 200 μsec
resolution of current measured – slow sampling	■	22 bit ±1 LSB at 16.67 msec

7.1.3.5   BH PS and BV PS – Corrector Coil Set Power Supplies

The BH and BV Corrector PS circuits consist of the corrector coil set located in an HVC magnet. Each coil set is 0.09 Ω and 50 mH. The SKQ power supply circuit consists of corrector coil sets located TBD. This coil set is estimated at 3.0Ω and 1 mH. The operating current for both power supplies is ~15 A for 3.0 GeV. The cabling from the coil sets to the power supplies will be # 10 AWG flexible copper cable, routed through the tunnel ceiling into the equipment area above the main tunnel. The cabling has a resistance of 0.140 Ω and an inductance of 0.1 mH. The worst-case power supply load is 0.230 Ω and 0.050 H. The power supply is located above the magnet in the equipment area.

The BH and BV power supplies are bipolar, 4-quadrant, current-regulated linear PS that fit in a standard 19 inch electronics rack and are 5.25 inches high. An analog control system will control their operation. Each will have a precision current regulator using a shunt as the current feedback device. These corrector power supplies are part of an intermediate-speed beam position feedback system. A microcontroller will be used for state control (on/off commands and interlocks).

Corrector Coil Set Power Supply Specifications

AC input power	■	1-phase 208 VAC ~2.6 AAC
DC maximum output current – Imax	■	+ 20 ADC
DC minimum output current – Imin	■	− 20 ADC
DC output voltage	■	±200 VDC
operating quadrants	■	4: (V+, I+) , (V−, I+), (V−, I−) & (V+, I−)
small-signal – 3 db bandwidth	■	10 kHz
large signal – bandwidth	■	~5 Hz
stability (8 h–10 s) – referred to Imax	■	1000 ppm
stability (10s–300 ms) – referred to Imax	■	500 ppm
stability (300 ms–0 ms) – referred to Imax	■	100 ppm
absolute accuracy – referred to Imax	■	2000 ppm
reproducability long term – referred to Imax	■	1000 ppm
current ripple – referred to Imax	■	20 ppm 60 Hz and greater
resolution of reference current	■	16 bit ±1 LSB
resolution of current measured – fast sampling	■	14 bit ±1 LSB at 200 μsec
resolution of current measured – slow sampling	■	22 bit ±1 LSB at 16.67 msec

7.1.3.6   FIBH PS and FIBV PS

The FIBH and FIBV fast insertion corrector power supply circuits consist of the corrector coil set located in a fast insertion HVC magnet. These magnets are located in the insertion region on either side of an insertion device. Each coil set is estimated at 1.5 Ω and 13 mH. The operating current for the power supplies is ~5 A for 3.0 GeV. The cabling from the coil sets to the power supply will be # 14 AWG flexible copper, routed through the tunnel ceiling into the equipment area above the main tunnel. The cabling has a resistance of 0.355 Ω and inductance of 0.1 mH. The worst-case power supply load is 1.86 Ω and 0.013 H. The power supply is located above the magnet in the equipment area.

The bipolar, 4-quadrant, current-regulated linear power supplies fit in a standard 19 inch electronics rack and are 5.25 inches high. An analog control system will control their operation. The power supply will have a precision current regulator using a shunt as the current feedback device. These corrector power supplies are part of a fast beam position feedback system. A microcontroller will be used for state control (on/off commands and interlocks).

Fast Insertion Corrector Power Supply Specifications

AC input power	■	1-phase 208 VAC ~2.6 AAC
DC maximum output current – Imax	■	+6 ADC
DC minimum output current – Imin	■	-6 ADC
DC output voltage	■	±72 VDC
operating quadrants	■	4: (V+, I+) , (V–, I+), (V–, I–), & (V+, I–)
small-signal – 3 db bandwidth	■	10 kHz
large signal – bandwidth	■	100 Hz
stability (8 h–10 s) – referred to Imax	■	1000 ppm
stability (10s–300 ms) – referred to Imax	■	500 ppm
stability (300 ms–0 ms) – referred to Imax	■	100 ppm
absolute accuracy – referred to Imax	■	2000 ppm
reproducability long term – referred to Imax	■	1000 ppm
current ripple – referred to Imax	■	20 ppm 60 Hz and greater
resolution of reference current	■	16 bit ±1 LSB
resolution of current measured – fast sampling	■	14 bit ±1 LSB at 200 μsec
resolution of current measured – slow sampling	■	22 bit ±1 LSB at 16.67 msec

7.1.3.7   FGBH PS and FGBV PS

The FGBH and FGBV fast global corrector power supply circuits consist of the corrector coil set located in a fast global HVC magnet. The coil set is not yet designed. The operating current, coil resistance and coil inductance is TBD. The cabling from the coil sets to the power supply will be flexible copper, routed through the tunnel ceiling into the equipment area above the main tunnel. The power supply is located above the magnet in the equipment area.

Plans are to use a bipolar, four-quadrant, current-regulated linear power supply. It will fit in a standard 19 inch electronics rack. An analog control system will control their operation. The power supply will have a precision current regulator using a shunt as the current feedback device. This corrector power supply is part of a fast beam position feedback system. A microcontroller will be used for state control (on/off commands and interlocks).

Fast Global Corrector Power Supply Specifications

AC input power	■ TBD
DC maximum output current – Imax	■ TBD
DC minimum output current – Imin	■ TBD
DC output voltage	■ TBD
operating quadrants	■ 4: (V+, I+), (V–, I+), (V–, I–), & (V+, I–)
small-signal – 3 db bandwidth	■ 10 kHz
large signal – bandwidth	■ 100 Hz
stability (8 h–10 s) – referred to Imax	■ 1000 ppm
stability (10s–300 ms) – referred to Imax	■ 500 ppm
stability (300 ms–0 ms) – referred to Imax	■ 100 ppm
absolute accuracy – referred to Imax	■ 2000 ppm
reproducability long term – referred to Imax	■ 1000 ppm
current ripple – referred to Imax	■ 20 ppm 60 Hz and greater
resolution of reference current	■ 16 bit ± 1 LSB
resolution of current measured – fast sampling	■ 14 bit ± 1 LSB at 200 μsec
resolution of current measured – slow sampling	■ 22 bit ± 1 LSB at 16.67 msec

7.1.3.8 Power Supply Interlocks

All power supplies will have sufficient interlocks that will prevent the power supply from becoming damaged due to changes in cooling conditions, ac power disturbances, and nonstandard operating conditions.

All magnet coils will have an over- temperatures interlock if there is a change in cooling and/or operating conditions.

All power supplies will have an electrical safety interlock that will prevent the power supply from turning on if the machine safety system requires it.

7.1.3.9 Power Supply Instrumentation

Redundant DCCTs or shunts will be used to confirm the power supply current reproducability.

High-precision DMMs and scanners will be used to monitor the power system current, the redundant current sensor, and the analog current set point. This equipment will ensure long-term stability and reproducability.

Temperature monitoring of the magnet coils and power system environment will be accomplished using low-cost digital temperature sensors. With such system, a problem can be identified before it becomes an emergency, making it possible for repairs to be scheduled more conveniently.

7.1.3.10 Power Supply Controls

The slow power supplies will require software generated current references for each power supply. The Power Supply Interface has a precision DAC for generating the reference current and a multi-channel ADC for inputting PS signals. The PSI also has digital IO for state control and status read backs of the PS.

A VME device card will be used to communicate between the control system and the PSI. This card will be located in a control system's VME chassis that will be mounted in one of the power supply system racks. This card will generate the reference current profiles, input analog data, and perform digital state control and status readbacks. The output of the device card is a fiber optics cable that connects to a PSI.

The other controls will include the operation of the high-precision DMM and scanner and readout of the digital temperature sensors.

7.1.3.11   Electrical Safety

All power supplies will conform to the latest BNL safety requirements, especially concerning arc flash protection. Whenever possible, NRTL-listed equipment will be used.

7.1.3.12   Cable Tray Cable Routing

The cable tray for the dipole magnet circuits will be located in the equipment area above the main tunnel. The cable will drop through the tunnel ceiling at each cell, where it will connect to two dipole magnets. There will also be a tray along the inside wall of the main tunnel only in the area of the cell. This tray will be located in a different area then the booster cable tray. The dipole cables will be installed with a twist to prevent pickup from the booster circuits. All cables will be tray-rated cables. Power cables will be arranged to minimize pickup from other circuits. All power cables will be separated from signal cables. The quadrupole, sextupole, and corrector cables will be routed through conduit in the main tunnel ceiling. The power supply racks will be located above the conduits. The cable going through the conduit will run in the cable tray mounted on the inside wall until it is connected to the magnet. All cables and trays will meet NEC codes.

7.1.3.13   Power Supply Racks

All storage ring power supplies except for the dipole will be mounted in sealed Nema 12 electronics racks. These racks will have a maximum of six 3-kW power supplies installed in them. These racks will also have power supply controls and instrumentation installed in them. At each cell location there are 10 racks. The racks will be located above the magnets they supply power to. A water-to-air heat exchanger will cool a set of two or three racks. Cooled air will flow through the power supplies and circulate back to the heat exchanger. The heat exchanger will use chilled water and have the outlet temperature regulated (Figure 7.1.15).
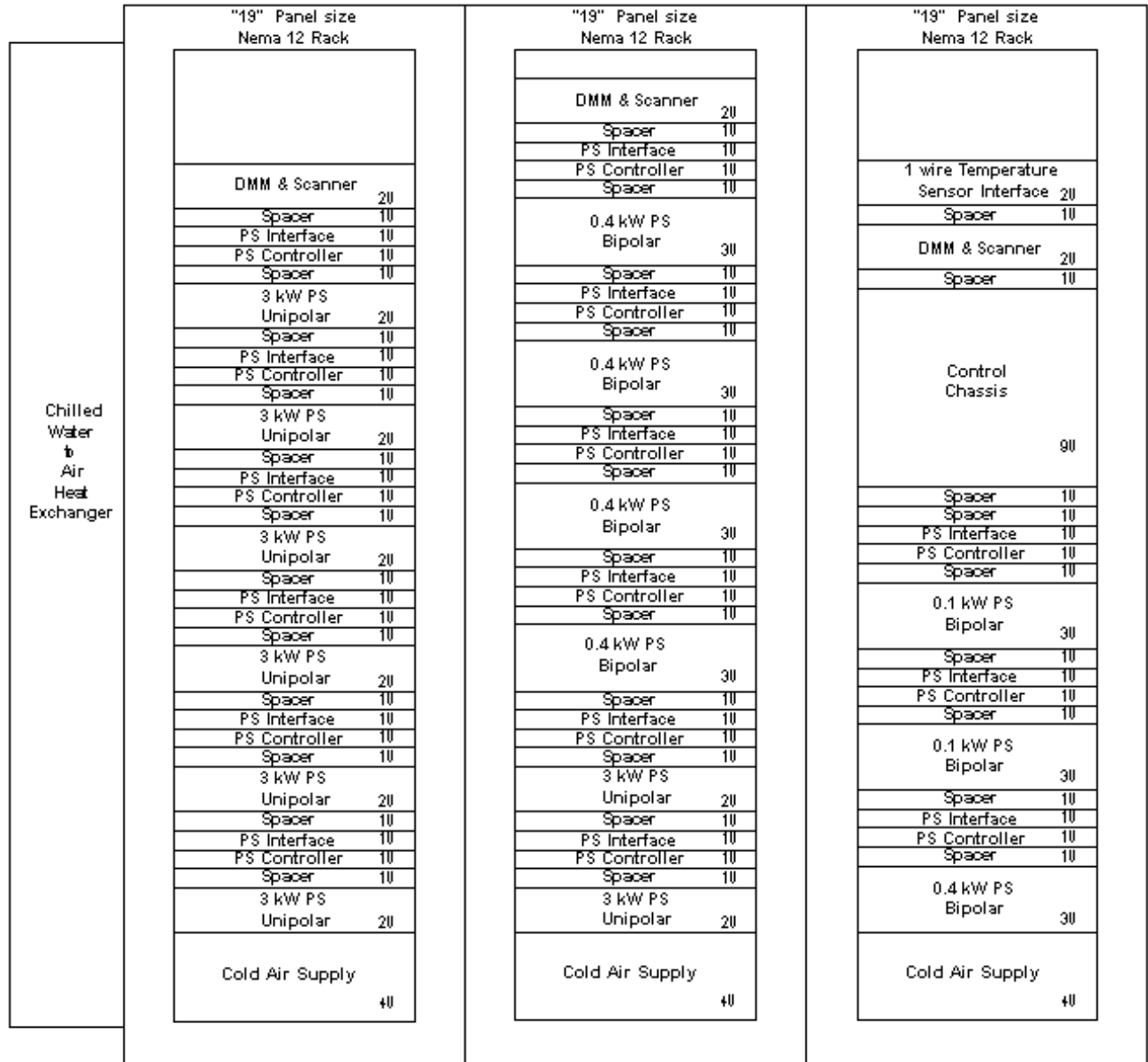
Figure 7.1.15 Single magnet power supply rack layout.

7.2   Magnet–Girder Support System

7.2.1   Scope

This section describes alignment tolerances, stability requirements, and conceptual design of the storage ring magnet support system. Specifications for magnet alignment and stability are established from analysis of the storage ring nonlinear dynamics. Functional requirements of the girder supports are presented and design features for meeting these requirements are discussed. Various sources of ambient motion affecting the stability of the support system are identified and design solutions to mitigate their effects are discussed

7.2.2   Alignment Tolerances and Stability Requirements

The alignment tolerances for the ring magnets impact the ring performance in several ways. Magnet alignment is necessary to be able to store the electron beam with the design emittance and lifetime (i.e., sufficient dynamic aperture, DA). First, there is a relative magnet-to-magnet alignment tolerance to a line relative to the rigid girder. Second, there is an alignment tolerance specified for the transverse position of the ends of the girder and its roll angle and longitudinal position (six parameters), as it is installed in the tunnel. The girder misalignment introduces a correlated offset of the magnets. For this conceptual design, we took the achieved magnet-to-magnet alignment values from recently commissioned light sources as our specification and calculated the impact on the DA. Future studies will further explore these sensitivity to these tolerances, along with the tolerance on magnetic field errors. The current tolerances are listed in Table 7.1.1. The impact of tolerance errors is discussed in Section 7.1.1.

The stability of closed-orbit position is critical to providing a constant flux in the user beamlines (i.e., intensity through slits and mirror systems). There are several sources of steering that cause large closed-orbit motion (relative to the user beamline): power supply fluctuations, energy modulations, and alignment variations due to vibrations of the magnets. We only consider the last effect here. The magnet motions that are of most concern are those of the quadrupole transverse position, dipole longitudinal position, and roll angle. This closed-orbit motion is the result of the large COAF, discussed in Section 7.1, which determined the magnitude of beam motion per unit of transverse motion of the quadrupoles, assuming that all quadrupole motions were uncorrelated in location around the ring, as well as uncorrelated in time. Here we discuss in more detail the time variation of the beam orbit due to quadrupole and dipole motion and the impact this has on the user beam.

To estimate the magnitude of the resulting orbit motion, we need to know how the quadrupoles are shifted around the ring. This depends on the noise source that generates this motion, as well as its coupling to the magnets through their support system (girders and floor). The simplest model of these magnet vibrations is just the random fluctuations of the magnet centers by a common tolerance level and assuming this impact will be the same at any frequency of vibration. This tends to overestimate the impact on the beam motion, since it ignores correlations that will smooth the distortions, as well as the synchrotron radiation damping that will damp the beam to the shifted closed orbit. This latter effect will mean that for frequencies greater than $F_{x,y} \approx 1/\tau_{x,y}$, where $\tau_{x,y}$ are the transverse damping times, the effective beam emittance will grow, while the centroid orbit shift will be reduced from that estimated from the random closed-orbit shift calculation.

We place a limit on the amplitude of magnet motion to be that which contributes to an RMS orbit shift equal to 10% of the RMS beam size in that plane. These sizes are shown in Table 7.2.1 for beam at the center of the two ID straight sections (long and short, LID and SID):

Table 7.2.1   Beam Size at the Center of the ID Straights for 0.5 nm-rad (H) and 0.008 nm-rad (V) Emittance.

	LID Straight (8 m)	SID Straight (5 m)
$\sigma_x\,[\mu m]$	96	37
$\sigma_y\,[\mu m]$	5	2.7

The closed orbit at the center of the short straight section for 2,000 random seeds is shown in Figure 7.2.1, for the ring quadrupoles shifted by Gaussian random values with RMS values of ($\Delta X = 0.163$ μm and $\Delta Y = 0.023$ μm). Each point represents a different sampling of the random fluctuations of the quadrupole centers at any frequency with that amplitude, and includes all of the nonlinear elements in the calculation.
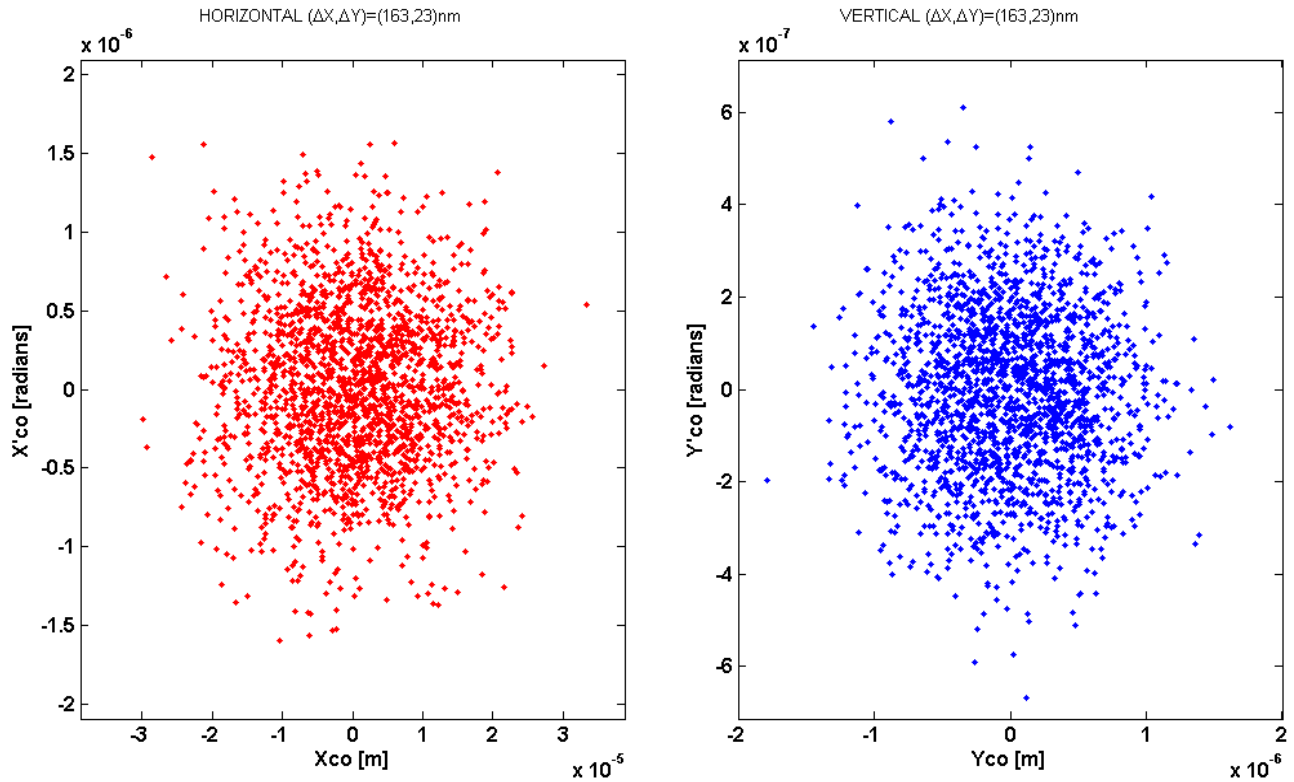
Figure 7.2.1   The horizontal and vertical closed-orbit in the LID straight for 2,000 seeds with RMS random quadrupole center shifts of ΔX = 0.163 and ΔY = 0.023 μm.

The RMS horizontal and vertical beam orbit shifts were 19.4 and 0.5 μm, respectively, or 10% of the RMS beam size in the LID. These RMS values give a very conservative tolerance for quadrupole vibration tolerances. At frequencies above the damping frequency, $F_{x,y}$, this calculation gives an estimate of the emittance dilution.

$$\Delta \varepsilon_x / \pi = \frac{1}{n}\sqrt{\sum x^2 \sum x'^2 - \left(\sum x x'\right)^2}$$

(7.2-1)

where *x* and *x'* are closed orbit and slope from each seed and the sum is over all seeds. The effective emittance dilution shown in Figure 7.2.1 is only 1% horizontal and 1% vertical of the emittance plane, or $\Delta\varepsilon_x$ = 5.1 pm and $\Delta\varepsilon_y$ = 0.09 pm, representing a small increase in the damped beam emittance.

Since the dipole magnets do not have gradients, their transverse motions have little impact on the closed-orbit motion. However, longitudinal position fluctuations of the dipoles will also create a horizontal beam motion and the roll angle will create a vertical closed-orbit motion. Using a similar random distribution analysis, we set a tolerance level for the RMS fluctuations of the dipole longitudinal position, ΔS <2 μm, and the dipole roll angle of $\Delta\theta$ <0.1 μrad. These tolerances, together with the quadrupole levels set above, contribute increases of the RMS closed-orbit motions of 11% and the effective emittance dilution of

$$\Delta\varepsilon_x = 5.6 \text{ pm and } \Delta\varepsilon_y = 0.12 \text{ pm.} \tag{7.2-2}$$

Because the magnets are not supported independently but on girders, magnetic center fluctuations will be correlated. In Section 7.1.1 the effect of random misalignment of the girders was considered and the closed-orbit Girder Amplification Factor was computed to be 3 to 5 times less than the COAF for the quadrupoles, for independent fluctuations. The GAFs in the long ID straight sections are 15.4 μm (H) and 7.1 μm (V). In the short ID straight sections the GAFs are 4.8 μm (H) and 2.3 μm (V). To maintain an RMS closed-orbit fluctuation of ~10% of the RMS beam size in the LID would require random girder fluctuations of less than 0.62 μm (H) and 0.07 μm (V). The tolerances for the SID would be 0.77 μm (H) and 0.12 μm (V). This shows the reduction in tolerance levels for vibrations coming from the correlation of the magnet vibrations, compared to the random quadrupole tolerance, and that the random model tends to yield a worst-case tolerance level estimate for vibrations.

Another model for quadrupole magnet center fluctuations attempts to include a magnet-to-magnet spatial correlation based on a ground movement model of a plane wave passing through the ring. This model was implemented in the accelerator design code BETA-ESRF [7.2.1]. The horizontal and vertical quadrupole motions are then calculated from the amplitude and wavelength (λ) of the wave. The increase in the effective emittance can be calculated from the closed-orbit shift around the ring using Eq. (7.2-1). Since there will be a dependence on the direction of the wave relative to straight sections, several phases relative to the lattice orientation have been considered, to estimate the maximum impact. The wavelength varies as a function of frequency, which depends on the knowledge of the speed of propagation. We assumed V = 270 m/sec for both S and P waves (see Section 7.2.3.5.1 for measurement for the BNL site). The impact on the beam's closed-orbit shift is then estimated by displacing the center of each quadrupole on the corresponding point of the plane wave. The effective amplitude of the closed-orbit distortion is estimated by sampling the closed orbit around the ring, instead of for different seeds. No consideration for the girders is taken, nor is there any damping of the wave or the beam assumed. Figure 7.2.2a shows the tolerance level for the horizontal (pressure, P) wave amplitude versus frequency (f = V/ λ), for an effective emittance dilution that is 1% of the beam emittance, or 5 pm.

Figure 7.2.2b shows the tolerance level for the vertical (shear, S) wave amplitude versus frequency (f = V/ λ), for an emittance dilution that is 1% of the beam emittance, or 0.08 pm. Clearly, as the wavelength exceeds the ring diameter of 248 m (f<~2 Hz), the entire ring moves in phase and the closed-orbit impact becomes small; the tolerance becomes quite large. Above 20 Hz (H) and 10 Hz (V), the amplitude tolerance becomes almost independent of frequency, about at the levels where ΔX = 0.08 μm and ΔY = 0.04 μm.
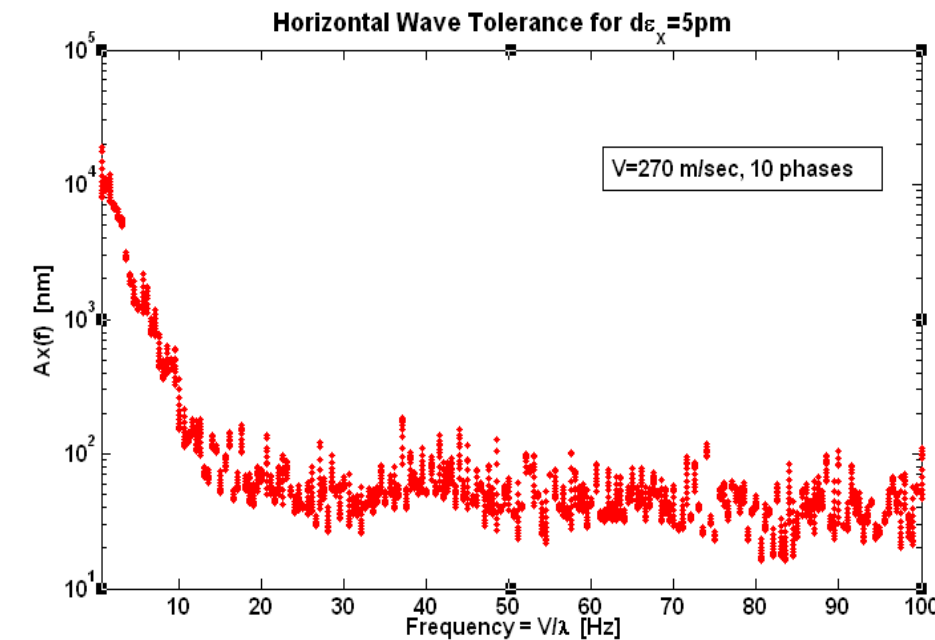
Figure 7.2.2 a   The tolerance level for a horizontal wave amplitude, in nm, yielding a 5 pm emittance dilution, assuming a wave velocity of 270 m/sec.
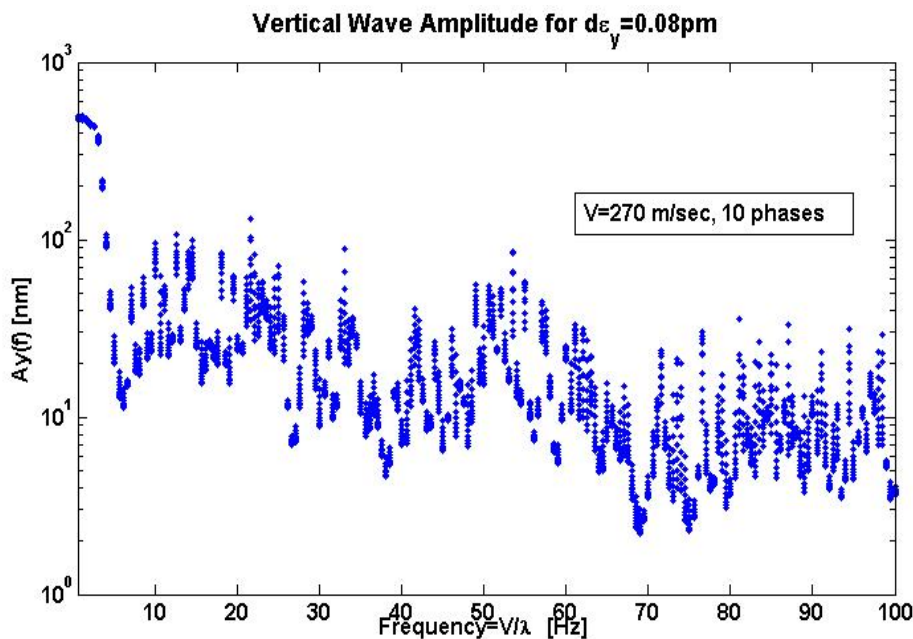

Figure 7.2.2 b   The tolerance level for a vertical wave amplitude, in nm, yielding a 0.08 pm emittance dilution, assuming a wave velocity of 270 m/sec.

At frequencies below the 2 Hz level, clearly this model will yield very large tolerances, since all the ring magnets move together. In the low-frequency range (up to ~50 Hz), the global feedback system will take out most of the closed-orbit motion independent of the source term, to a level limited by the BPM and corrector electrical noise level. Above 50 Hz, the centroid motion becomes less obvious, but the beam emittance will be diluted by the effective emittance resulting from the magnet motion.

In summary, the magnet stability tolerances estimated with these models show the worst-case being the random model for the ~10% vertical beam size. However, the effective emittance contribution of this is 1% of the beam emittance and could be relaxed at least by a factor of 2, to about 0.050 µm. These tolerance limits, for the magnets only, are listed in Table 7.2.2. All other tolerances are readily achievable with careful design of girders and the accelerator floor. However, a global feedback system is planned, to ensure that orbit stability is achieved even if these tolerances cannot be achieved. Based on the calculations in Section 6.3, this feedback system will handle random quadrupole fluctuations as large as 0.3 µm vertically.

Table 7.2.2   Magnet Stability Tolerances for AC Closed-Orbit Stability, without Feedback Correction.

Tolerance Limits	ΔX RMS Quads	ΔY RMS Quads	X (LID) RMS (ε_x)	Y (LID) RMS (ε_y)
Random motion	<0.163 µm	<0.023 µm	9.4 µm (5.1 pm)	0.5 µm (0.09 pm)
Random girder motion	<0.62 µm	<0.070 µm	9.4µm (5.1 pm)	0.5 µm (0.09 pm)
Plane wave <5Hz	>2 µm	>0.1 µm	(5 pm)	(0.08pm)
Plane wave >10Hz	~0.08 µm	~0.04 µm	(5 pm)	(0.08 pm)
Additional limits	**ΔS RMS Dipole**	**Δθ RMS Dipole**		
Random motion	≤2 µm	≤0.1 µrad	10 µm (0.006 nm)	0.58 µm (0.12 pm)

7.2.3   Conceptual Design of the Magnet–Girder Support System

7.2.3.1   Functional Requirements

The storage ring girders in a cell provide common mounting platforms for different set of magnets, as shown in Figure 7.2.3. Multipole magnets are mounted on girders number 1, 3, and 5. Dipoles are mounted on separate girders, numbered 2 and 4, because of their height difference and less stringent alignment and stability requirements.
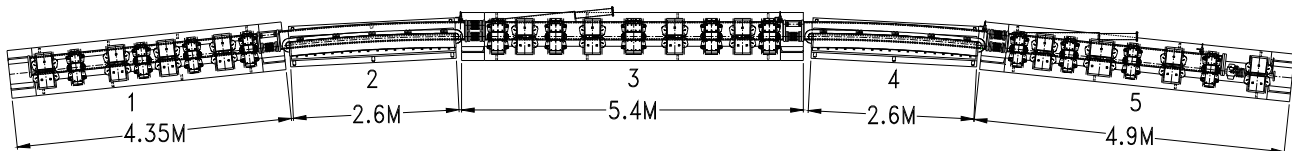

Figure 7.2.3   NSLS-II girders in one cell of the storage ring.

General functional requirements of the magnet–girder support system are given as follows:

1. Raise the centers of the magnets to the nominal beam height of 1 m. This height was chosen based on stability considerations that are discussed in Section 7.2.2.
2. Provide a stable platform for assembling and aligning the magnets outside the tunnel. The stringent alignment tolerances can only be met by precision alignment techniques (see Section 7.2.3.3) requiring out-of-tunnel assembly and alignment. The magnet alignment must remain unperturbed during the transportation and installation of the magnet–girder assemblies in the tunnel.
3. Meet girder-to-girder alignment requirements, both during the initial alignment and subsequently to compensate for long-term floor settlement.
4. Meet dynamic stability requirements under expected ambient floor motion, flow-induced vibrations, and temperature fluctuations of the tunnel air and process water.

In addition, the overall width of the magnet–girder support system must be less than 1 m, for ease of transportation and assembly in the tunnel. The support design must also be cost effective without sacrificing speed of installation and alignment.

7.2.3.2   Main Conceptual Design Features

In many recent light sources the girders have been precisely fabricated with very stringent top surface tolerances (~15 μm flatness) and with T-slot type alignment features. Magnets, built with equally tight tolerances, are fastened directly to the girder's top surface without an interface of alignment hardware. After a careful examination of this approach, we decided to design NSLS-II girders and magnets with conventional tolerances, and to use a vibrating-wire alignment technique for aligning the magnets to ~30 μm precision.

A typical girder with its mounting pedestals is shown in Figure 7.2.4. The nominal length is 2.6 m for the dipole girders and 4.35 to 5.4 m for the multipole girders. The girders are approximately 0.8 m wide and 0.4 m high. They are fabricated by welding commercially available plates and channels of thicknesses ranging from 1 to 2 inches. After welding, the girders are stress-relieved by commercial vibratory stress-relief equipment.
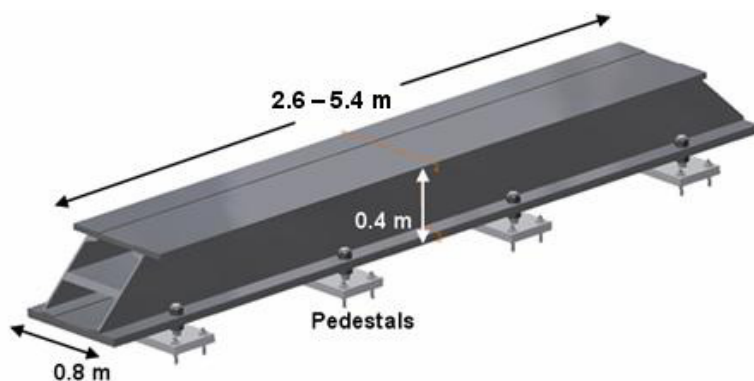

Figure 7.2.4   Conceptual design of the NSLS-II storage ring girder.

The girders are mounted on four 2-inch-thick pedestals that are grouted to the floor with nonshrinking epoxy grout. For mounting and height adjustment, eight 2 inch-diameter bolts with spherical washers are used. The girder is thus over-constrained in order to minimize static deflection and raise the first natural frequency of the magnet–girder assembly. A similar over-constrained scheme has been used successfully at SPring-8 [7.2.2] and will be implemented at the ALBA light source [7.2.3].

7.2.3.3   Magnet–Girder Assembly and Alignment

NSLS-II lattice magnets have magnetic alignment tolerances that exceed mechanical assembly tolerances and the ability of conventional alignment techniques to locate the magnetic components within the required tolerances. Therefore, a vibrating wire alignment technique, originally developed at Cornell University [7.2.4] and subsequently adopted at SLAC, will be used. It has been shown that this technique is capable of aligning magnets on the same girder to within 10 μm.

In this alignment technique, a generator supplies a varying current in the wire and the field of the magnet causes the wire to vibrate. Adjusting the current frequency puts the driving forces in resonance with the wire's vibrating modes. This creates standing waves on the wire that are detected by optical wire sensors. In this way, the null center of the magnet can be located to within a few microns. Laser trackers are then used to transfer the position of the wire to the tracker cups on the girder.
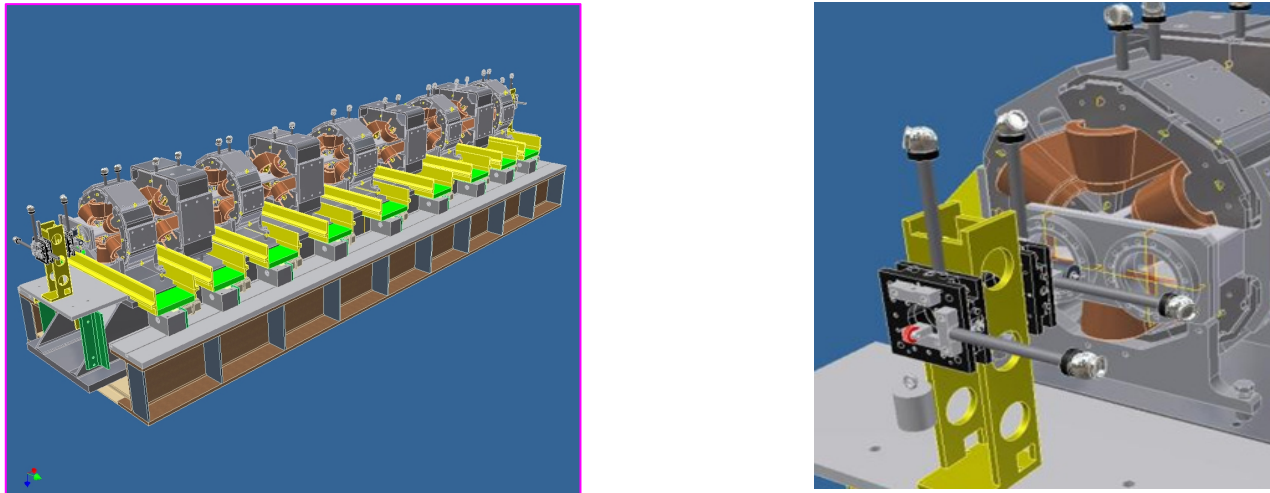
Figure 7.2.5 Left: Vibrating wire alignment system mounted on the girder. Right: Special brackets with wire movers, wire locators, and laser tracker fiducials are attached to either end of the girder.

Initially, the magnets will be installed and aligned on the girder with a laser tracker. The top-half of the multipole magnets will then be split and the vacuum chamber will be installed. The ends of the chamber will be sealed with Mylar caps. The caps will have small holes in either end to allow the ends of the vibrating wire to protrude through while a positive purge of dry nitrogen gas is maintained.

A clean wire will be installed into the vacuum chamber prior to bakeout and conditioning. Vibrating wire support brackets will be attached to either end of the magnet girder assembly and the wire will be secured to X–Y translation stages mounted on these brackets (Figure 7.2.5). After the top half of the magnets are reassembled, their iron cores will be supported on precisely computer-controlled positioners (such as cam movers). The roll angles of the magnet cores will be brought to within ±0.2 mrad tolerance by using magnet positioners and digital inclinometers. For each magnet the sag of the stretched wire is compensated by using translation stages to introduce a vertical offset in the wire's position. The magnet is aligned by moving it to a "null" position that stops the wire from vibrating. The core of the magnet is then fastened to its support frame.

7.2.3.4   Installation of the Magnet–Girder Assembly

A transporter system with self-contained air pads will be used to transport the girder–magnet assemblies from the alignment laboratory into the storage ring tunnel for final installation.

During the early phases of girder installation, the multipole girders will be installed prior to the dipole magnets. The wire support brackets will be left attached for the entire installation process. The air pad system will cushion any shocks to the girder during transport, assuring accurate magnet location. The girder transporter will locate the girder over the eight pedestals studs that will affix the girder to the tunnel floor.

Instrumented torque wrenches will be used in conjunction with laser trackers to precisely offload the girder from the air pads onto the pedestals' studs. Once the girder is fixed to the floor and prior to dipole installation, in-situ vibrating wire measurements will be repeated to confirm alignment of the magnets. These measurements will be discontinued when it is established that the magnet alignment was not disturbed during transportation and alignment.

7.2.3.5   Mechanical Stability of the Magnet–Girder Support System

Sources affecting the mechanical stability of the support system include ground settlement, ambient floor motion, flow-induced vibrations, and thermal transients. These sources can be categorized in terms of the

frequency range—*fast* when greater than a few Hz or *slow* when operating at frequencies lower than one Hz. Sources are also categorized based on the time-scale of the excitation, as being short (<1 hour), medium-term (<1 week), or long-term (>1 week). Short-term sources include natural and cultural ground vibrations, flow-induced vibrations, and power supply jitters. Thermal transients due to temperature changes of the cooling water or the tunnel air, as well as gravitational and tide effects, constitute medium-term sources. Floor settlement or seasonal temperature changes, which may have direct impact on the alignment of components, are considered to be long-term effects. Cultural noise or human activity is typically observed in the frequency range of 1 to 100 Hz. Ground motion from ocean waves or tides is centered at about 0.2 Hz.

7.2.3.5.1 Medium- and Long-Term Stability

Over the years, various studies have been performed at the BNL site and in the vicinity of NSLS-II to characterize the subsurface conditions. Drill-core data show that the soil at the site consists mainly of medium coarse sand with traces of silt and, in some cases, traces of clay and gravel. The shear wave velocity in the top sand layer is about 270 m/sec. The bedrock lies at a depth of approximately 430 m beneath the site. Therefore, the BNL site, including the NSLS-II site, is classified as a very deep site with relatively soft soil. The soil consisting of glacial sands is well settled and, based on the drill-core results, exhibits limited scatter in key properties (coefficient of variation ~0.18). This is important, in that the differential movement (or settlement) in the soil supporting NSLS-II is expected to be of the order of 10 μm /10 m / year. To ensure that this is the case, a detailed study of ground settlement based on finite element analysis will be performed, taking into account both the site soil conditions and the facility layout.

7.2.3.5.2 Short-Term Stability

Short-Term Stability – Ambient Ground Motion

Ambient ground motion measurements near the NSLS-II site were taken from August 31 through September 1, 2006. Data measured at the following locations at BNL were used for a comparison of the NSLS-II site with the ALS, ESRF, and SPring-8 sites:

1. Microscopy suite of the Center for Functional Nanomaterials currently under construction
2. Foundation of a light stand near CFN, not stiffened by the presence of the building
3. A remote location near the northeast corner of BNL
4. Experimental hall of NSLS directly beneath the X1 beamline

The RMS (4–50 Hz) amplitudes of the ground motions in vertical, north–south, and east–west directions are given in Table.7.2.3. The most important value is that of the microscopy laboratory at CFN, where the RMS amplitudes are 20 nm or lower in all directions. The lower values, compared to those at the free-field at CFN and at the remote northeast BNL location, are indicative of the stiffening effect of the CFN building and the floor. The ambient ground motion at the floor of NSLS X1 beamline is considerably higher at 18 and 30 Hz, due most likely to rotating mechanical equipment.

Table 7.2.3   RMS (4-50 Hz) Ground Motion near the NSLS-II Site.

Location	Time	Vertical (nm)	North–South (nm)	East–West (nm)
Microscopy lab at CFN	7:30 pm	20	12	19
Free-Field at CFN	11:40 pm	24	41	38
Remote location near the northeast corner of BNL	Noon	21	25	26
Beamline X1 at NSLS	Midnight	71	12	13

Figure 7.2.6 shows the vertical log mean of site vibrations at the NSLS-II site expressed as PSD, compared with similar data from ALS, ESRF, and SPring-8. Shown also are PSD spectra measured at NSLS beamline X1 just after midnight, the "free-field" location near CFN, and the microscopy suite at CFN identified by the black arrow. The legend indicates the RMS amplitude using summation between 4 and 50 Hz, except for the NSLS-II log mean, which is summed with a 6 Hz lower cutoff because of contamination by the instrumentation noise floor at lower frequencies. The RMS amplitudes for ALS, ESRF, and SPring-8 were calculated in the 2 to 100 Hz band.
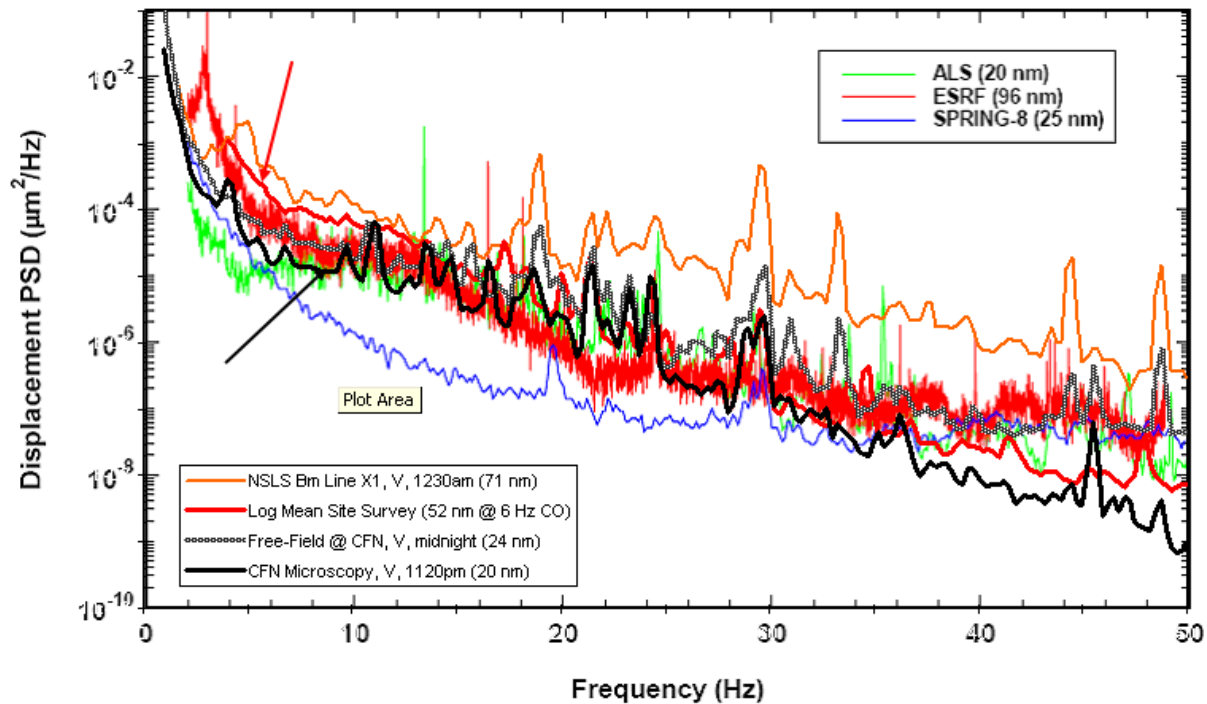

Figure 7.2.6:   Comparison of PSDs of vertical ground motions at various locations near the NSLS-II site and at ALS, ESRF, and SPring-8 light sources [7.2.5].

The vibration measurements indicate the presence of local noise sources at ~18 and 30 Hz in the NSLS building. Further vibration measurements are planned to identify and eliminate these local sources of vibration. In addition, the CFN measurements show that the installation of the NSLS-II storage ring and experimental hall will significantly stiffen the site. The floor vibration levels of the NSLS-II storage ring are then expected to be comparable to those of the other light source facilities.

7.2.3.6   Resonant Frequencies of the Girder Support System

Although the NSLS-II magnet–girder assembly fastened to the pedestals is a complex dynamical system, its important design features can be understood by a simple 1D oscillator shown in Figure 7.2.7a.
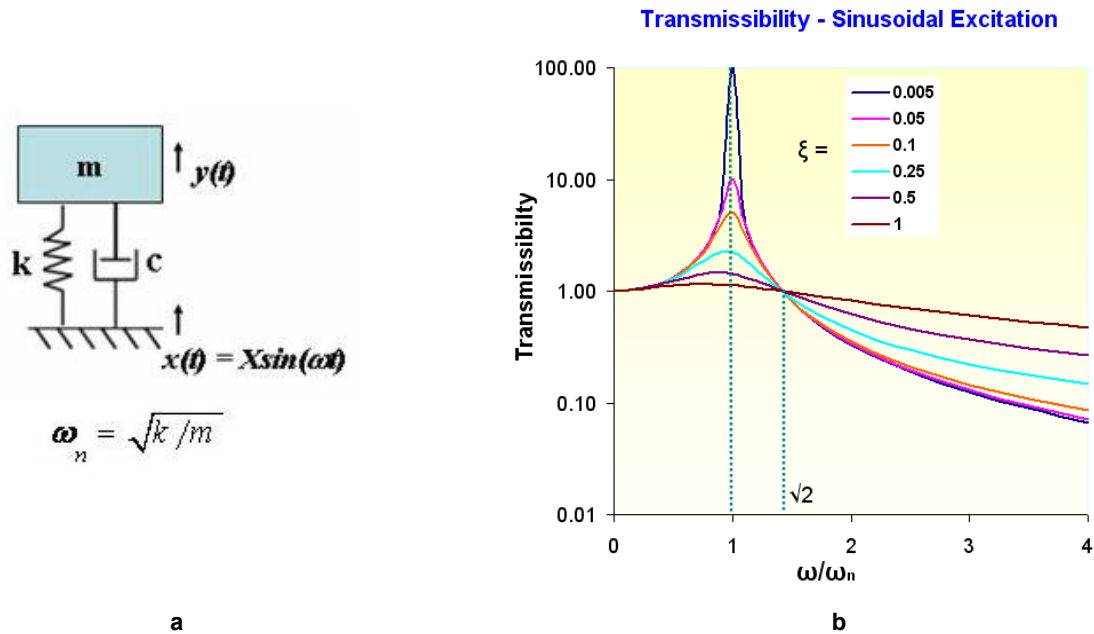
Figure 7.2.7 **a**) 1D oscillator; **b**) transmissibility plot.

For such an oscillator, the natural frequency is

$$\omega_n = \sqrt{k / m} \tag{7.2-3}$$

and the vibration amplification (or transmissibility) is given by

$$Transmissibility = Y / X = \sqrt{\frac{4\xi^2 (\omega / \omega_n)^2 + 1}{[1 - (\omega / \omega_n)^2]^2 + 4\xi^2 (\omega / \omega_n)^2}} \tag{7.2-4}$$

where the fraction of critical damping, ξ, is given by

$$\xi = \frac{c}{2\sqrt{mk}} \tag{7.2-5}$$

Transmissibility curves, obtained from Eq. 7.2-4 for different values of critical damping, ξ, are plotted in Figure 7.2.7b. There is no significant vibration amplification (transmissibility $\approx$ 1) when the natural frequency, ω_n, is substantially greater than the excitation frequency, ω. The ambient ground motion reduces sharply as $1/\omega^4$, as shown in Figure 7.2.6, and its amplification above 30 Hz can be ignored. Several investigations have been carried out on the dynamic response of the magnet–girder support systems using vibration measurements and finite element modal analyses. These studies have shown that it is quite difficult to raise the lowest natural frequency of the support system to greater than 20 Hz if elaborate alignment mechanisms are used either between the girder and its pedestals or between the girder and the magnets. When such alignment mechanisms are used, then the internal structural damping (ξ = 0.02 to 0.04) of the support

system is insufficient to reduce the floor motion amplification to an acceptable level. External damping devices, either active or passive, are then used, such as viscoelastic damping pads at APS and ESRF.

For the NSLS-II magnet–girder support system, a lowest natural frequency of greater than 50 Hz will be obtained by eliminating elaborate alignment mechanisms, and by lowering the beam height to 1 m. Short, stiff threaded rods will be used for height adjustment only. Transverse alignments will be made by precise but removable alignment mechanisms. Finite element model analysis of the NSLS-II magnet–girder assembly shows that the lowest two natural frequencies are 68.7 Hz and 94.3 Hz. The corresponding mode shapes, rolling and twisting of the girder, are depicted in Figure 7.2.8.
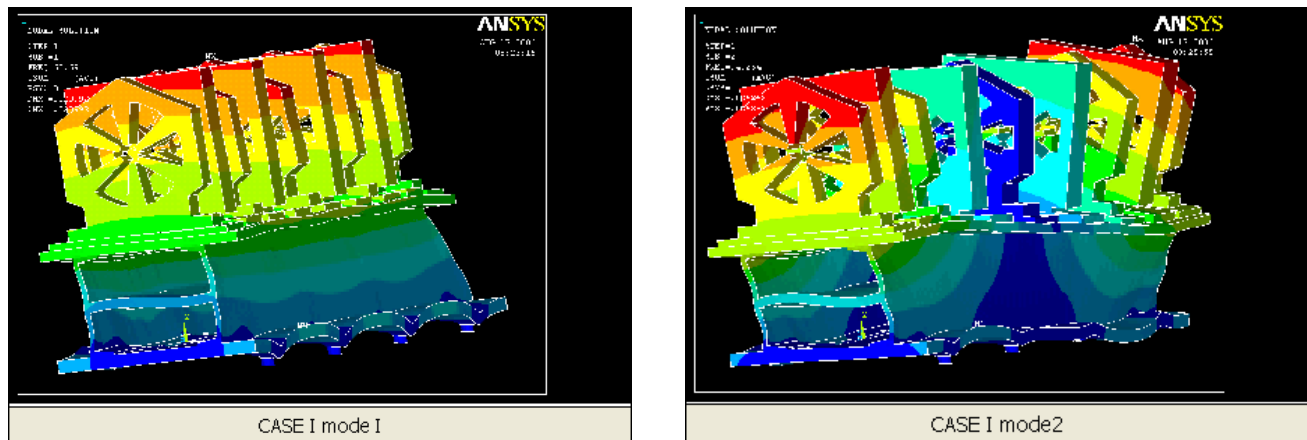

Figure 7.2.8 Mode shapes of the NSLS-II magnet–girder assembly: (left) First mode shape, rolling, ω_1 = 68.7 Hz. (right) Second mode shape, twisting, ω_2 = 94.3 Hz.

7.2.3.7   Flow-Induced Vibrations

Flow-induced vibrations of the water headers can be transmitted to the magnets and the vacuum chambers [7.2.6] by flexible hoses and pipes. The effects of flow-induced vibrations will be mitigated by paying close attention to several useful design guidelines, namely:

1. Locate all rotating equipments including fans, blowers, compressors, and pumps outside the storage ring tunnel, preferable tens of meters away from the tunnel floor and ceiling.
2. Keep low flow velocities (less than 2 m/s) in the process water headers.
3. Design header supports to minimize their vibration, such as by integrating viscoelastic dampers in the headers hangers, or by attaching headers directly to the ceiling.
4. Arrange water flow circuits and connection fittings such that sharp bends are eliminated. Special attention is to be given to the routing and clamping of the hoses and tubes that connect the magnets and vacuum chambers to their respective headers.

Analytical models and vibration measurements will be employed to ensure that flow velocities required to regulate the temperature of the vacuum chambers do not induce unacceptable level of vibrations.

7.2.3.8   Thermal Stability

Ambient temperature variations will result in displacements of both the magnets on the girders and the BPMs on the vacuum chambers [7.2.7]. To ensure acceptable thermal deformations of the ring components, process water and tunnel air temperatures will be maintained to within ±0.1ºC of their nominal values, 29.4ºC and 25.6ºC (85ºF and 78ºF), respectively. Air-conditioning temperature cycling of ~1-hour duration will be

maintained in order to take advantage of the thermal inertia of the support system. Thermal insulation of the girder will also be considered as an option to further reduce the effects of temperature transients.

Lowering the beam height from 1.4 m to 1 m would reduce the vertical thermal expansions of the assembly proportionately. In addition, over-constraining each girder to its pedestal at eight locations would minimize thermal bending effects.

7.2.3.9   R&D Program on Stability of the Magnet–Girder Support System

To further improve the mechanical stability performance of the girder support system, the following R&D tasks will be undertaken.

- real-time online measurements and analysis of the NSLS-II ambient ground motion.
- optimization of the stiffness of the magnet–girder assembly (A prototype assembly will be built for this purpose.)
- use of viscoelastic damping devices
- characterization and mitigation of the flow-induced vibrations of the magnets and the vacuum chambers
- investigation of the effect of process water and tunnel air temperatures on the field quality of the storage ring magnets
- assessment of insulating materials to reduce the effects of thermal transients in the tunnel

References

[7.2.1]   BETA USERS' GUIDE by L. Farvacque, T.F. Gunzel, J.L. LaClare, A. Ropert.

[7.2.2]   K. Tsumaki and N. Kumagai, "Vibration Measurement of the SPring-8 Storage Ring," IEEE, PAC, 2001.

[7.2.3]   L. Nikitina and Y. Nikitin, private communication on ALBA girders, August 13, 2006.

[7.2.4]   A. Temnykh, "The Magnetic Center Finding using Vibrating Wire Technique," CBN 99-22, Cornell University, May 26, 1999.

[7.2.5]   S. Sharma, C. Doose, G. Portmann, L. Zhang, K. Tsumaki, and D. Wang, "Ground Vibration Problems at the Light Sources," 22nd Advanced ICFA Beam Dynamics, SLAC, Nov. 6-9, 2000, SLAC-WP-18, pp. 37-48.

[7.2.6]   Nakazato, et al., "Observation of beam Orbit Fluctuation with Forced-Vibrating Magnets and Vacuum Chambers," MEDSI2002, Chicago, IL 2002.

[7.2.7]   L. Emery, "Measurements of Thermal Effects on the Advanced Photon Source Storage Ring Vacuum Chamber," MEDSI2002, Chicago, IL, 2002.

7.3　Beam Chambers and Vacuum Systems

7.3.1　Scope

The storage ring vacuum system provides and measures the acceptable vacuum pressure within the storage ring and front-end vacuum chambers. The storage ring vacuum system includes all vacuum chambers, vacuum pumps, vacuum valves, bake-out systems, and vacuum instrumentation and control. The storage ring vacuum system extends throughout the storage ring from the booster injection line-storage ring interface to the outer portion of the shield wall where the front end transitions to the user beamline. Vacuum system information for the linac-to-booster transport line, the booster, and the booster-to-storage ring transfer line is discussed in Chapter 5.

Many components such as shutters, photon absorbers, beam scrappers, insertion devices, etc. require or share storage ring vacuum, but only the components whose main purpose is to maintain, monitor, and control storage ring and front end vacuum are included in detail here. The other components are described in their respective sections. Due to many years of accumulated operational experience at NSLS and other synchrotron radiation facilities, a design approach that provides optimal performance at minimal cost will be pursued.

The storage ring vacuum pressure with beam is designed to be less than 1×10^{-9} Torr. At this pressure level, the beam lifetime due to bremsstrahlung and Coulomb scattering is longer than 10 hours. The stored beam lifetime for 500 mA operation will be limited to 2–3 hours by the Touschek lifetime due to the scattering loss of electrons in the bunch. The designed pressure level will provide ample beam lifetime with minimal radiation and beam loss effects.

To achieve the low thermal outgassing and low photon-stimulated desorption, all the vacuum vessels and appendage vacuum components will be made from ultra high vacuum compatible materials. All the vacuum components will be carefully prepared, cleaned, and conditioned using UHV compatible processes.

7.3.2　Mechanical Design

7.3.2.1　Design Overview

There are 30 cells in the storage ring. Each vacuum cell consists of five basic chambers; an upstream straight chamber, a dipole chamber, a mid-section straight chamber, a second dipole chamber, and a downstream straight chamber. There are RF-shielded bellows connecting the chambers. There is a long straight section either 5 m or 8 m long between the cells, for insertion devices and for special components such as RF cavities, injection devices, damping wigglers, and so forth. A typical vacuum cell layout is shown schematically in Figure 7.3.1. The dipole magnet chambers are approximately three meters long and the straight chambers for the multipole magnets 4 to 5 m long. All-metal, RF-shielded gate valves will be employed to isolate each of the 30 cells and the long straight sections between cells.
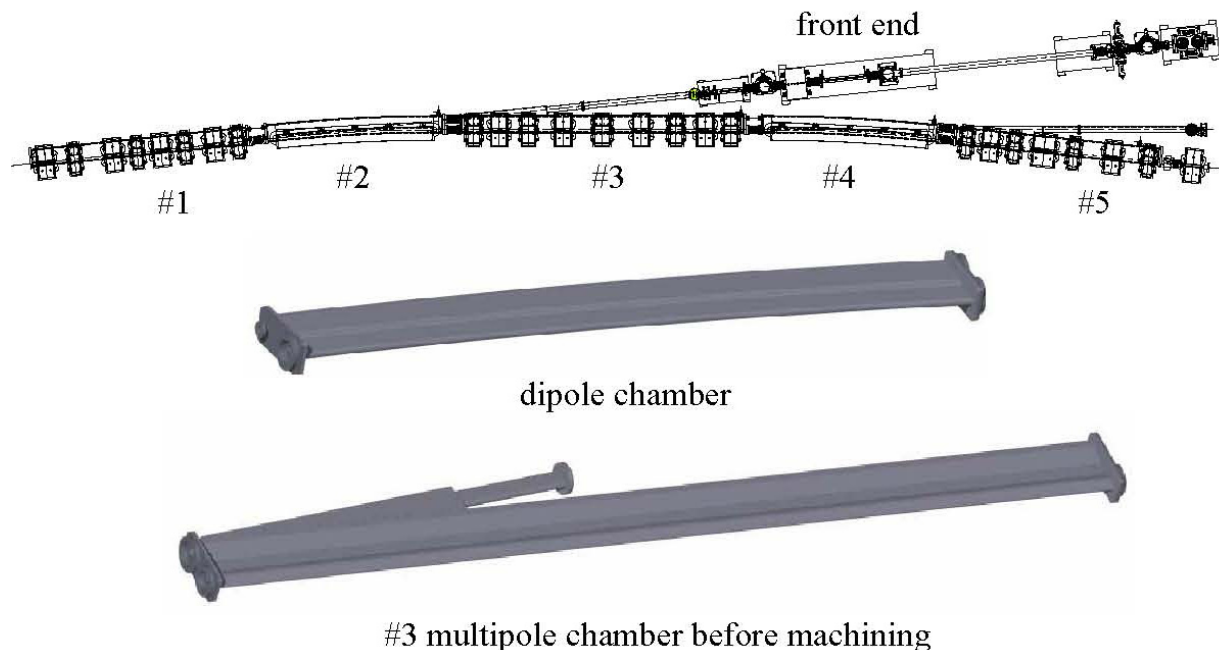
Figure 7.3.1   The layout of the five vacuum chambers in a typical synchrotron cell with two photon exit ports; and the 3D models of dipole magnet chambers, and the #3 straight chamber for multipole magnets.

Most of the storage ring chambers will be made of extruded aluminum with a cross-section similar to that of the APS chambers [7.3.1]. Conflat flanges with copper gaskets will be used throughout the vacuum systems, except for the flanges and seals for beam position monitor buttons, where Helicoflex delta seals will be employed. Water-cooled copper or Glidcop absorbers will be positioned in the storage ring vacuum chambers to absorb the unused photons and high heat loads. The entire set of vacuum cells will be in-situ bakeable to 150°C to remove adsorbents and contaminants. Vacuum bake for the aluminum chambers will be at 130°C using pressurized hot water circulated within the cooling water channels. External heating jackets will be used for the bakeout of the appendage vacuum components.

To achieve fast conditioning after intervention, sufficient pumping capacity is needed. The chambers will use sputter ion pumps, non-evaporable getters (NEGs), and titanium sublimation pumps (TSP) for their main UHV pumping. Following rough pumping, in-situ vacuum bakeout is required, to remove contaminants. Provisions for vacuum bakeout are therefore necessary, and the careful selection of vacuum chamber materials and all other materials that are directly in contact with the vacuum chambers is important. The vacuum chamber design must provide provisions for stability during bakeout and be made with sufficient precision for accurately locating the vacuum chambers and BPM buttons after bakeout. The impedance of the vacuum chamber should be low enough so as not to excite higher-order mode resonances. Smooth cross-sectional transitions between components are required, as are flexible interfaces such as RF-shielded bellows between cell chambers and insertion devices. The design parameters of each vacuum system component must be considered separately and as a whole, as each parameter affects the performance of the overall storage ring vacuum system.

7.3.2.2   Vacuum Chamber Design

The electron beam vacuum chambers differ according to their location within the storage ring. The vacuum chambers will provide adequate ports for heat absorbers, BPM buttons, pumps and exit ports to the front ends. A pronounced antechamber design similar to that of APS [7.3.1] will be used to better distribute vacuum pumping capability. The cell vacuum chambers contain two distinct but connected channels; the

beam channel portion must be continuous, but the antechamber portion may be interrupted at various locations for vacuum valves, bellows, insertion devices, and other devices where the mechanical requirements constrain the use of the antechamber. Ports emanating from the cell chambers will use bi-metal Conflat flanges. The internal beam chamber cross-section will be elliptical, 25 mm vertical by 76 mm horizontal, to allow sufficient beam-to-chamber clearance, except at absorbers, which insert to 25 mm from the storage ring centerline at the outboard side to intercept some unused photons. The antechamber portion of the vacuum chamber is sized for distributed NEG pumping and to fit within the magnets. A slot connecting the beam channel and antechamber portions of the vacuum chamber is sized as large as possible according to the physical requirements of the magnets that the vacuum chamber passes through, and according to constraints given by the wall strength requirements for the vacuum chamber. The chamber cross sections inside the dipole, quadrupole and sextupole magnets are shown in Figure 7.3.2. There will be at least 2 mm clearance between chambers and magnet poles and coils at the closest points to allow adjustment in the chamber supports as well as during in-situ bake. The extruded chamber cross sections and the cross sections after machining are given in Figure 7.3.3. The ANSYS analysis of the stress and deflection due to atmospheric pressure load of the multipole chambers at the sextupole location, which has the thinnest wall, is shown in Figure 7.3.4, with maximum stress of 135 MPa and maximum deflectors 0.6 mm × 2. However, a 3D ANASYS analysis gives maximum stress of 94 MPa and maximum deflection of 0.3 mm × 2, because the chamber wall is machined down to 2.9 mm only at the sextupole locations.
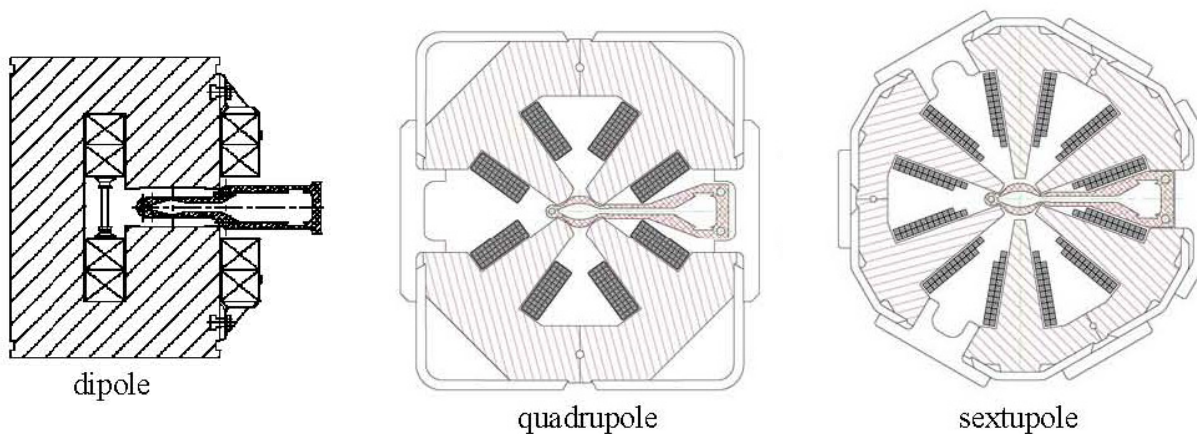

Figure 7.3.2 Storage ring vacuum chamber and magnet cross-sections at dipole, quadrupole, and sextuple interfaces. The beam channel will have a minimum aperture of 25 mm (V)×76 mm (H).

A list of storage ring vacuum chambers for the storage ring is given in Table 7.3.1.
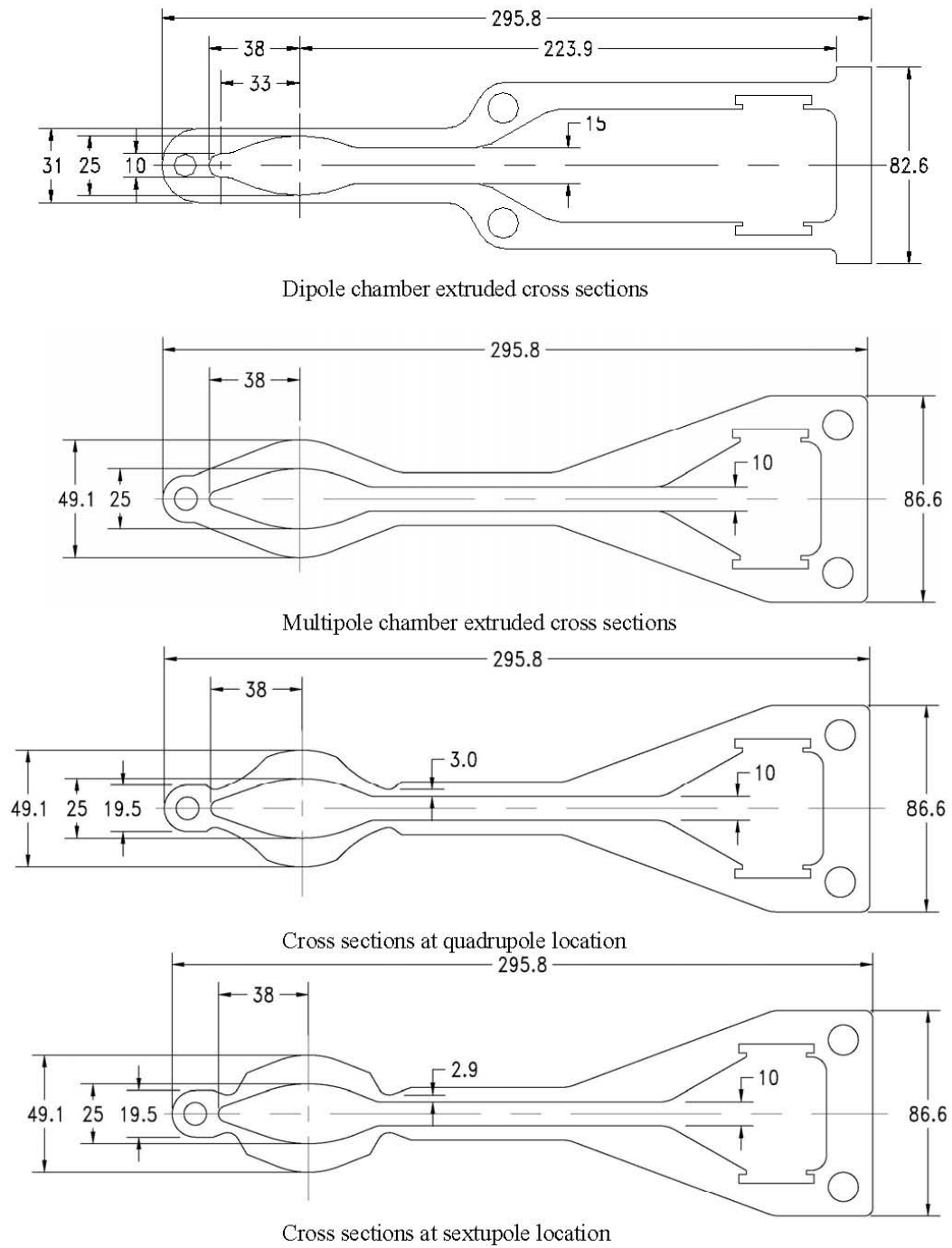
Figure 7.3.3   Storage ring vacuum chambers at dipole, multipole, quadrupole, and sextupole interfaces. The minimum wall thickness at the sextupole location is ~2.9 mm.
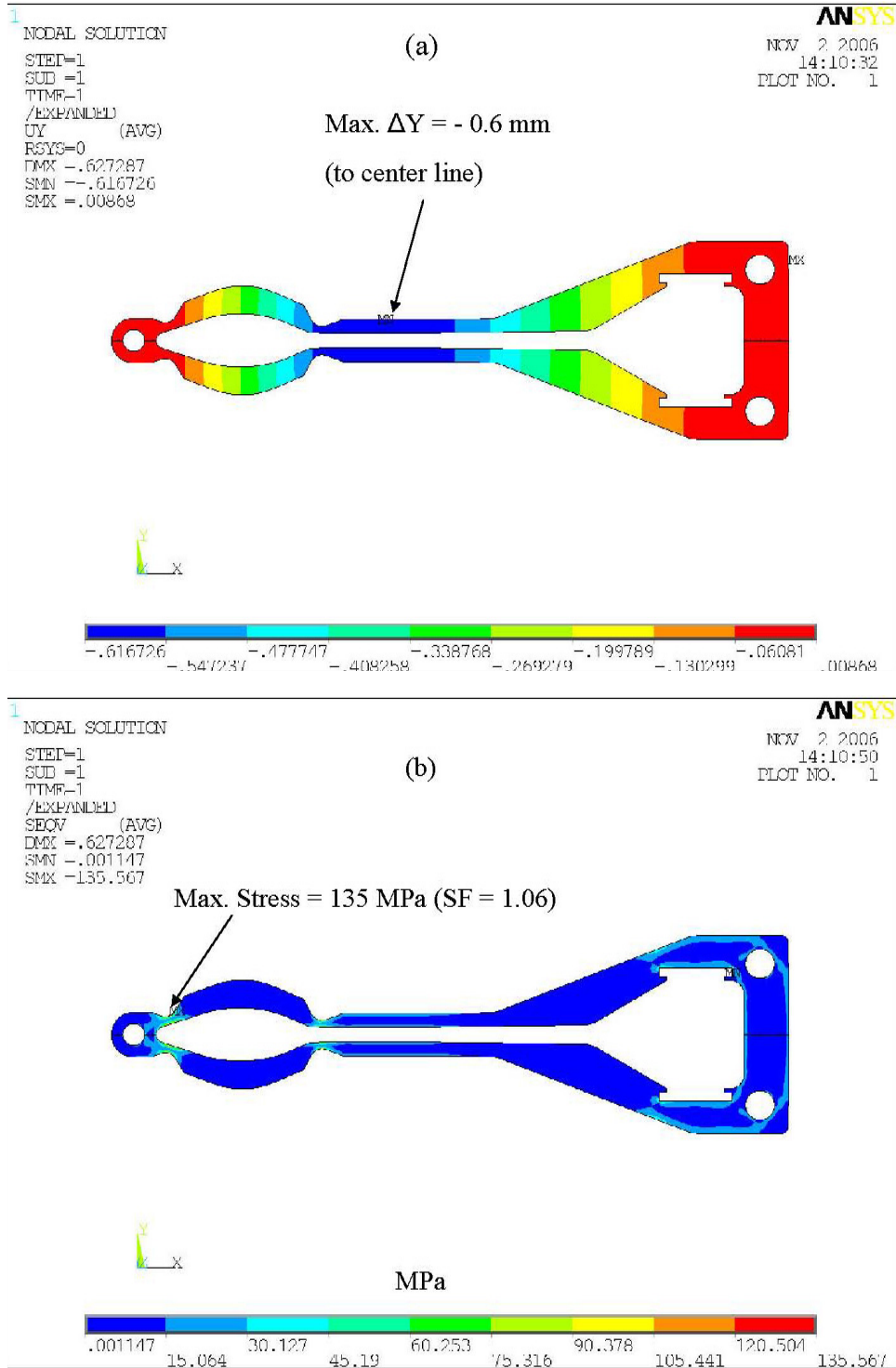
Figure 7.3.4 ANSYS analysis of the deflection and stress of the multipole chamber at the sextupole pole tip locations where the wall thickness is 2.9mm, **a)** the maximum deflection due to atmosphere pressure load is found to be 0.6 mm×2; and **b)** the maximum von Mises stress at this single point is 135 MPa, within the maximum allowable stress of 144 MPa.

Table 7.3.1   Types and Numbers of Vacuum Chambers, Absorbers, and RF-Shielded Bellows in the NSLS-II Storage Ring at Start of Operations.

Description - Type	Length (m)	Quantity
Cell – Bending - #2, #4	3.0	60
Cell – Straight – #1	3.7	30
Cell – Straight – #3	4.8	30
Cell – Straight - #5	4.3	30
Cell – RF–Bellows	0.3	120
Cell - Absorber		210
ID – CPMU & EPU	~4	5
ID – Damping wiggler	~7	3*
ID – SRF cavity	~7	2
ID – Injection kickers + septum	~7	1
ID – Empty 5 m straight	~4	10
ID – Empty 8 m straight	~7	9*
ID – RF-Bellows	~0.3	~60

* Two 4 m beampipes will be used at each 8 m long straight.

7.3.2.3   Pumping at the Photon Absorbers

There are several discrete photon absorbers, as described in Section 7.7.2, in each vacuum cell to intercept and absorb unused photons from the two bending magnets and the upstream insertion devices. The absorbers are located as far from the source of the photons as practicable, to reduce the power density, and thus the peak temperature on the absorber surface. Sputter ion pumps with either NEG cartridges or TSPs will be located at the absorbers to remove as much desorbed gas as possible, thus minimizing the amount of gas diffused back to the beam channel. The maximum gas load from each absorber for the bending magnet radiation is estimated to be $\sim 1 \times 10^{-6}$ Torr-l/s, as described in Section 7.3.3.2, and can be handled with the combination of a sputter ion pump and titanium sublimation pump. The absorber for the DW radiation fan will intercept ~ 10 kW of photons, resulting in a gas load of 7×10^{-6} Torr-l/s. This high gas load at the DW absorber will be pumped by the combination of a sputter ion pump and a NEG cartridge pump, which has higher capacity than a titanium sublimation pump.

7.3.2.4   Injection Kicker and Front-End Chambers

Kicker magnets require special ceramic vacuum chambers. The four ceramic chambers will be located in the injection straight section, upstream and downstream of the injection septum magnet to correct the electron beam path as needed during injection to the storage ring. These chambers will be specially designed so that they are able to 1) withstand the stresses of fast magnet actuation, 2) resist fatigue, and 3) maintain vacuum integrity. The internal surface of the ceramic chambers will be coated with a conductive film to reduce impedance for the beam image current and prevent charge buildup [7.3.2]. The film must be thin to minimize the eddy current induced by the fast-pulsing kicker field so as not to disturb the injected beam. A thin window may be used at the injection septum to separate the transport line high vacuum from the storage ring UHV.

There are two photon exit ports at each vacuum cell to extract proper photon beams to the user beamlines: one at straight Chamber 3 for photon beam originating from the upstream insertion device; and the second at the upstream end of straight Chamber 5 for photons from bending magnet 4. The front ends of these exit ports will have high heat load components to intercept the photons before the beamlines are installed or when the beamlines are not in use. The front ends will consist of photon masks, safety shutters, heat absorbers, and fixed and adjustable slits. Vacuum gate valves will also be located in the front ends to allow vacuum isolation of components as needed for maintenance and troubleshooting. The front-end vacuum chambers will be made

of stainless steel. Sputter ion pumps with TSP will be placed in each front-end section as close as practical to the gas sources at the photon mask, safety shutter, and absorbers. Vacuum gauges and residual gas analyzers will be installed at each front end to monitor vacuum quality. Radiation shielding will also be installed at front ends to protect downstream equipment and personnel.

7.3.2.5   RF-Shielded Bellows, Flanges, and Ports

To reduce the broadband impedance of the vacuum chamber wall and to minimize the localized HOM heating, the inner cross-section of the electron-beam chamber should be maintained as smooth as possible. High transverse impedance may cause beam instability, which might put an upper limit on the stored current. The changes in cross-sections of the beam chamber should vary smoothly, with an angle of inclination less than 1/5 for tapered transitions. The height of the steps should be less than 1 mm, in general, and less than 0.5 mm at small-aperture ducts for insertion devices. For vacuum components with cavity-like or discontinuous structure, such as flange joints and bellows, RF contact fingers will be installed to reduce the impedance and provide a smooth path for the beam image current. The opening of the thin slits of these fingers should allow enough pumping of residual gases from behind the slits. Calculations will be made to optimize the design of the thin slits while minimizing the impedance of the chambers. Slots or screens will be implemented at the ports of some ion pump locations to reduce impedance and still provide adequate vacuum pumping. Only RF-shielded gate valves, commercially available, will be used along the storage ring beam channel.

Two types of RF-shielded bellows will be studied for their finger contact force, flexibility, cost, and vacuum and RF properties: the single-finger type with hydro formed bellows used at APS [7.3.3], and the double-finger type with welded bellows used at B-factories and a few SR facilities in Asia. They are shown in Figure 7.3.5. The welded bellows will allow more compression and lateral movement than the hydro-formed ones. The double-finger design may not be as reliable as the single-finger type, but does offer lower contact resistance. The magnetic permeability of both welded and formed bellows must be measured and the eddy current effect calculated, since fast corrector magnets will be mounted at some bellows. The welded bellows will cost more than the formed ones.
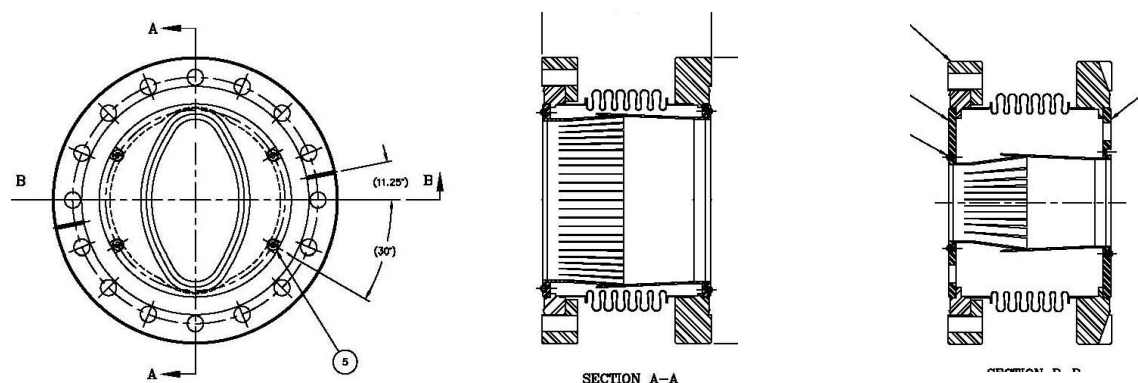
a

b

Figure 7.3.5.   Two types of RF-shielded bellows: (a, upper row) the ones with welded bellows used in B-factories and BEPC-II with single or double fingers; and (b, lower row) the APS type with single fingers and hydro formed bellows.

Explosion-bonded bi-metal transition flanges, made from 316L stainless steel and A6061-T6 aluminum plates, will be used for the aluminum chambers throughout the storage ring. These Conflat type flanges with aluminum weld neck will be tungsten-inert-gas welded to the cell chambers using a robotic welding machine. They have the standard stainless steel knife-edge sealing face for the copper gaskets and are commercially available. They will form reliable, leak-tight joints with other bi-metal flanges and standard stainless steel flanges of adjacent chambers, bellows and other appendage vacuum components, such as vacuum pumps and gate valves. The bi-metal joints can be in-situ baked up to $250^{\circ}C$.

7.3.3   Pressure Requirements and Distribution

As mentioned earlier, an average beam channel pressure of less than 1×10^{-9} Torr is needed. This pressure will provide ample beam-gas lifetime with minimal radiation and beam loss effects. Beam losses generate radiation according to electron current, energy, and vacuum pressure. At pressures greater than 10^{-9} Torr, both the stored beam lifetime and the life of many of the vacuum pumps will be reduced. Titanium sublimation and NEG pumps have lifetimes that are directly related to the operating pressure; therefore, maintaining this vacuum level in the storage ring improves vacuum component life, stored beam life, and minimizes the amount of radiation produced from bremsstrahlung scattering.

The beam gas scattering loss in the NSLS-II storage ring will depend largely upon the interaction of the beam with heavier residual gas molecules such as CO, CO_2, and Ar due to bremsstrahlung and Coulomb scattering. The gas density inside the vacuum chamber is determined by the installed pumping and by the surface condition of the vacuum chambers and the absorbers, which is bombarded by photons (synchrotron

radiation) generated by the circulating electron beams. During initial ring commissioning, there are severe limitations on the achievable beam current and stored beam lifetime, caused by large pressure increases due to gas species from Photon-Stimulated Desorption. Experience gained during early commissioning of the NSLS x-ray ring showed that residual gas spectra obtained with no stored electrons were typical of a well-baked UHV system. Hydrogen constituted approximately 95% of the residual gas at that time, and the average vacuum was in the 10^{-10} Torr range. The composition of the desorbed gases during initial operation of the x-ray ring was 43% H_2, 25% CO, and 16% each of CO_2 and CH_4. After three months of additional beam conditioning, the PSD rate dropped by a factor of five, and the CO, CO_2, and CH_4 peaks represented much smaller percentages of the total desorbed gas. The PSD rate versus beam conditioning dosage for copper and aluminum chambers [7.3.4, 7.3.5], as measured at NSLS, is shown in Figure 7.3.6. Typical desorption yields after 100 A/hr beam conditioning are used in the pressure simulation. The beam lifetime did not show a corresponding increase with the reduced desorption rate, however.
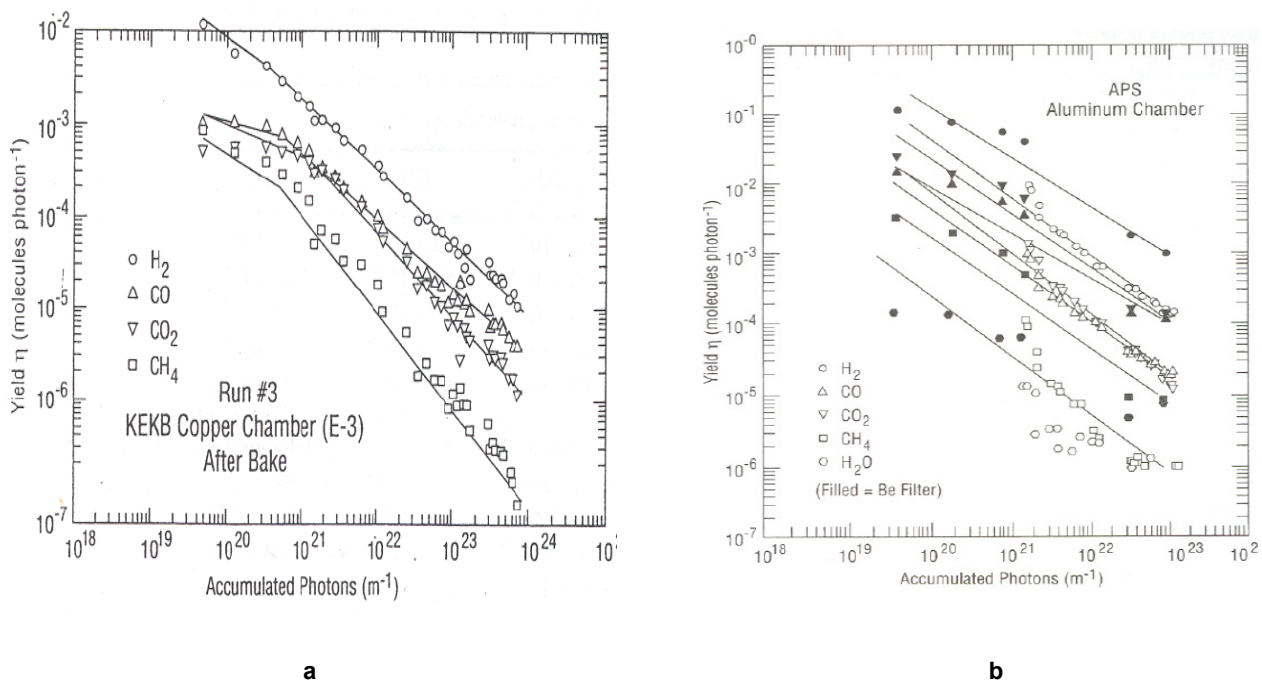

a

b

Figure 7.3.6   Comparisons of PSD yields with photon dosages for copper and aluminum. **a)** PSD yields for a 1 m pure copper sample beam chamber at KEKB. **b)**   PSD yields for a 1 m extruded aluminum sample beam chamber at APS.

Most of the NSLS-II storage ring vacuum chambers will be fabricated from extruded aluminum and may be exposed to low levels of bending magnet photon radiation. Almost all unused photons will be incident on specially designed water-cooled absorbers. After NSLS-II commissioning and operation, copper, stainless steel, and aluminum PSD will be at almost the same levels.

The 25×76 mm electron beam channel is vacuum pumped using distributed NEG strips in the ante chamber connected by a narrow pumping slot. Two NEG strips are installed in the extruded ante chamber and have a combined pumping speed of 240 l/s/m. The NEG pumps only chemically active gases. Sputter ion pumps are employed to pump the inert gases not pumped by the NEGs. The SIPs are located under the photon absorbers where the majority of PSD occurs. The SIPs provide 400 l/s pumping and are part of a combination SIP/TSP. The TSP provides an additional 500 l/s of pumping for active gases.

Conductance of the electron beam channel is 8 l/s/m. The connecting slot in the extrusion between the NEG ante chamber and the dipole beam chamber is 15 mm high and limits the NEG pumping speed to about

150 l/s/m, in the beam channel. The slot in the extrusion for the quadrupoles and sextupoles is 10 mm high, which yields a conductance of approximately 110 l/s/m in the beam channel.

7.3.3.1   Static Vacuum: Thermal Outgassing

The static pressure distribution in the storage ring will be determined by the amount of thermal outgassing from the internal surfaces in the vacuum chambers. These outgassing rates will depend on the construction materials used and their preparation. After precision cleaning, the chambers will be vacuum-baked and may be glow-discharge conditioned to reduce outgassing and remove contaminants prior to their final assembly into the storage ring magnets and girders. All the chambers and vacuum components in the vacuum cell will be in-situ baked, again to reduce the thermal outgassing. Most of the internal vacuum surfaces along the storage rings are aluminum. The contribution of other materials to the thermal outgassing load is much smaller than that of aluminum wall. Vacuum-baked aluminum outgassing of 1×10^{-12} Torr-l/s/cm^2 is used for thermal gas load modeling. The total thermal gas load is estimated to be 6×10^{-6} Torr-l/s.

7.3.3.2   Dynamic Vacuum: Photon Stimulated Desorption

During operations with stored electrons, specially designed water-cooled Glidcop absorbers will intercept most unused synchrotron radiation. The PSD rate η for vacuum-baked copper and Glidcop has been studied at NSLS [7.3.4] and at other laboratories. An η value of 2×10^{-6} molecules per photon is used for the modeling calculations [7.3.6]. The total photon flux from the storage ring dipole magnets is calculated using Np (ph/s) = $8\times10^{+20}$ [E(GeV)] [I(Amperes)]. For 3 GeV and 500 mA, the total photon flux is $1.2\times10^{+21}$ ph/s. Using these values and converting to gas load yields 7.5×10^{-5} Torr-l/s (or $\sim1.2\times10^{-6}$ Torr-l/s per bending magnet). Thus the total estimated gas load, for both thermal and bending magnet PSD, is 8×10^{-5} Torr-l/s. The undulator radiation will have a narrow fan. It will mostly be collimated and intercepted down at the front end and beamline, and will produce little gas load to the storage ring beam channel. In contrast, the damping wiggler radiation will have a relatively wide fan. Approximately 15% of the DW radiation will be intercepted by the crotch absorber located upstream of the #3 multipole chamber, equivalent to $\sim1\times10^{+20}$ ph/s by each DW. Assuming the same η value of 2×10^{-6} molecules per photon, this corresponds to an additional gas load of 7×10^{-6} Torr-l/s from each DW.

7.3.3.3   Dynamic Pressure Distribution

The pressure rise with beam operation will be determined by the PSD of gases from internal surfaces of the vacuum chamber, and the amount of dynamic pumping. Most synchrotron radiation will be intercepted by water-cooled Glidcop absorbers, which are located downstream of bending magnets and insertion devices. The pressure distributed in a super-period of 52 m was calculated using both Molflow [7.3.7] and Vaccalc [7.3.8] software. The storage ring pressure distribution in the beam channel with 500 mA stored beam current, with no beam current, without TSP, and with only 50% NEG strip coverage, is plotted in Figure 7.3.7. PSD yield of 2×10^{-6} mol/ph, reached after approximately 100 amp-hours of beam conditioning, is used in the calculation. The design average pressure of less than 1×10^{-9} Torr can be reached with the current pumping scheme of distributed NEG, lumped ion pumps, and TSP. The significance of the distributed NEG is clearly illustrated, i.e., a 50% decrease in NEG coverage results in a five-fold increase of average pressure in the electron beam channel. The comparison of the pressure distribution in super-periods with and without DW is illustrated in Figure 7.3.8. The crotch absorber for DW radiation produces a sharp but localized pressure peak, but only a 10% increase in average pressure for that super-period.
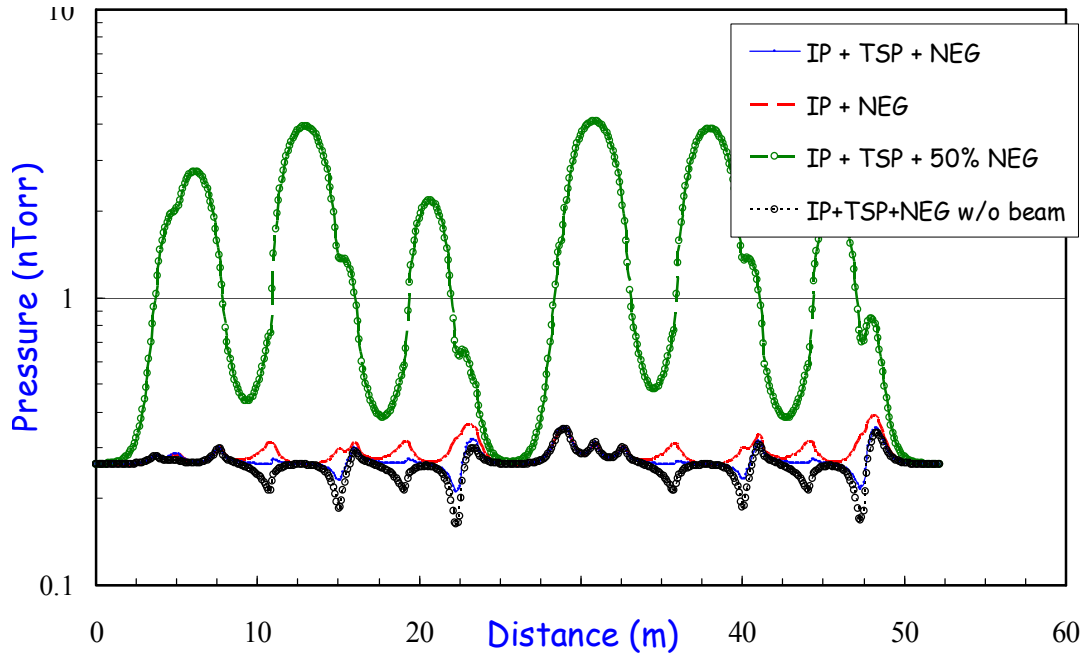
Figure 7.3.7 Pressure distribution inside the electron beam channel in one storage ring super-period without beam (black circles), with 500 mA current (blue line), without TSP (red line), and with 50% NEG strip coverage (green circle). The average pressure is at ~3×10^{-10} Torr, except when 50% NEG strips are removed, where the average pressure increases five-fold, to 1.5×10^{-9} Torr.
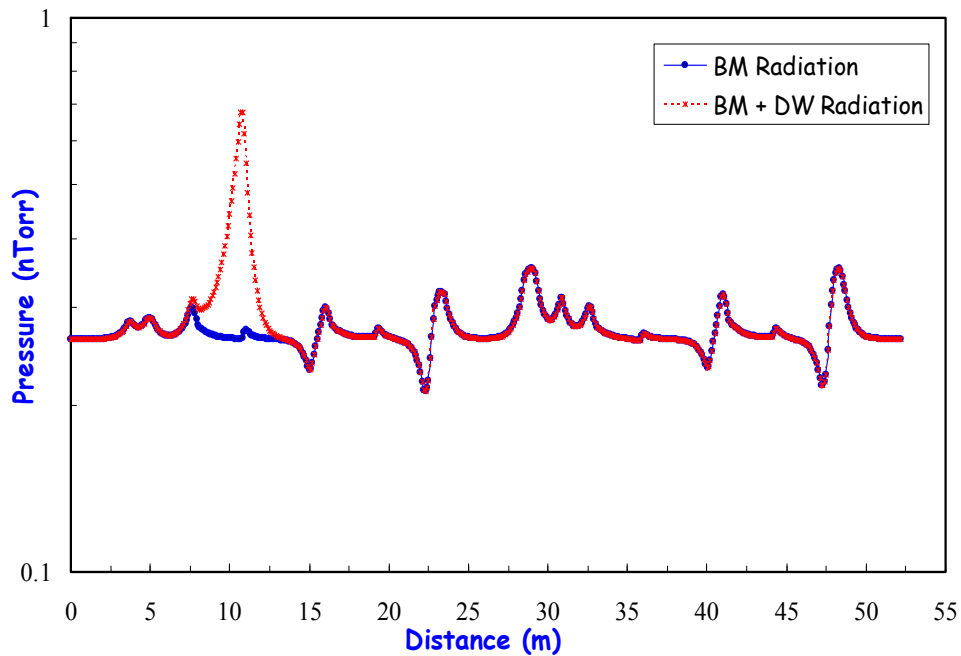

Figure. 7.3.8 Pressure distribution inside the electron beam channel in one 52 m super period with and without a damping wiggler. The crotch absorber intercepting the DW radiation generates a localized peak pressure with a 10% increase on the average pressure.

7.3.4 Vacuum Chamber Materials, Fabrication, and Treatment

Most of the storage ring vacuum chambers will be constructed from extruded A6063-T5 aluminum. This alloy was selected based on a comparison of various properties for commonly used vacuum chamber materials, as described below.

7.3.4.1 Selection of Chamber Materials

There are three common UHV materials suitable for the vacuum chambers of the electron storage ring: stainless steel, aluminum alloys, and OFHC copper, with stainless being preferred for a few new SR facilities in Europe, and aluminum for the new ones in Asia and the U.S. Copper was chosen for storage rings with high energy and high power density, such as the B-factories at SLAC and KEK, and also for its high thermal conductivity and radiation shielding properties. However, copper has the disadvantages of high material and fabrication costs. For the 3 GeV NSLS-II, radiation shielding and thermal conductivity requirements are not as critical as in the higher energy machines. Moreover, most synchrotron radiation from bending magnets will be removed by discrete copper or Glidcop absorbers. Therefore, copper has not been considered a preferred chamber material. The choice between stainless and aluminum for the NSLS-II cell chambers is based on experience at NSLS and APS, plus aluminum's vacuum and mechanical properties, ease of fabrication, and relatively reasonable cost.

One major difference between NSLS-II and other new SR facilities of comparable energy is the large bending magnet radius. The photon fan from the bending magnet will have a small dispersion and will be easily intercepted by discrete absorbers. This allows a narrow chamber geometry design; therefore, the cell chambers can be fabricated from extruded aluminum with uniform cross-sections. The need to accommodate the distributed NEG pumping also favors extruded aluminum, since an antechamber can easily be produced by aluminum extrusion. The cost of extrusion is considerably lower than that of chambers made of stamped stainless plates or machined aluminum plates, although the cost of machining the external chamber profile to fit the magnet poles and the various access ports will be significant. A few important arguments concerning the choice of material are listed and further discussed below.

Table 7.3.2   Electron Storage Ring Chamber Materials and Their Critical Properties.

Specifics	Aluminum	Stainless	Copper
Initial PSD rate	High	Low	Average
Mechanical strength	Acceptable	Excellent	Good
Thermal expansion	Large	Small	Small
Thermal conductivity	Excellent	Poor	Excellent
Weldability	Good	Excellent	Good
Beam impedance	Low	High	Low
Bi-metal flanges	Yes	No	Yes
Cooling channels	Extrusion	Brazed	Brazed
Fabrication cost	Low	Average	Expensive
Ease of in-situ bake	Good	Poor	Good
Radiation shielding	Poor	Average	Excellent

The outgassing of unbaked aluminum is higher than that of stainless, but an in-situ baked aluminum surface has similar or lower outgassing than that of stainless. The initial PSD rate of an aluminum surface is higher than those of copper and stainless. However, aluminum conditions faster and will reach the same PSD rate at a modest integrated beam dosage. The high thermal conductivity of aluminum offers distinct advantages over stainless, both during the in-situ bake and during normal operation. No conductive coatings or strips are needed on aluminum to reduce the chamber wall impedance, whereas stainless chambers may need copper strips and absorbers in certain locations and for mis-steered beam. Therefore, our preferred material to form the cell chambers through extrusion is aluminum A6063-T5 alloy. Stainless-to-aluminum bi-

metal Conflat flanges will be welded to the aluminum chambers, and standard copper seals can be used to form reliable joints between the chambers, bellows, and appendage components.

7.3.4.2   Vacuum Facility

To ensure the necessary chamber surface properties, cleanliness, mechanical quality, and leak tightness, vacuum facilities will be needed for cleaning, welding, assembling, and evaluating the vacuum chambers and other vacuum components for the storage ring and injectors. A dedicated chemical cleaning facility is required to clean the long chambers and other vacuum components. It will consist of four long, stainless steel tanks and a gantry crane capable of handling chambers up to 6 m long and 200 kG in weight. These tanks will provide ultrasonic cleaning with hot water, commercial bio-degradable cleaning agents, and de-ionized water rinse, and are suitable for aluminum, copper, inconel, and stainless chambers and materials. The exact cleaning recipe and process will be based on the chamber material and experience developed at other SR facilities such as NSLS and APS. Programmable robotic welding stations with laminar flow hoods will be set up to weld the cleaned chambers, the sub-assemblies, and the flanges. A Class 1000 clean room with ~100 m^2 floor space is needed for the assembly of the chambers with distributed NEG strips, ion pumps, gauges, absorbers, BPM buttons, and other components.

A facility with these capabilities was established at Argonne National Laboratory for the construction of the Advanced Photon Source. The NSLS-II project is evaluating the potential benefit of using the ANL/APS facility for the production, chemical cleaning, and automatic welding of the cell chambers of the NSLS-II vacuum system. Should this prove impractical for some reason, equivalent facilities will be established at BNL. Even if the ANL vacuum facility is utilized, a small chemical cleaning facility is still needed at BNL for storage ring and beamline vacuum components. The clean room and vacuum bakeout/evaluation stations are still required at BNL for the final assembly and evaluation of the cell chambers. If we do not utilize the APS facility and need to establish all of the capabilities at BNL, then ~2,000 m^2 of space would be required. If the ANL facility is used for production, cleaning, and welding, then ~1,400 m^2 would be required. Building 905 at BNL has been identified as the preferred location for the BNL vacuum facility. This building has more than 2,500 m^2 of space, as well as overhead cranes, and is available for use by the NSLS-II project.

7.3.4.3   Fabrication, Assembly, and Evaluation

Most of the storage ring chambers will be made of extruded aluminum. Immediately after extrusion, the long chamber sections will be stretched to obtain the uniform cross-section and to meet the dimensional requirement. They will then be cut to the designed length. The bending chambers will be formed to the curvature on a hydraulic press with a die of correct radius. To preserve the internal cross-sections, the inner volume of the bending chambers will be filled with DI water and frozen prior to the forming operation. The extruded chambers will be machined at industrial vendors to the appropriate external profiles and to add photon exit ports, access ports for BPM buttons, pumps, absorbers, and other vacuum components. The chambers will then be cleaned at the chemical cleaning facility and sealed in an aluminum bag filled with dry nitrogen gas for storage and further processing.

The aluminum chambers and flange adaptors are welded together with tungsten-inert-gas welding processes, using programmable robotic welding machines. The relative humidity of the laminar hoods over the welding zones will be reduced to less than 50% during welding to minimize oxide growth at the heat zone and to ensure weld integrity. Following welding, the vacuum chambers will be pumped down with a TMP backed by a dry mechanical pump, then checked for leaks using a leak detector with minimum helium sensitivity of 5×10^{-11} Torr-l/s. Specific procedures for repairing each type of weld leak will be developed to ensure that the quality of the chambers is not compromised. The cooling water channels will be leak-checked with vacuum and by sniffing while pressurized. The welded chambers are then brought into the Class 1000 clean room for assembly of peripheral components, such as BPM buttons, NEG strips, pumps, absorbers, and gauges. The chamber end flanges will then be capped with blank flanges.

The assembled chambers will be installed at the evaluation stands for final leak checking and bakeout at 130°C using temporary ovens. The vacuum level and the residual gas composition will be closely monitored during the bakeout, using vacuum gauges and RGAs, to ensure that the chambers remain leak-tight and are free of contaminants. All the pumps, gauges, BPM buttons, absorbers, and thermocouples are to be activated and measured to ensure their proper operation during the bakeout cycle. The possible use of a DC glow-discharge system to clean internal surfaces with an Ar/O_2 mixture during bakeout will be investigated for its merit versus the technical complexity and cost. After bakeout, the chambers will be either at storage vacuum or back-filled with dry nitrogen for the subsequent assembly into magnets and installation in the SR tunnel.

7.3.4.4   Installation, Alignment, and In-Situ Baking

During the machining of the vacuum chambers, all mounting holes for the survey fiducials will be checked against the beam channel cross-sections and the BPM mounting surfaces. To ensure precision alignment, the design of the vacuum chambers and the proposed alignment schemes will be reviewed and approved by the diagnostics, accelerator physics, and alignment and support groups. The required precision of the chamber alignment is ≤0.5 mm in general, and ≤0.1 mm for special parts such as the BPM buttons. The assembled and tested chambers will be installed into the split magnets and aligned using built-in adjustment bolts of the fixed support plates mounted on the girder. After the installation and alignment of individual chamber/magnet girders in the tunnel, the end capping flanges will be removed and the RF-shielded bellows will be installed and connected to the next cell chambers. Two sector gate valves will be mounted and supported on the end flanges of the #1 and #5 chambers of each cell. The magnet buses, cooling water lines, and vacuum equipment cables will then be connected prior to final measurement, pump down, leak check, and in-situ bakeout.

The in-situ bakeout of the storage ring cell in the tunnel will be carried out with pressurized hot water provided by the SR utility system. Additional heating jackets, heating tapes, and thermal insulation are needed for large appendage components, such as gate valves, ion pumps, etc., to ensure uniform temperature distribution, especially at large flange joints where uneven temperatures may result in seal failure and vacuum leaks. The supports for the chambers and the pumps must be adjusted to allow thermal expansion during the bake, while still maintaining and protecting the mechanical stability of the entire system. The storage ring cell will be pumped down with a turbopump backed by a dry mechanical pump during the bakeout. The vacuum level and gas composition will be continuously monitored using cell vacuum gauges and RGAs during the bakeout. The temperature of the chambers will be raised slowly by the hot water system and the heating jackets, and controlled by the bakeout programmable logic controller with inputs from the installed thermocouples on the chamber surface. The entire vacuum cell will be baked at $130°C$ for 40 hours to remove absorbed water and other contaminants from the surfaces. The sputter ion pumps, the titanium sublimation pumps, the NEG strips, and NEG cartridges will be degassed during the bake, then activated during the ramp down of the bake cycle. The bakeout of the whole cell will be completed in ~3 days, from Day 1 to Day 3, and can be comfortably fitted in a normal work week while still leaving sufficient time for any necessary remedial actions. The vacuum cell will be leak-checked again after the bake, using the cell RGA. The fixed support points on the chambers will be checked and adjusted to their original positions by the survey group to ensure that all the critical components are properly aligned.

7.3.5   Storage Ring Vacuum Pumping

The types and sizes of the pumps to be used at NSLS-II will be standardized throughout all the machine areas as much as possible, to lower the unit cost and to ease routine maintenance in the future. The selection of the pumps will be based on the experience of the existing pumps used in NSLS and other similar SR facilities.

7.3.5.1   Roughing Pumps

A set of TMPs backed by dry mechanical pumps will be used to rough down the vacuum section from ambient pressure to high vacuum, and during in-situ bake before turning on the in-line ultra high vacuum pumps. The TMPs will be connected to the vacuum sections through small, manually operated, all-metal angle valves. TMPs with magnetic or ceramic bearings of ~100 l/s size backed by dry pumps of ~5 l/s are deemed sufficient, since the ultimate pumping speed at the vacuum chambers is limited by the conductance of the chambers, the angle valve, and the flexible hose. TMPs will be manually valved out once the sector reaches ultra high vacuum. Each of the TMP stations will be equipped with vacuum gauges and electro-pneumatic valves to quickly and effectively isolate the TMP from the vacuum section in the event of pump or power failure. A dozen TMPs will be needed during the first phase of NSLS-II construction for component testing and leak checking. These TMPs, due to limited operating lifetime under heavy usage, will be replaced with newer models to meet required ring and beamline vacuum during NSLS-II commissioning and operation. A list of TMPs required for the operations at the storage ring is given in Table 7.3.3.

Table 7.3.3   List of Vacuum Pumps and Gate Valves for the Storage Ring and Font Ends.

	IP 400 l/s	TSP 500 l/s	NEG Lumped 500 l/s	NEG strips*~100 l/s/m	TMP portable	Gate valves
SR	150	150	60	150	10	60
Front end	60	60	0	0	4	30
ID	60	60	60	27	4	
Total	270	270	120	177	18	90

*Each chamber will have a pair of 3–5 m NEG strips for a total length over 1 km.

7.3.5.2   Ultra High Vacuum Pumps

After initial rough down and in-situ bakeout of the vacuum sectors, the system pumping will be transferred from TMPs to ultra high vacuum pumps, including SIPs, TSPs, NEG cartridges, and NEG strips. TSPs and NEGs have high pumping speed for active gases such as CO, CO_2, H_2O, and H_2 with equilibrium pressure down to 10^{-12} Torr; they, however, will not pump inert gases (CH_4, C_2H_6, etc.) nor noble gases (He, Ne, Ar, …). Sputter ion pumps will remove inert and noble gases as well as active gases.

Triode-type SIPs have better pumping speed for noble gases, but they tend to have higher current leakage and are harder to rebuild after electrode saturation. A few noble diode SIPs, with tantalum cathode plates and similar pumping speed as triode pumps for noble gases, will be used to supplement the regular diode-type SIPs, thus avoiding so called "argon instability." Ion pumps of 30 l/s, 200 l/s, and 400 l/s will be used throughout NSLS-II, with the 30 l/s pumps used at conductance-limited areas such as booster synchrotron and beam transport lines; and the larger pumps at SR absorber and shutter locations. These SIPs will have large anode cells to retain sufficient pumping speeds down to the 10^{-10} Torr range. A DESY-style high-voltage feedthrough, which is less prone to radiation-induced corrosion at the brazing joint, will be used for the ion pumps. Commercial dual ion pump controllers with local and remote capabilities will power and monitor the SIP, by interfacing with the PLC and control computers, through hard wires and Ethernet linkage, respectively. Ion pump currents will supplement the vacuum gauges to provide pressure distribution over the whole ring. However, due to the buildup of leakage current in the ion pump elements, the reliable pressure reading from ion pumps is limited to the mid 10^{-10} Torr range. A list of ion pumps for the storage ring is given in Table 7.3.3.

The large volume of active gases desorbed from the photon absorbers can be efficiently removed from the SR by localized TSPs of ~500 l/s, thus minimizing the quantity of gases diffused back to the electron beam channel. Alternatively, at absorbers for damping wigglers, with a modest increase in cost TSPs may be replaced with NEG cartridges of comparable pumping speed but higher capacity between the reactivations. Both TSPs and NEGs can be activated and reactivated locally or remotely. However, TSPs have the advantage of only generating a brief gas burst during their short sublimation period, while NEG activation

takes longer, during which time a larger amount of hydrogen is produced and must be removed by the portable TMP stations.

Distributed NEG pumping in the form of NEG strips, similar to those employed at the APS storage ring, is planned for use in all cell vacuum chambers. This is deemed efficient to provide linear pumping to the beam channel through the photon exit opening. Dual strips will be mounted on the top and bottom of the antechamber. There will be sufficient clearance between the two mounted NEG strips to allow the passage of photons, even when a beam mis-steers. The mounting of the dual strips will be carefully designed and thoroughly tested to eliminate any potential electrical faults during in-situ bake and NEG activation. The NEG activation is at $400^{o}C$ for 30 minutes and will be achieved with resistive heating of the NEG strips with ~45 ampere current, carried out at the end of in-situ bakeout or during the machine maintenance period. The two NEG strips together will provide more than 240 l/s per meter pumping speed for active gases such as CO and H_2 even after pumping ~0.1 Torr-l per meter of active gases, corresponding to a few months of beam operation at 10^{-9} Torr pressure.

Some of the ID vacuum chambers will have very small gaps, resulting in limited linear conductance. In these cases it is not effective to simply rely on the lumped pumps located at both ends of the chamber. Sputter-coated NEG thin film has been applied to the inner surface of ID chambers at several SR facilities, notably at ESRF, where 20 ID chambers have been coated and in operation for 5 years, and at Soleil, where most straight chambers have been NEG coated. For narrow-gap undulators at NSLS-II, NEG coating will be considered during the design stage; if appropriate, it will greatly simplify the pumping system design. For long straight sections that are not occupied by insertion devices, distributed NEG strips together with large ion pumps and titanium pumps will be installed to maintain ultra high vacuum.

7.3.6   Vacuum Measurement and Control

7.3.6.1   Monitoring and Control Methodology

The vacuum level in the storage ring, the front ends, and the beamlines will be monitored and interlocked with the ion pump current and with vacuum gauge readings. Residual gas analyzers will also be used for online monitoring and diagnosis. Each vacuum sector will have a convection-enhanced Pirani gauge and two ionization gauges as the primary vacuum gauges. Additional vacuum gauges will be installed to protect the RF cavities and kickers. Vacuum devices such as gauge controllers, ion pump controllers, gate valve solenoids, and valve position indicators—with local and remote capabilities—can be operated through front-panel switches. Their communication with the equipment control system will be through RS232 or Ethernet links for remote monitoring and control. It is anticipated that most of the vacuum controllers will be off-the-shelf items purchased through competitive bids from qualified vendors.

Due to the predicted high level of radiation in the SR tunnel, controllers for vacuum systems will be placed in satellite electrical racks located outside the storage ring shielding structure. Electrical power for vacuum diagnostics and controllers will be standard 115 V AC and 60 Hz. Since vacuum pumps and associated vacuum equipment surrounding the ring vacuum chambers are subjected to synchrotron and bremsstrahlung radiation, radiation-resistant cables and appropriate routing for wire extensions will be employed to minimize radiation damage.

7.3.6.2   Vacuum Gauges

One primary vacuum gauge, a convection-enhanced Pirani gauge, will be installed in each vacuum sector to provide pressure readings ranging from atmospheric pressure down to 10^{-4} Torr. It will also be used for other vacuum equipment protection and interlocking. Two ion gauges, either Bayard-Alpert ion gauges or inverted-magnetron cold cathode ion gauges, will be installed at each SR vacuum section as the primary UHV gauge. The same type of ion gauge will be used for injectors, beam transport lines, front ends, and user

beamlines. Both types of ion gauges have a useable pressure-sensing range down to 10^{-11} Torr and they have been implemented successfully at various synchrotron radiation facilities. CCGs have the advantage of overlapping the lower end of the Pirani gauge range and can be operated through long cables for signal transfer, thus eliminating the necessity of locating electronics nearby. CCG tubes do not have built-in hot filaments and are therefore less susceptible to mishandling and filament breakage during startup and commissioning. The accuracy of CCG readings is normally at ±50%. Moreover, it is difficult to de-gas CCGs once they are contaminated. CCGs are still our choice at this point in the design process. The numbers of vacuum gauges in each area of the storage ring are listed in Table 7.3.4.

Table 7.3.4 Number of Gauges and Residual Gas Analyzers in Various Areas of the Storage Ring.

	TCG*	Ionizing Gauge	Residual Gas Analyzer
SR	30	60	34
Front end	30	60	60
ID	30	60	10
Total	**90**	**180**	**104**

*TCG = convection-enhanced Pirani gauge

Interference with the gauge readings due to the presence of copious electrons, photons, and photoelectrons has been observed at many SR facilities. Therefore, if practically achievable, the gauge tubes will be mounted on elbows at shielded ports on the vacuum chambers to minimize interference and erroneous pressure readings. The gauge tubes will also be installed in areas with minimal stray electrical and magnetic fields. Radiation-hardened material such as Kapton-insulated cables will bridge the short distance between the chamber gauge ports and the cable tray to ensure system reliability. Kapton cables are bakeable up to 200°C. Microprocessor-based multi-gauge controllers will be used to control the vacuum gauges and to provide system monitoring and control through RS232 or an Ethernet bus. The controller will be hardwired to interlocks through PLCs to gate valves and other beam components and subsystems.

7.3.6.3   Residual Gas Analyzers

Quadrupole-type RGAs will be installed to measure the partial pressures of residual gas species at selected locations in the injectors, storage ring, front ends, and user beamlines. Their use will help to identify sources of residual gases, including photon-desorbed gas from chamber walls and absorbers, air leaks, cooling water leaks, oil back-streaming, specialty gases back-streamed from the beamlines, and other contaminants. RGAs with electron multiplier will have partial pressure sensitivity down to the 10^{-13} Torr range. Due to the high cost, RGAs may only be installed at some vacuum sections during the initial phase of NSLS-II operation. The RGAs' quadrupole mass filter RF box, which contains sensitive electronics, may be located near the head and needs to be shielded from synchrotron radiation. The PC-based control units for RGAs, however, will be located at the satellite control racks, to allow easy access for online analysis and maintenance. The number of RGAs estimated for the storage ring and front ends is listed in Table 7.3.4.

7.3.6.4   Vacuum Control and Equipment Protection Systems

The vacuum control system has to 1) monitor and control all the vacuum equipment including gauges, pumps, valves, etc., to ensure that they are operating properly in their appropriate ranges; 2) collect and archive the data for instant display and alarm and for off-line analysis; and 3), most importantly, interlock and protect the storage ring and injector from harm before damage can develop.

The vacuum control system will interface directly with each vacuum device, and as part of the storage ring equipment control and protection systems (EPS). Due to high radiation levels in the storage ring tunnel, all the vacuum devices and the vacuum control system will be located at the satellite control racks. They will be backed by uninterruptible power supplies. Vacuum devices include gauge controllers, ion pump

controllers, chamber and absorber temperature readouts, cooling water flow sensors, and gate valve solenoids. They can be operated via front-panel switches and with the machine control system through RS232 or Ethernet links for high-level monitoring and control. The low-level vacuum controls, consisting of several dedicated PLCs with digital and analog I/O modules, take inputs from the vacuum devices and send out commands through dry contact circuits. The PLCs, with their own microprocessors and operating systems, will be programmed by vacuum system experts and provide the logic for the operation and control of the vacuum devices.

For gate valve control, the PLCs will use a voting scheme, with inputs from the setpoint contacts of several gauges and pumps, to initiate valve interlock and closure, therefore minimizing false triggering due to the malfunctioning of a single gauge or pump. The PLC for the water flow and temperature monitoring system, with direct inputs from thermocouples and flow meters, will read and compare those with the pre-set values. An out-of-range alarm from this PLC will trigger an output to the EPS to abort the beam, thus preventing overheating of the chamber wall or absorbers, due to either the malfunction of the cooling water system or abnormal beam steering. The PLC outputs for the flow meters, the temperature readouts, and gate valve status will be part of input arrays to the EPS, which will be used to determine if conditions are unacceptable. When warranted, the EPS will initiate a fast beam abort by interrupting the low-level RF power to the accelerating cavities. The stored beam would coast inward to a scraper and be lost in a fraction of millisecond.

References

[7.3.1]   J. Noonan, J. Gagliano, G.A. Goeppner, R.A. Rosenberg, and D.R. Walters, "APS Storage Ring Vacuum System Performance," Proc. PAC97, p 3552-5 (1998).

[7.3.2]   C. Doose, L. Emery, and S.H. Kim, "Investigation of the Surface Resistivity Tolerance of the Kicker Ceramic Vacuum Chamber at APS," Proc. PAC01, p1491-3 (2001).

[7.3.3]   J. Jones, S. Sharma, and D. Bromberek, "APS SR Flexible Bellows Shield Performance," Proc. PAC99, p 3095-7 (2000).

[7.3.4]   C.L. Foerster, C. Lanni, and K. Kanazawa, "Measurements of photon stimulated desorption from thick and thin oxide of KEKB collider copper beam chambers and a stainless steel beam chamber," *J. Vac. Sci. Technol. A* **19**, 1652 (2001).

[7.3.5]   C.L. Foerster, C. Lanni, J. Noonan, and R.A. Rosenberg, "Photon stimulated desorption measurements of an extruded aluminum beam chamber for the Advanced Photon Source," *J. Vac Sci. Technol.* A14, 1273 (1996).

[7.3.6]   V. Anashin, et al., "Photodesorption and Power Testing of the SR Crotch-Absorber for BESSY-II," Proc. EPAC98, p. 2163 (1999).

[7.3.7]   R. Kersevan, "MOLFLOW User's Guide," Sincrotrone, Trieste Technical Report, ST/M-91/17 (1991).

[7.3.8]   M.K. Sullivan, "A Method for Calculating Pressure Profiles in Vacuum Pipes," PEP II AP Note No. 6-94, March 1994. (Vaccalc is a software using the finite differential method for pressure calculation.)

7.4   Beamline Front Ends

7.4.1   Scope

The beamline front ends connect the storage ring to the user beamlines and provide radiation protection to personnel. Most of the front-end components generally reside within the storage ring's shield wall, outboard of the dipole vacuum chamber. The major components of the beamline front-ends are photon masks, shutters, heat absorbers (such as beam-defining apertures and/or slits), fast valves (or other shock wave protection devices), vacuum isolation valves, beryllium windows, or other means of pressure isolation sensors, and diagnostics. Vacuum chambers are also included; however, the chambers are often part of the individual front-end components. Other components, such as filters, may be included depending on the application. The front end usually starts at the exit to the dipole vacuum chamber and usually extends to the beryllium window (if used), where the user vacuum is isolated from the machine vacuum. If a beryllium window is used, it generally is positioned as close as is practical to the outer end of the storage ring shield wall. Also to be considered as important front-end components are radiation shields, i.e., safety shutter shields and bremsstrahlung shields. Vacuum pumps, vacuum sensors, and diagnostics (e.g., for Residual Gas Analysis, to activate fast valves, etc.), heater tape and provisions for bakeout, as well as the vacuum valves are included in the front ends—even though these components are generally considered part of the vacuum system. Steel stands will be designed, as needed, to support the front-end components at the nominal 1 m beam height.

The details of the front-end components will differ based on the radiation source. The front ends may transport x-rays from a bending magnet or from an insertion device. The resulting photons may be collected and directed down a beamline, or absorbed as heat. For the bending magnet beamlines, the front-end designs can differ according to the angle (in mrad) of radiation and number of apertures (and therefore beamlines) in each heat absorber that allows synchrotron radiation to pass through. For insertion device front ends, the type of insertion device used (e.g., undulator or wiggler), and its magnetic properties (field strength, length of field, periodicity, etc.) determine the radiation output parameters (e.g., radiation fan, output power density, and total radiated power). The heat-absorbing-components in each front end therefore need to be set according to the radiation source parameters. These parameters are selected according to the research needs of the scientific program served by each beamline. The front-end components and the arrangement of components therefore will differ somewhat according to the specific front end.

The vacuum aspects of the front ends include the gas loading (including outgassing loads from the heat absorbers) and pumping characteristics. The front-end vacuum system must maintain and measure acceptable vacuum pressures within the vacuum chambers in the front end and must be compatible with the storage ring vacuum. Vacuum isolation valves are included to allow the removal and replacement of front-end components. Since there is no vacuum isolation during operations between the front ends and the storage ring, the front ends share machine vacuum from the exit of the storage ring chamber to the beryllium window (or other vacuum isolation provision). The vacuum system may differ slightly between beamline magnets and front ends. The vacuum system components must function in conjunction with the front-end components, however. Therefore, some front-end vacuum system aspects are included in this section as they relate to the front end components.

Vacuum isolation provisions between the front end and the downstream beamline are necessary. For hard x-ray beamlines, this usually takes the form of a beryllium or a CVD diamond window, which is under consideration for NSLS-II. However, for beamlines such as VUV and soft x-ray beamlines, as well as the hard x-ray beamlines that cannot tolerate the presence of a window (due to its potential to introduce optical artifacts into the transmitted beam), "vacuum isolation" must be implemented without a solid window separating the front end and beamline vacuum spaces. A differential pumping stage can address this requirement. A commercially available device, which could permit a downstream beamline to operate at a

pressure as high as 10^{-4} Torr while still preserving a pressure of 10^{-9} Torr in the front end, is used on several beamlines at APS for this purpose. This device consists of an inline ion pump with internal throttles to limit conductance, yet it offers a sizable clear aperture for the beam.

Note that the inclusion of such a device between the front end and the beamline does not obviate the need for sensitive pressure diagnostics along the beamline, as well as protective measures such as fast-closing valves in case of accidental vacuum breaks along the beamline.

7.4.2 Mechanical Design

Six front-end configurations are currently anticipated, based on radiation source type and concomitant characteristics of output, geometry, and power loading. The six sources are 1) superconducting wigglers, 2) cryogenic permanent magnet undulators, 3) superconducting undulators, 4) damping wigglers, 5) normal conducting and permanent magnet insertion devices, including soft x-ray undulators and elliptically polarized wigglers, and 6) bending magnet beamlines. Figure 7.4.1 shows a conceptual layout of the mechanical design for a typical hard/soft x-ray beamline front end.

The storage ring lattice constrains the length available for insertion devices. Fifteen 5 m straight sections and twelve 8 m straight sections are available for insertion devices. The design parameters for the various radiation sources currently expected at NSLS-II are given in Chapter 8.
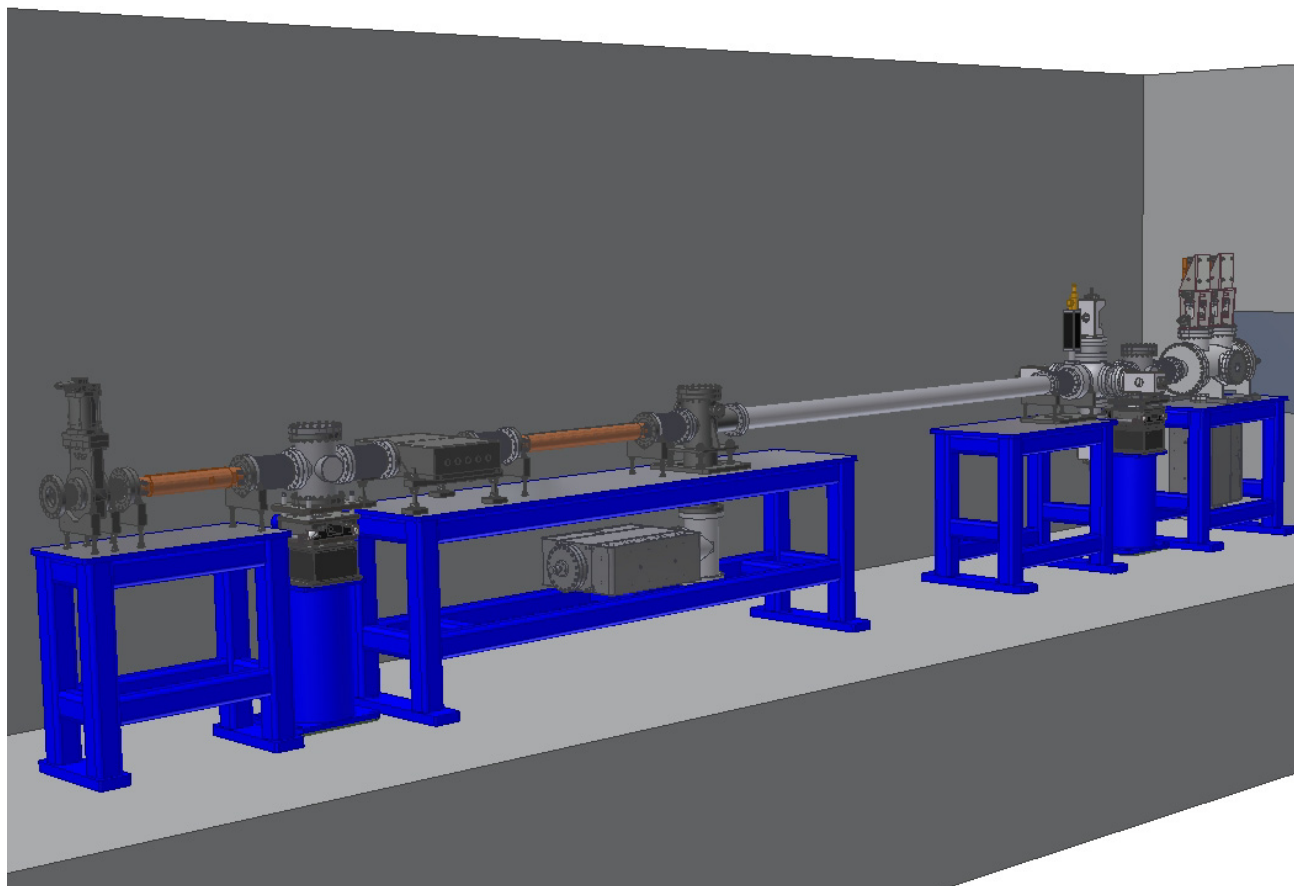

Figure 7.4.1 Typical layout of a hard or soft x-ray beamline front end. From left to right: UHV gate valve, fixed aperture photon mask, first, photon beam position monitor (BPM1), collimator, photon shutter, four-way cross for ion pump, spool, fast valve, beam defining aperture, second photon beam position monitor (BPM2), and safety shutter.

7.4.3   Vacuum Components/Enclosures

The front end will consist of numerous ultra high vacuum chambers that house heat absorbers, beam diagnostics, and personnel protection devices, along with beam chambers to transport the photon beam from the electron storage ring to the experimental beamlines. These chambers and ducts will be constructed from 304L stainless steel tubes and weldments, where applicable, and will be joined to adjacent components using commercially available Conflat flanges, copper gaskets, and UHV hardware. Fabrication of chambers and ducts will be from stainless steel utilizing TIG-welded construction.

Because the front ends share the storage ring vacuum, front-end and SR vacuum pressures must be compatible. A pressure of 10^{-9} Torr therefore must be maintained in the beamline front ends during machine operations. To achieve these pressures, a combination of UHV components and procedures, in addition to bakeout of the front-end subsystem, will be employed. The chambers and beam ducts will be designed to withstand a bakeout temperature of 200°C, to accelerate the release of gases. We expect that an integral bakeout system will be incorporated in the beamline front end, to enable the capability of in-situ bakeout. Commercially procured equipment to accomplish this task within the stated parameters will be selected.

Each front end will employ a commercially available UHV all-metal gate valve. This valve will be used to separate the front-end from the SR vacuum for bakeout, maintenance, and during installation of the front end. Additionally, this valve will be used in combination with a commercially procured UHV fast-closing valve to protect the SR vacuum in the event of a vacuum breach from the beamline. The fast valve should close in less than 15 msec and have a leak rate of less than 7.5×10^{-10} Torr-l/s when closed. We plan to use this isolation valve in combination with a water-cooled bending magnet photon shutter [see Figure 7.4.2(c)] to accept the synchrotron radiation at the exit ports where no front end is installed.

Referring to Figures 7.4.2a and 7.4.2b, two ion pump/titanium sublimation pump combinations are planned, located strategically in each beamline front end. In order to minimize any residual gas species generated by the photon beam impinging on a surface, a 400 l/s ion pump/TSP pair will be installed near the photon shutter locations. An additional 400 l/s ion pump/TSP pair will be installed at the safety shutter due to the relatively long distance (approximately 5 m) between the photon shutter and the safety shutter—a section of the beamline front end that would otherwise have no dedicated vacuum pumping.

The front end configuration shown in Figure 7.4.2a reflects our current thinking of what is required to serve a beamline supporting a hard x-ray nanoprobe instrument. It includes a combination of a fixed mask and moveable slits to define the beam size as close to the undulator as possible. This is not likely to be necessary for most beamlines, and so they will only have a beam defining aperture, as shown in Figure 7.4.2b. This is an example of some of the differences that may be required in the design of front ends to optimally serve each beamline.

The front ends for beamline ports that have not yet been allocated will be configured with a photon shutter, gate valve, and bremsstrahlung beam stop, as shown in Figure 7.4.2.c. Once a beamline port is allocated, the front ends will be configured to meet the specific requirements of the beamline it will serve. Since those requirements may vary for different beamlines, the detailed design and construction of front ends will occur as part of the design and construction process for each beamline.

An all-metal right-angle valve will be located between the photon shutter and the fast-closing valve. Attached to this valve will be a fitting with both an ion gauge and an RGA to monitor the total and partial pressures of the front-end vacuum. At the remaining port of the cross, a valve will be installed (to be used in combination with the right-angle valve) to allow for venting and pump-down when replacing either the ion or RGA gauge filaments. Additionally, installation of a vacuum valve between the fast-closing valve and the second BPM is planned to allow for separate venting/pump-down of the downstream portion of the front end.

To allow for transverse offsets in front-end hardware, thermal expansion and/or contraction, and to allow for sufficient flexibility in the alignment of front-end devices, an appropriate number of welded bellows assemblies will be part of the front-end vacuum system.
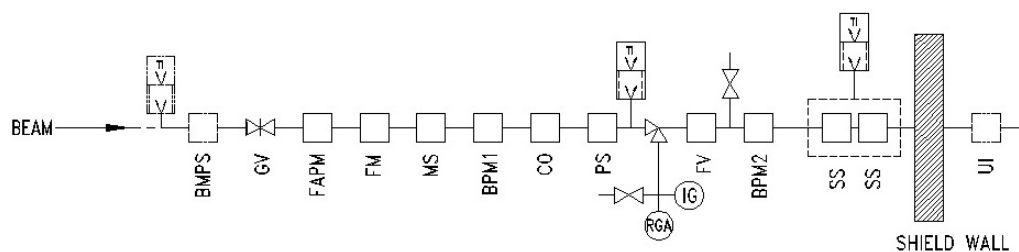
BMPS:BENDING MAGNET PHOTON SHUTTER, BPM:PHOTON BEAM POSITION
MONITOR, CO:COLLIMATOR, FAPM:FIXED APERTURE PHOTON MASK,
FM:FIXED MASK, FV:FAST VALVE, GV:UHV GATE VALVE, MS:MOVABLE
SLITS, PS:PHOTON SHUTTER, SS:SAFETY SHUTTER, UI:USER ISOLATION

(a) HARD X-RAY NanoProbe FRONT END
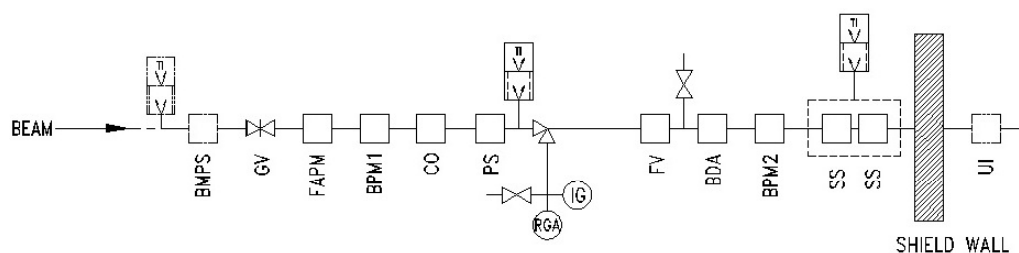
BMPS:BENDING MAGNET PHOTON SHUTTER, BDA:PHOTON BEAM DEFINING
APERTURE, BPM:PHOTON BEAM POSITION MONITOR, CO:COLLIMATOR,
FAPM:FIXED APERTURE PHOTON MASK, FV:FAST VALVE, GV:UHV GATE
VALVE, PS:PHOTON SHUTTER, SS:SAFETY SHUTTER, UI:USER ISOLATION

(b) TYPICAL HARD/SOFT X-RAY ID FRONT END

BMPS:BENDING MAGNET PHOTON SHUTTER, BS:BREMSSTRAHLUNG BEAM
STOP, GV:UHV GATE VALVE

(c) TYPICAL CONFIGURATION FOR NO INITIAL FRONT END

Figure 7.4.2   Front-end schematic representation of: **a)** the Hard X-Ray NanoProbe front end, **b)** typical Hard/Soft X-Ray insertion device front ends, and **c)** exit ports with no initial beamlines.

7.4.3.1   Heat Absorbers

Heat absorbers are front-end devices consisting of components whose function is to absorb the synchrotron radiation produced by the SR bending magnets or IDs. These absorbers are needed to: 1) stop dipole radiation in the exit ports that have no front ends, 2) prevent uncooled surfaces in the front ends from being impacted by a mis-steered beam, 3) protect the uncooled safety shutter shielding blocks, and 4) completely prevent the photon beam from being transported beyond the front end. The heat-absorbing devices needed to accomplish these tasks are a bending magnet photon shutter, a fixed aperture photon mask, and a photon shutter.

Heat-absorbing front-end components are designed based on the horizontal and vertical angular divergence and the power density distribution of radiation produced by each insertion device, as well as on temperature criteria. As an example (referring to Chapter 8), for the CPMU device at a distance of 15 m from the source, the peak heat flux of the insertion device radiation is approximately 11.6 W/mm^2, with a total power of 11.1 kW at 3.0 GeV and 500 mA. We assume that an electronic active-interlock system will be used to reasonably limit the electron beam orbit so that the photon beam cannot illuminate any uncooled surfaces of the storage ring vacuum chamber. For thermal calculation purposes, we assume that there is a ±2 mm offset to accommodate beam deviations in position and minor manufacturing and alignment errors. The electron beam may also have an angular steering error of ±1 mrad.

Since the storage ring isolation valves are uncooled, dedicated heat absorbing devices capable of protecting the valves from the incident dipole magnet radiation are required. A bending magnet photon shutter will be installed upstream of the UHV isolation gate valve, which is the first vacuum component in the front end (see Figure 7.4.2a). Due to the rather low power density produced by the dipole magnet radiation, a normal incidence, water-cooled device will be sufficient. For heat-absorbing devices that experience relatively low peak temperatures (less than 200˚C), OFHC copper will be the material of choice for all heat absorbing surfaces. We anticipate that the BMPS, which is not a high heat flux device, will meet this criterion and that it will be possible to procure and install a commercially available version.

The **f**ixed-**a**perture **p**hoton **m**ask is the first front-end component that may be impacted by the photon beam. The FAPM protects front-end components that are not designed to withstand the thermal loading of the photon beam, in the case of beam mis-steering. For this reason, the photon mask must close when the front-end vacuum valves close. For commonality, the initial overall engineering design approach for the FAPM and the photon shutter will be similar. The heat absorbing surfaces of the FAPM will be designed from a single solid piece of Glidcop to handle the high heat flux of the insertion devices. To accommodate the dissipation of the full insertion device power, the aperture of the FAPM will be tapered on all four sides. The mask will be designed such that when the final geometry is fixed, the converging aperture will taper to 7.5 mm (V)×30 mm (H) at the downstream end of the device. Integrally machined cooling passages on all four sides will provide pathways for the flow of coolant. Since the FAPMs will be designed to withstand vacuum forces, a separate vacuum chamber will be unnecessary. Also, since the FAPMs will be infrequently subjected to the full ID power, a higher peak temperature will be allowed than for similar masks that are cyclically loaded.

Recent experimental results at both APS and ESRF have concluded that for Glidcop devices, a maximum calculated temperature of 500˚C is sustainable for 10,000 thermal cycles [7.4.1]; therefore, this will be our thermal design criteria for high heat flux devices which are not cyclically loaded. From preliminary photon shutter thermal calculations, a 4° (70 mrad) angle of incidence to the nominal should provide adequate thermal loading reduction for the FAPM heat-absorbing surfaces. Careful calculations and detailed study will be carried out in the preliminary design phase to ensure that the devices are optimized for the high heat loads encountered.

The photon shutter is a device that can be opened to allow photons to be directed down each beamline. One method to accomplish this would be to tilt a photon shutter similar in design and construction to the FAPM so that one of the inclined, heat-absorbing surfaces completely intercepts the photon beam when the photon shutter is in the closed position. To minimize design and fabrication costs, all heat-absorbing surfaces of the photon shutter will be designed and fabricated from Glidcop, similar to the FAPM. As with the FAPM, integrally machined cooling passages will provide coolant flow to remove the thermal load. Figure 7.4.3 illustrates a conceptual design for the photon shutter (*PS* in the figure). In addition to the cooling passages on the horizontal heat absorbing surfaces (as shown in the figure), the photon shutter would have an additional set of machined cooling passages adjacent to each vertical heat-absorbing surface. During the design phase, the requirements for each photon shutter will be considered carefully for each application. A photon shutter design that can accommodate most or all front-end applications will be considered, to minimize engineering and design labor, to keep manufacturing costs low, and to maintain commonality of components wherever possible.
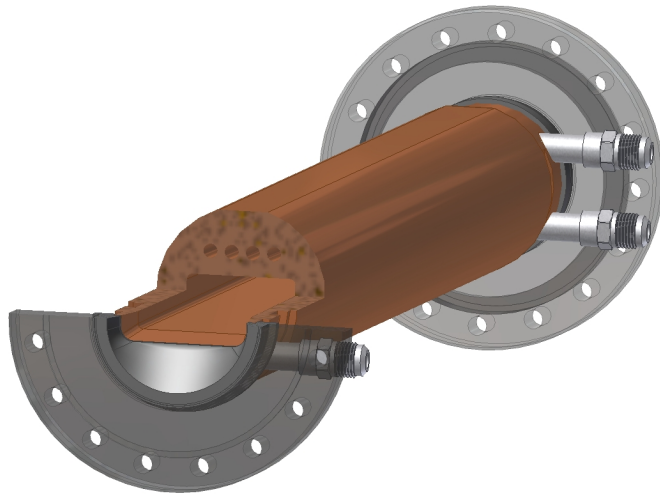
Figure 7.4.3   Conceptual design of the NSLS-II photon shutter.

Preliminary calculations indicate that an angle of incidence of 4˚ between the nominal photon beam centerline and the inclined surface of the photon shutter aperture will allow us to maintain the design specification for Glidcop of $T_{max} \leq 450˚C$. Figure 7.4.4 shows the results of a steady-state, 2D finite element computation for the CPMU device listed in Table 7.4.1, at 3.0 GeV and 500 mA and a distance of 17 m from the source. That figure shows the thermal gradient that results from completely intercepting the ID radiation with the heat absorber directly in the photon beam path. This simulation was computed using a heat transfer coefficient of ~1.6 W/cm^2/°C for each cooling channel. The final optimized design of the photon shutter must recognize that the 4˚ inclined surface incorporated in the simulations includes both the angle the device is rotated through to close off the photon beam, as well as the angle of inclination of the heat-absorbing surface.
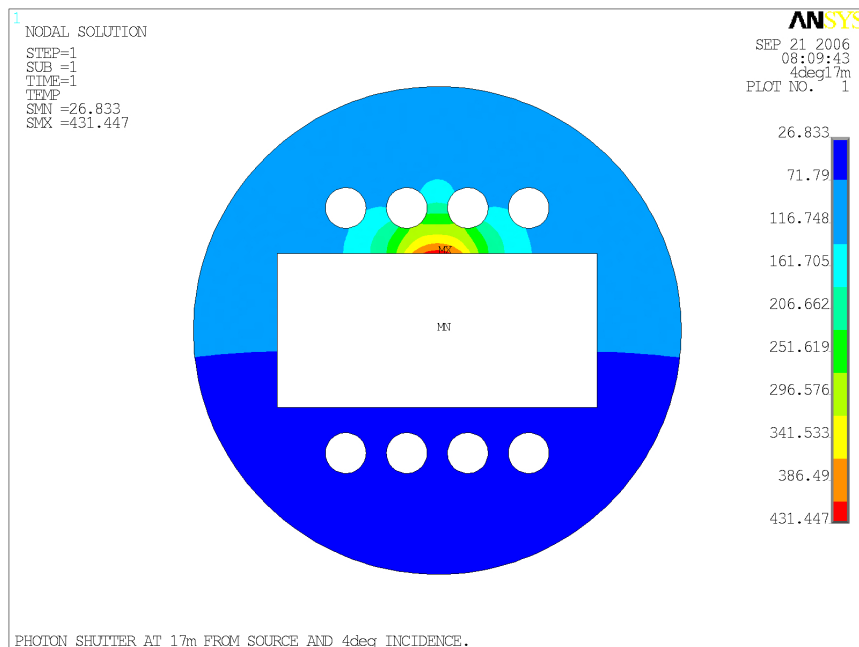

Figure 7.4.4   Steady-state temperature distribution from 2D finite element analysis simulation of the photon shutter. Temperature units are degrees Centigrade.

Additional specific requirements for beamline front ends that require specialized collimating or beam-defining apertures downstream of the FAPM will not be specified until those beamlines are designed. We nevertheless expect, however, that one additional photon-collimating aperture will be needed in most front ends. Therefore, a generic BDA will be included as a placeholder in these front ends until specific requirements are developed. Any additional photon collimating devices will be located in the individual beamlines outside of the x-ray ring's outer shield wall.

7.4.3.1.1   Hard X-Ray Nanoprobe Beamline Masking Requirements

The Hard X-ray Nanoprobe Beamline has unique requirements. Two additional BDAs (listed as moveable and fixed masks in Figures 7.4.2a and 7.4.5) are currently planned for this beamline front end. The first BDA downstream of the FAPM in the Nanoprobe Beamline front end (in Figure 7.4.5, listed as "1st fixed mask") will be located as close to the undulator source as possible. This BDA is fixed in space and serves as a guard, reducing the size of the initial undulator x-ray beam to the desired maximum beam size accepted by the beamline. The second absorber (listed as "2nd moveable mask" in Figure 7.4.5) is not fixed. It can be moved into the beam for a high-spatial-resolution mode and removed for high-flux mode. When in the beam, it provides a beam-defining horizontal constriction equal to the vertical FWHM extension of the beam. When removed, it passes the full beam unobstructed. These two additional absorbers are shown without the other front-end components in Figure 7.4.2. For an x-ray wave length of 1 Å (~12.4 keV), the following values were used to help estimate the absorber geometric requirements.

$$
\begin{array}{rcl}
\text{horizontal source size, } \sigma_x & \blacksquare & 84.5 \ \mu\text{m} \\
\text{vertical source size, } \sigma_y & \blacksquare & 4.3 \ \mu\text{m} \\
\text{horizontal source divergence, } \sigma'_x & \blacksquare & 18.2 \ \mu\text{rad} \\
\text{vertical source divergence, } \sigma'_y & \blacksquare & 1.8 \ \mu\text{rad} \\
\text{length of undulator, } L & \blacksquare & 5 \ \text{m}
\end{array}
$$

In this application, placement of the first absorber at 14 m or less and the second absorber at 15 m or less from the undulator is desired for best optical properties of the photon beam. The aperture openings for the first absorber are calculated to be X1 ≈ 1400 μm and Y1 ≈ 300 μm. For the second absorber, the settings calculated are X2 ≈ 180 μm and Y2 ≈ 2 mm. The need for further vertical collimation at the second absorber in this beamline is currently not required; therefore, we will consider a design for this device similar to those in use at APS.
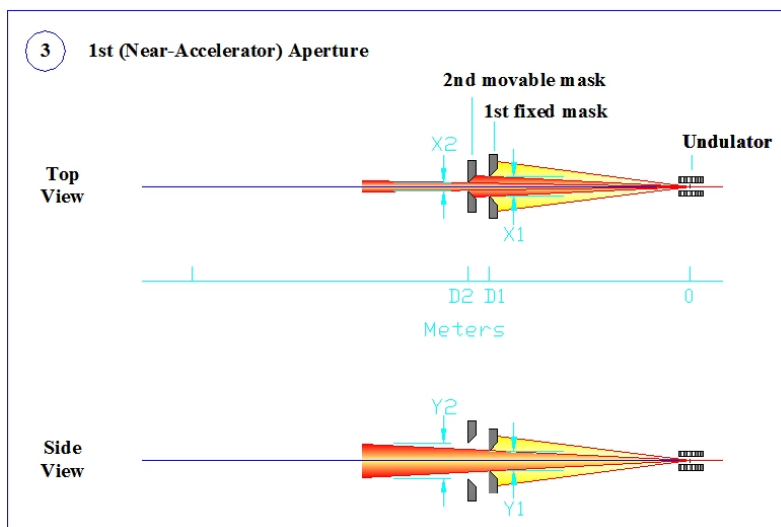

Figure 7.4.5   Absorber geometry for a nanoprobe beamline front end.

7.4.3.2   Radiation Protection

At times during storage ring operations, it will be necessary to access the experimental hutch (for example, to set up equipment and change samples). It will also be necessary to assemble and maintain the beamline apparatus when there is stored beam in the accelerator. To accomplish these tasks, a remotely actuated safety shutter will be required as one of the front-end components. For redundancy purposes, this component will consist of two identical tungsten shielding blocks housed in a single UHV-compatible vacuum chamber in each front end. The shielding blocks may be inserted into (or retracted from) the path of the bremsstrahlung radiation cone. There will be no need to provide active cooling for this device because the photon shutter, which is located upstream of this device, will completely absorb the synchrotron radiation.

The remotely actuated safety shutter device is a required part of a beamline personnel protection system, which should absorb the bremsstrahlung radiation, thus providing protection from ionizing radiation for personnel downstream of each shutter. From calculations, a thickness of 20 cm of tungsten is required to attenuate the bremsstrahlung radiation in the forward direction. Ray-tracing will be required to determine the transverse dimensions of the tungsten shielding. Additionally, lead collimators will be provided in each front end to confine the bremsstrahlung cone in the downstream experimental area. From calculations, a thickness of at least 30 cm of lead for the collimators will be required to attenuate the bremsstrahlung radiation in the forward direction. As with the tungsten shield of the safety shutter, ray-tracing will be performed to determine the minimum transverse dimensions of lead required. For exit port chambers that have no initial complement of front-end components, it will be necessary to install a bremsstrahlung beam stop as close as possible to the storage ring vacuum isolation valve (see Figure 7.4.2c).

A byproduct of the bremsstrahlung/lead collimator interaction is the production of neutrons that ultimately must be shielded. The concrete used in the shielding wall is a very effective neutron shielding material; however, there will be beampipe penetrations through the shield wall that must be considered. Void volumes between the shield wall and front-end beampipe penetrations will be filled with concrete and lead, to terminate the transit of photons and neutrons beyond the shield wall. For exit ports with no front end, the shield wall window will be completely filled with concrete.

7.4.3.3   Diagnostic Equipment

To correct for unwanted mechanically and electrically induced electron beam motions, two x-ray beam position monitors will be designed and installed in each front end as part of an orbit feedback system. These BPMs will detect photon beam position and supply information to an active feedback system that will correct the electron beam orbit. We anticipate that two gapped, blade-type BPMs will be installed to detect any closed-orbit instabilities. By utilizing two x-ray BPMs in each front end, it will possible to correct for both angular and displacement steering errors. To more accurately measure any angular steering error, it is most desirable to take advantage of the increased lever arm by placing the second x-ray BPM as far downstream as possible within the confines of the front end enclosure.

7.4.3.4   Interlocks

The two safety shutters and the photon shutter will provide a redundant means of absorbing the full synchrotron power and bremsstrahlung radiation in the beam. The Personnel Protection System will monitor the position of these devices to provide personnel at the beamline safety from prompt radiation. The Equipment Protection System will control the sequencing and control of front-end devices and prevent damage from occurring. The EPS will prevent damage to front-end components by sensing position, water flow, and vacuum, then taking action by operating components or dumping the beam, when appropriate.

To protect the storage ring vacuum from any inadvertent pressure rise due to front-end or beamline component failures, various interlock sequences will be implemented. Two possible scenarios in which an air-to-vacuum leak in the front end would corrupt the SR vacuum are mentioned here as examples: 1) a slow air-

to-vacuum leak due to faulty bellows or a leaking weld in a vacuum chamber, and 2) a catastrophic vacuum leak due to a failure in a beamline.

If monitoring of the vacuum quality (see Figure 7.4.2a) indicates a slowly increasing pressure, the origin of this pressure rise will be investigated and repaired during a regularly scheduled maintenance period. Should the pressure in the front end reach the ion gauge set point of approximately 5×10^{-7} Torr, the EPS will first signal the insertion device on the offending beamline to open its gap, thereby eliminating the high heat flux on any front-end components. The bending magnet photon shutter will then be actuated to provide dipole radiation protection to the uncooled isolation valve when it has been moved into the closed position. Finally, first the photon shutter and then the safety shutters will be the last devices instructed to close. With the storage ring isolation valve in the closed and sealed position and Personnel Protection System in place, ring operations will be allowed to continue unhindered by the vacuum leak in the front end. The front end or beamline experiencing such vacuum difficulties would be repaired during a regularly scheduled maintenance period. Note that all of these front-end actions will be taken in the background while facility operations continue unhindered.

In the case of a catastrophic leak, once the fast closing valve is triggered by a pressure exceeding 5×10^{-6} Torr in the front end or beamline, the EPS will send the appropriate signals to dump the stored electron beam. Triggering of the FV will simultaneously close the BMPS, isolation gate valve, and safety shutters. Operations may resume when proper sealing of the isolation gate valve has been verified and the vacuum leak in the front end or beamline has been isolated from the SR vacuum.

These two vacuum leak management strategies are the assumed baseline modes of operation in the event of an air-to-vacuum leak in the NSLS-II front ends. At present, we are aware of an ongoing evaluation at APS of a fast closing photon shutter that would be capable of handling the power densities generated by the planned NSLS-II insertion devices. This heat-absorbing device is, in principle, capable of closing in approximately 15 ms. One clear advantage of installing a device such as this in the beamline front end is that it would be possible to continue SR operations in the event of a catastrophic beamline vacuum leak rather than dumping the stored electron beam. The strategy to be employed in this scenario is as follows:

1. The EPS simultaneously signals the fast closing photon shutter to close and the fast valve to close.
2. The EPS then signals the offending insertion device to begin opening its gap.
3. Once the insertion device gap has been fully opened, reducing the insertion device heat flux to a level that the BMPS can safely manage, the BMPS receives a signal to close, to protect the storage ring isolation valve from incident dipole radiation.
4. The EPS then simultaneously signals the isolation valve to close and seal, and the safety shutters to close.
5. Once the SR isolation valve is sealed, the EPS disables the affected front end while the insertion device remains in the open position. The front end must be repaired during a regularly scheduled maintenance period.

As a preliminary estimation, we have determined that to reduce the heat flux developed by an ID to the same order of magnitude as the dipole magnet radiation, each insertion device will need to have its gap fully opened in the event of a catastrophic vacuum leak. A precondition of employing the vacuum leak strategy just described will require that all ID mechanics are designed to be sufficiently robust such that the gaps between magnet arrays can be fully opened in the least time practicable. Note that in this alternative scenario, we assume that the leak rate through the fast valve is small enough that the SR vacuum stays within acceptable limits until the isolation valve is completely closed and sealed. Thus, during the preliminary design phase, it will be important to determine the precise time required to open the ID gap to a state that will enable the BMPS to safely handle both the reduced ID power and the dipole magnet power.

7.5   Storage Ring RF Systems

The large dipole radius (25 m) and the medium energy (3 GeV) of NSLS-II results in very low radiated energy from the bending magnets (288 keV/turn). This increases the effectiveness of 8 damping wigglers to reduce the bare emittance of 2.1 nm-rad to 0.5 nm-rad. The RF system power requirement for NSLS-II is determined primarily by the power radiated by the damping wigglers. This makes it possible for us to stage the RF system installation to parallel the installation of damping wigglers and user insertion devices.

The small momentum compaction (0.0037), an RF frequency of 500 MHz and high RF voltage results in small bunch lengths of ~4 mm. This contributes to a short Touschek-dominated lifetime of <2 hours. To improve lifetime to greater than 3 hours, a third harmonic bunch lengthening cavity is included in the baseline design.

The storage ring RF system consists of the 500 MHz Superconducting RF cavities, their associated klystron tube amplifiers and power supplies, the passive SCRF third harmonic Landau (bunch lengthening) cavity, the liquid helium cryogenic plant, and the master clock, frequency synthesizers, digital I/Q cavity controllers, and RF distribution system that make up the low-level RF.

7.5.1   Physics Requirements and Design Parameters

The RF system must provide sufficient momentum acceptance (bucket height) so as not to be the limiting factor in the storage ring acceptance. In addition, with the small momentum compaction of the low emittance lattice leading to very short bunches, and the accompanying short lifetime, a third harmonic (1500 MHz) RF system is used to lengthen the bunches to increase the Touschek lifetime from <2 hours to >3 hours. The Landau cavity also increases the dependence of the synchrotron tune on the oscillation amplitude providing Landau damping, which can suppress bunch instabilities. The required RF power is the sum of the beam radiated power in the dipoles, damping wigglers, and user IDs. There is no unique approach to meeting the RF requirements; in fact, the frequency choice of 500 MHz is within a broad range of frequencies in which RF sources and cavity designs exist and that would meet the physics requirements. Three frequencies within this broad range, 352 MHz, 476 MHz, and 500 MHz, have been used successfully in third-generation light sources. The operating frequency of 500 MHz has been selected here due to the availability of existing SCRF cavity designs, commercial RF transmitters, and the large number of 500 MHz systems in use at light sources around the world. This translates into mature technologies and lower development costs. A summary of the ring parameters related to the design of the RF system is shown in Table 7.5.1.

Table 7.5.1   RF and Beam Parameters for the NSLS-II Storage Ring.

RF frequency [MHz]	499.46
Circumference [m]	780
Harmonic number	1300
Loss per turn (assuming 5 undulators, 21 m of DW, and dipole losses) [keV]	816
RF acceptance [%]	3
Accelerating voltage [MV]	3.3
Momentum compaction	3.7×10^{-4}
Bunch charge [nC]	1.2
Number of buckets filled with charge	1040

The radiation from dipoles and an assumed complement of five undulators and 21 m of damping wigglers result in an energy loss per turn of 816 keV, corresponding to 408 kW power loss at the design current of 500 mA. A 3% momentum acceptance ($\Delta p/p$) is specified to insure sufficient Touschek lifetime of the storage

ring. For 816 keV/turn energy loss this corresponds to an RF voltage of 3.3 MV (see Figure 7.5.1). As insertion devices and damping wigglers are added as the user program is built out, the loss per turn increases to more than 1.6 MeV, and a voltage of 4.8 MV is required to maintain the 3% bucket height.
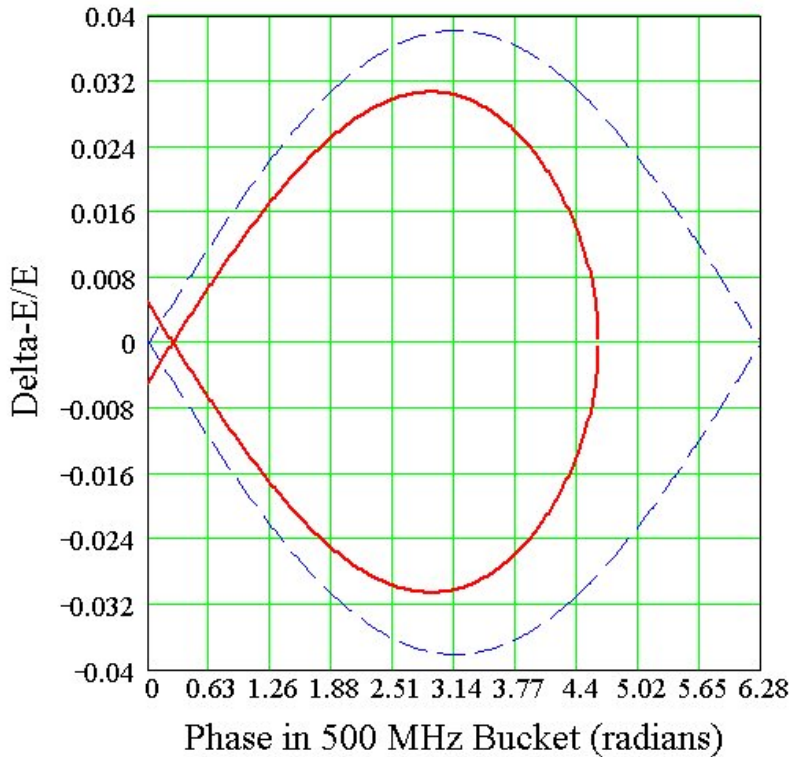

Figure 7.5.1   RF seperatrix for 3.3 MV RF field with (red trace) and without (blue trace) 816 keV/turn radiation losses. The 3% RF acceptance is easily met with two CESR-B cavities.

Thus, the evolution of the RF power requirements over the life of the facility must be taken into account. Table 7.5.2 outlines the initial machine configuration, the capabilities of the RF system, and a reasonable extrapolation as to how this might evolve as insertion devices are added. The exact scenario will be driven by the user requirements and is not fixed at this stage of the machine design.

Table 7.5.2   RF Power Requirements for Dipole Losses and Various Example Insertion Device Configurations.

RF power requirements	Phase 1: Capability of installed RF (270kW/cavity)		Phase 2: Adding 3rd cavity plus purchase 300-kW Transmitter		Phase 3: Add 4th RF station (cavity + transmitter)	
	#	P (kW)	#	P (kW)	#	P (kW)
Dipole	-	144	-	144	-	144
Damping wiggler (9.23 kW / m, 7 m each)	4	259	8	517	8	517
Cryo-PMU (4.17 kW/m, 3 m each)	6	76	6	76	10	127
EPU (4.1 kW/m, 4 m each)	4	66	4	66	5	83
Additional Insertion devices						209
Total		545		803		1080

The initial RF system will consist of two CESR-B cavities, each powered by a 310 kW transmitter. Three cavities will be purchased with the third cavity to be used as a spare in the event of a cavity failure. Two installed cavities can provide up to 5 MV, which exceeds the voltage requirement of 4.8 MV even for the full

complement of insertion devices and the 56 m of damping wigglers envisioned for NSLS-II. However, the power coupler is capable of delivering only ~270 kW of beam power, and so the ring is limited to four damping wigglers and 10 user IDs (or equivalent) by the initially available RF power. Installing a third cavity and transmitter will support a full complement of eight damping wigglers, resulting in the ultimate horizontal emittance of 0.5 nm-rad. Two 500 MHz cavities and one 1500 MHz harmonic cavity (to be described in Section 7.5.3) fit into a single 8 m straight. A second RF straight is reserved for the third and potentially fourth CESR-B cavity and second 1500 MHz cavity to meet the evolving power requirements of NSLS-II as more user IDs are added.

7.5.1.1   Impedance Analysis and Beam Stability

The high beam loading due to 500 mA average stored current requires highly damped structures to prevent beam instabilities. In this regard, the B-factory cavity designs of KEK, PEP-II, and Cornell are attractive and have been studied in detail.

The narrow band cavity impedances have been calculated using the codes GdfidL, SUPERFISH, and CLANS [7.5.1, 7.5.2, 7.5.3]. These codes calculate the longitudinal shunt impedance as

$$R_{sh} = \frac{\left[\text{Re} \left(\int E_z(z) e^{ikz/\beta} dz \right) \right]^2}{2P} ,$$

(7.5-1)

where P is the power dissipated in the cavity, E_z is the longitudinal electric field either on axis (monopole modes) or displaced with a radial offset corresponding to a dipole mode, quadrupole mode, etc. Here, k is the wave number (ω/c), and β is the ratio of beam velocity to that of light.

The cavities also have transverse impedances that can couple strongly to the beam. The transverse shunt impedance of a cavity is given by the integral of the force acting on the beam, as

$$Z^\perp = -i \left(\frac{\int_0^L (\vec{E} + \vec{v} \times \vec{B})_\perp ds}{\beta \cdot I_{av} \cdot a} \right) ,$$

(7.5-2)

where L is the cavity length, I_{av} is the average bunch current, and *a* the offset of the beam from the cavity axis. The beam must couple energy into the higher-order transverse mode through the electric field and hence there is a relation between the longitudinal and transverse impedances. The broadband impedance model uses the Panofsky-Wenzel relation,

$$Z_\perp = \frac{c}{\omega \Delta^2} \cdot Z_\parallel^{(\Delta)} ,$$

(7.5-3)

where Δ is the offset at which the longitudinal impedance is calculated. The cavity impedances have been calculated for the PEP-II, KEK-B, and CESR-B cavities [7.5.4, 7.5.5, 7.5.6]. All three cavity designs can meet the NSLS-II requirements in terms of attainable voltage and beam power delivered. The SCRF approaches of KEK and Cornell result in lower installed RF power requirements and more efficient operation, attain much lower HOM impedances, and require fewer cavities to achieve the voltage specification. This is particularly important when additional insertion devices are installed which will increase the RF voltage requirement to ~5 MV. The choice for NSLS-II has been narrowed to either the KEK-B cavity or the Cornell CESR-B cavity. Further studies on cost, reliability, and future upgrade potentials in the preliminary design phase will lead to the final choice. For the purposes of this document, the CESR-B cavity is baselined in order

to present self-consistent calculations of system parameters such as RF power and cryoplant requirements, coupled bunch growth rates, system mechanical layouts, and cost. Details of the HOM impedances and coupled bunch growth rates are given in Section 6.2.3.

To meet the initial requirements of 3.3 MV accelerating voltage and 408 kW beam power, two RF cavities with individual klystron transmitters are to be installed. A third cavity to be used as a test cavity / spare will be purchased as part of the baseline machine. It is expected that this cavity will be installed in a future upgrade as additional insertion devices increase the beam power requirement to beyond 2×270 kW, a soft limit of the power couplers in the CESR-B cavities. The CESR-B cavity parameters are given in Table 7.5.3.

Table 7.5.3   CESR-B Cavity Parameters.

Frequency [MHz]	499.46 +/- 0.2
Electric field (normalized to 0.3m) [MV/m]	>8 MV/m
Accelerating Voltage (beam energy gain) [MV]	>2.4 MV
Unloaded Q (at 8MV/m)	$>7*10^8$
Static heat losses [W]	<30 W
Dynamic heat losses (at 4.5k and 8MV/m) [W]	<120 W
Maximum power transferred to beam [kW]	>250 kW
Loaded Q	2×10^5

In addition to coupled bunch instabilities caused by higher order modes in the cavities, the fundamental and harmonic RF systems can cause instabilities where all of the bunches oscillate in unison, the so-called Robinson instabilities. The classical Robinson analysis [7.5.7] is particularly relevant for short and compressed bunch operation of the machine. The resistive Robinson instability is not excited by the cavities. This is due to the fact that the main cavities are detuned below resonance to compensate for beam loading, which strongly damps phase oscillations, while the harmonic cavities' very high quality factor greatly reduces the resistive part of their impedance at the synchrotron frequency, and hence their excitatory (or damping) influence on phase oscillations.

The second observation concerns the reactive Robinson instability. In this instability the static bunch distribution is an unstable fixed point of the longitudinal dynamics, and a perturbation of the bunch pushes it with some growth rate away from that distribution, subsequently damping to one of two stable distributions. In the absence of harmonic cavities, the bunch is marginally unstable. The addition of inductively detuned harmonic cavities for stretched bunches tend to suppress this problem; capacitively detuned harmonic cavities for compressed bunches aggravate the instability. In unstretched or compressed operation, however, the unmitigated instability results in only a small phase shift of the bunch due to the narrow potential well. But for stretched bunches the potential well is wide and flat, and the instability results in gross distortion of the bunches, which must be addressed. A simple cure, first recognized by Miyahara [7.5.8], is to introduce a small-bandwidth feedback of the RF system to the beam. Simulations also show that a reduction of the main-cavity impedance using RF feedback suppresses the instability, although too much feedback excites a higher-order oscillatory instability.

Although glossed over in the discussion to this point, with stretched bunches the classical Robinson picture is not so simply applicable; more involved analyses, such as those by Bosch et al. [7.5.9], and numerical simulations are required to assess the stability of higher-order modes of these bunches. As was just mentioned, the use of RF feedback, which allows the adjustment of the impedance of the main cavities, is a means by which some manipulation of bunch stability is possible. Our experience with the NSLS VUV ring also shows that short-range wakes can have an impact on the stability of stretched bunches, which is further complicated by the varying bunch profiles along the train.

7.5.2 500 MHz RF System

7.5.2.1 500 MHz Cavities

The CESR-B cavity consists of a bulk niobium SCRF single cell with waveguide coupler, a special fluted beampipe to extract the lowest frequency dipole modes, warm-to-cold transition spool pieces for thermal isolation, water-cooled C48 ferrite HOM dampers, and long tapers to transition from the 240 mm cavity bore to the elliptical beampipe. The CESR-B cavity is a "single-mode" cavity. All higher-order modes with the exception of the TM110 dipole mode propagate through the cylindrical beampipe. A fluted beampipe at the opposite end of the cavity has a lower cutoff frequency to allow the TM110 to propagate to the ferrite load. This has only a small effect on the fundamental mode. This allows a shorter attenuation length in the beam tube and a more compact cavity. The cavity assembly is shown in Figure 7.5.2. The layout of two CESR-B cavities plus a single Super3HC harmonic cavity in a single straight is shown in Figure 7.5.3.
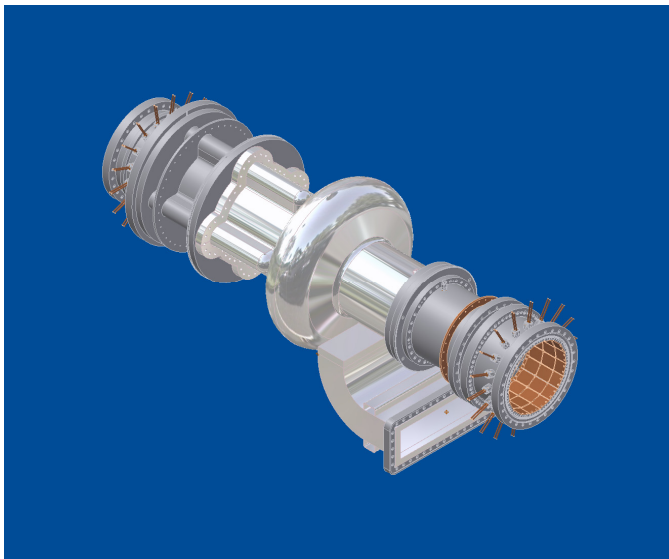
Figure 7.5.2 The CESR-B bare cavity assembly.
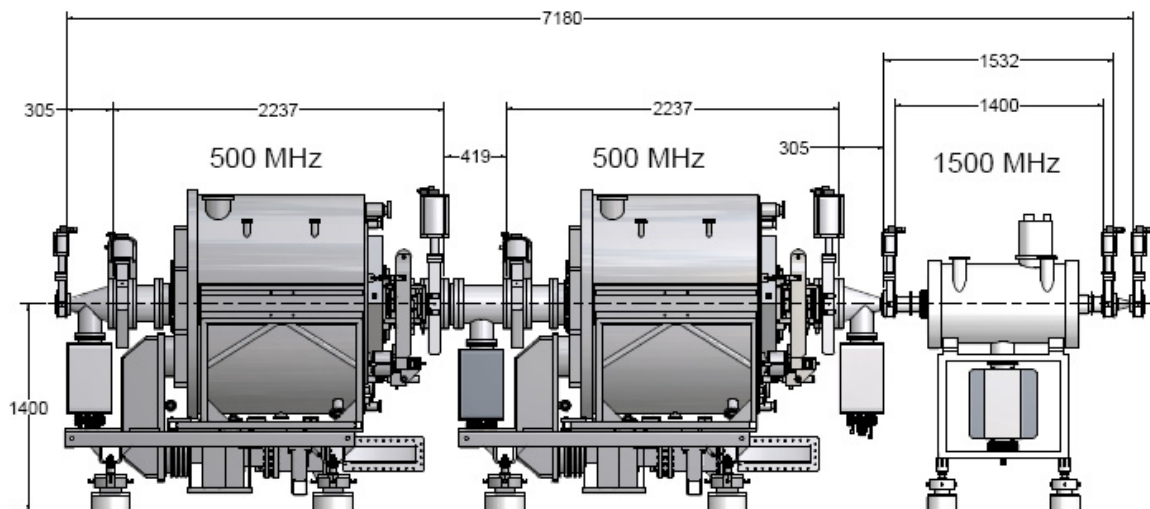
Figure 7.5.3 Layout of two 500 MHz cavities plus one 1500 MHz Landau cavity in a single straight. The tapers from the large cavity beampipe to the ring beampipe are ~300 mm long, limited by the available length in the straight of 7.18 m. A second RF straight is reserved for additional cavities.

7.5.2.2   HOM Damper

The HOM damper consists of C48 ferrite tiles brazed to water-cooled copper backing plates that form a spool piece outside the cryostat. The ferrite is several 500 MHz attenuation lengths away from the SC cavity. There is power dissipated in the ferrite from two sources. First, there is dissipation of the fundamental 500 MHz field driven by the transmitter. This has been calculated with CFISH [7.5.2, 7.5.10] to be less than 100 W at 2.5 MV cavity voltage. Second, the beam also loses energy from wakefields. This loss is given by

$$P_{loss} = k_{\parallel} \cdot \frac{I_0^2}{n} \, T_0 \, .$$

(7.5-4)

For NSLS-II, $T_0 = 2.6$ μs, $I_0 = 0.5$ A, and $k_{\parallel}$ ($\sigma_s = 4$ mm) = 3.6 V/pC, resulting in a $P_{loss} = 2.3$ kW. In the worst case, all of this power is lost in the ferrite, which is still a factor of 4 lower than the design limit.

7.5.2.3   KEK-B Cavity Option

The superconducting cavities developed for the KEK-B factory are being considered as an option for NSLS-II, for several reasons. The most significant advantage is the higher power per coupler, which has been demonstrated at KEK to be greater than 400 kW. In principle, two KEK cavities could meet the power requirements for the full complement of damping wigglers and user insertion devices, ~800 kW. The waveguide feed at the top of the cryostat makes the tunnel installation easier, and the coupling can be optimized for various beam currents and cavity voltages by simple spacers on the antennae coupling mounting flanges, as opposed to the fixed coupling of the waveguide feed for the CESR-B approach. A layout of two KEK-B cavities in an 8 m straight is shown in Figure 7.5.4.
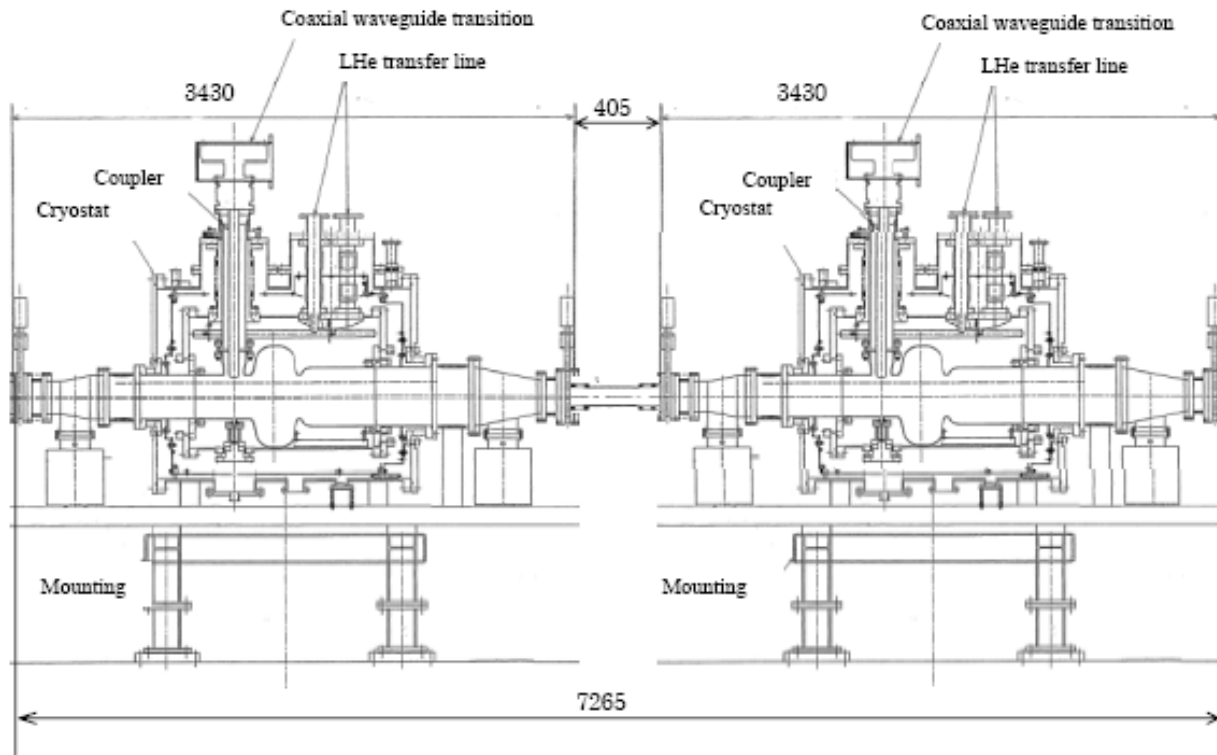

Figure 7.5.4   Installation of two KEK-B SCRF cavities in an 8 m straight.

7.5.2.4   RF Transmitter

The power couplers for SCRF cavities have a wide statistical variation in their power handling capability. Although they have been engineered for high power handling by proper thermal and electrical design, they are prone to multipacting, a resonant electron-avalanche effect that can impose a hard limit on power transmission and cause failure by local heating due to electron loading. The multipacting depends on the secondary-emission coefficient of the surface, which in turn depends on the properties of the bulk material, usually copper or niobium, and surface contaminants, which are usually cryo-pumped organics from the machine vacuum. These contaminants can be present at start-up or accumulate over a period of time, degrading performance and requiring, in the worst case, the cavity to be warmed up with a mild bake to drive off the condensed gases. Experience with the CESR-B cavities has shown transmitted power per coupler in the range of 250–330 kW. A transmitted power of 270 kW is assumed for meeting machine requirements and placing a limit on installed RF power. In addition to the energy losses due to radiation in dipoles, damping wigglers, and undulators, the RF power transmitter and coupler must provide for the HOM losses that are excited by the beam. We are exploring ways of increasing the power per coupler, and will factor this into the preliminary design and choice of transmitter power.

The coupling of the waveguide to the cavity in the ideal case is adjusted so that the cavity presents a matched load to the RF source at the normal operating current and energy. Since there is a phased installation of cavities and insertion devices, this optimal coupling varies over the life of the machine. The KEK-B cavity has an adjustable antennae coupler that, in principle, can be changed to follow the optimal coupling. In practice, this must be done in a cleanroom environment and may be of limited value.

For an aperture-coupled cavity such as the CESR-B, coupling is set during the design and manufacture. Usually coupling is set so the generator is matched to the cavity at the highest expected beam-loading (beam power) of 270 kW. This minimizes the requirement on installed RF power. For the staged installation of insertion devices (RF power required) and RF cavities there is not a single minima, and it is necessary to balance the mismatch over the different phases. For an approximate match to the conditions in Phase 3 in Table 7.5.2, the maximum reflected power in the other three phases is ~10.5 kW. In order to reduce the residual reflected power during commissioning and staged insertion device installation, a 3-stub waveguide tuner will be installed between the circulator and the cavity.

There will be variation of the impedance presented by the cavities to the beam at different times of the machine's life due to the varying number of cavities and insertion devices. RF feedback can be used to reduce (or increase) this impedance; this option is being studied and system layout designed to minimize loop delay to allow its implementation. A minimum transmitter power of 275 kW is required to meet the sum of the radiated, HOM, and reflected power demands. To allow for the case of coupler improvement (coupler is limited by multipacting, not power limitations) or system aging (degradation of klystron output power), the transmitter will be designed for a minimum of 310 kW, allowing up to ~280–300 kW per coupler.

A single 310 kW klystron amplifier will drive each of the main ring cavities through a 350 kW rated circulator and load. Klystrons that meet or exceed this power level are available from three vendors: CPI, Toshiba, and Thompson. The klystron beam power will be provided by a Pulse Step Modulation switching power supply at 55 kV and 12 A. The PSM switching power supplies have the benefit of low stored energy, and fast turn-off capability of the IGBTs, eliminating the need for a crowbar circuit to protect the klystron. The power supply will have redundant switching cards built in, and will operate at full capacity even with several card failures. The RF transmitter will have local control via PLC, with system parameters and control available to the main control system via an Ethernet link. The PLC will also monitor the PSM switch modules, so that failed modules are logged and transmitter repairs can be scheduled for the next maintenance period. The main ring power systems with a rating of 310 kW are beyond the power limit of air-cooled coaxial cable, and will be implemented in WR1800 waveguide. A layout of the RF straight with the associated RF transmitters is shown in Figure 7.5.5.
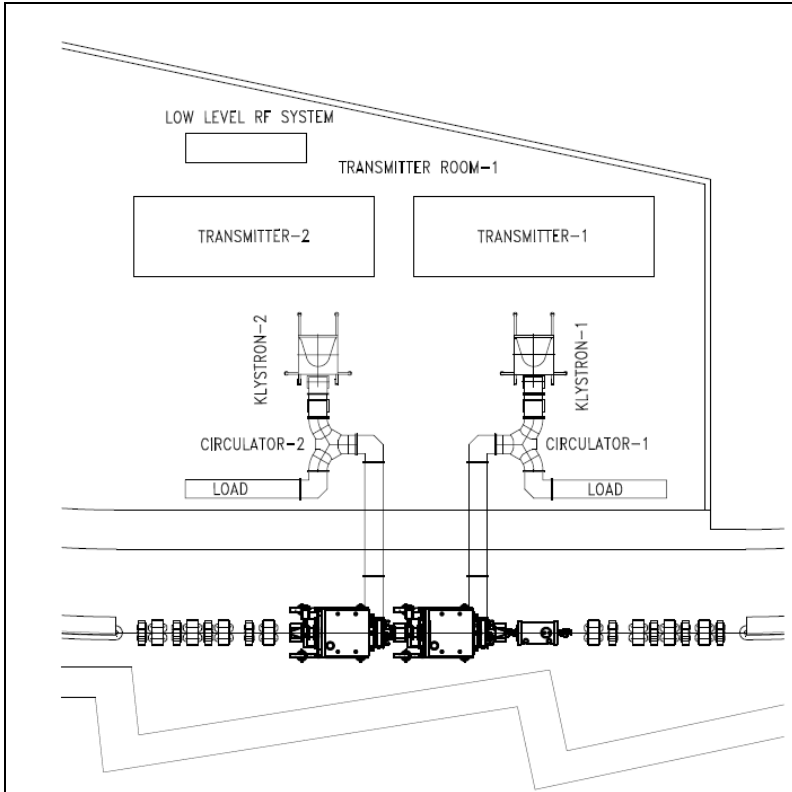
Figure 7.5.5 Layout of an RF straight section with two 500 MHz cavities and their klystron transmitters and a single 1500 MHz harmonic cavity.

An alternative approach of combining several Inductive Output Tube amplifiers to obtain the necessary RF power has been developed at other facilities [7.5.11, 7.5.12]. IOT systems have higher efficiencies and some limited failure tolerance. Likewise several hundreds of high-power transistors can be combined to provide the required power. SOLEIL has recently commissioned such a system at 352 MHz [7.5.13]. Both of these options will be explored in detail during the design phase.

7.5.3   1500 MHz Harmonic Cavity System

A passive 1500 MHz SCRF cavity, such as the BESSY scaled CESR-B [7.5.14] or Super3HC [7.5.15] scaled SOLEIL cavity, has been studied for the Landau cavity in NSLS-II. Both of these cavities can achieve ~0.5 MV per cell, with the BESSY cavity containing a single cell, and the Super3HC containing two cells per cavity. The details of the impact of the Landau cavity have been discussed in Section 6.2.7 on collective effects. Here we will discuss the hardware and system configuration. For this purpose, two cells of the Super3HC Y design will be used in the estimate.

The nominal voltage and phase of the harmonic cavity is that which cancels the slope and second derivative with respect to time of the total RF field. This results in bunches lengthened by approximately the ratio of the harmonic-to-main cavity frequencies. The field required of the harmonic cavity is approximately the reciprocal of that ratio times the main-cavity field, although slightly less due to the non-zero main-cavity synchronous phase that is a consequence of the beam's radiation loss. In practice, this harmonic-cavity field is pushed slightly higher to provide additional stretching, striking a balance between improved lifetime and the eventual onset of longitudinal instabilities. Furthermore, the use of a gap in the ring's fill pattern for ion clearing results in perturbations of the potential wells that vary along the train. As a result, the lengths of most bunches are shortened by these perturbations and the average lifetime is reduced. For these reasons, the harmonic-cavity field and phase require further investigation. Simulations shown in Section 6.2.7 give a

maximum in bunch length for ~1.1 MV of third-harmonic voltage for the initial fundamental cavity voltage of 3.4 MV. This can be met with a single Super3HC cavity. As the number of damping wigglers and user insertion devices increases, the fundamental mode voltage increases to 4.8 MV and an additional third-harmonic cavity will be necessary for optimal bunch lengthening.

7.5.4   Low-Level RF and Beam Control

The specifications of the RF system amplitude and phase requirements are derived in part from the user requirements that the transverse motion of the photon beam is to be <10% of the RMS beam size, and the increase in photon beam size due to emittance dilution of the electron beam is to be <10%. The relation of the photon beam size and jitter to electron beam size and jitter is influenced by the design of a particular insertion device and beamline, which might impose a tighter tolerance on the electron beam stability. The stability required from the RF system to limit the transverse jitter of the electron beam to 10% beam size is derived below. This will be expanded to study the effect on the photon beam in the next phase of design.

The electron beam size is given by

$$\sigma_x = \sqrt{\beta_x \varepsilon_x + \left(\eta_x \delta\right)^2} \ . \tag{7.5-5}$$

Since the residual dispersion in the ID straights is expected to be on the order of 1 mm, and the natural momentum spread ~1×10^{-3}, the dispersive term is negligible and the beam size depends only on the emittance and the beta function at the ID. For the 5 meter straights, $\beta_x = 2.7$ and $\varepsilon_x = 0.6 \times 10^{-9}$, corresponding to a beam size of 40 microns in the horizontal plane. Similarly, in the vertical plane for $\beta_y = 0.95$ and $\varepsilon_y = 0.6 \times 10^{-11}$, the vertical beam size is ~2.4 microns. The orbit jitter is given by

$$\Delta_{x,y} = \frac{\Delta p}{p} \eta_{x,y} . \tag{7.5-6}$$

In order to restrict the beam jitter to ~10% of beam size with a residual vertical dispersion of 1 mm, the momentum jitter must be less than 2.4×10^{-4}; the horizontal plane is less demanding. For the NSLS-II RF system, this corresponds to a 0.7 degree phase jitter.

The longitudinal beam stability derives in part from timing experiments. Even though these users employ a photodiode detection system to determine the arrival time, the limited bandwidth (~1 kHz) sets strict requirements for the jitter tolerance to be 5% of the RMS bunch length over the frequency range of 500 Hz to 50 kHz. This corresponds to a bunch phase tolerance of 0.12 degrees, for timescales comparable to the synchrotron period this is a tolerance on the RF phase as well. An example of the impact of emittance dilution is from user beamlines employing the radiation of higher harmonics, whose spectral purity and beam spot size depends on the momentum spread and momentum jitter of the electron beam. So it is a requirement of the RF systems to not contribute significantly to energy spread or jitter, either through instabilities or noise. While suppression of instabilities is already a basic requirement of the system, a cap on energy spread provides a constraint on the noise the RF system contributes to the beam.

The magnitude of the effect on the beam of RF phase and amplitude noise depends on whether the source of the RF jitter is random or harmonic (systematic). Sources of noise are broadly classified into continuum sources possessing a continuous and slowly varying (with respect to frequency) spectral density, and spurious sources that possess spectral lines, possibly varying in time. Examples of the former are the continuum component of synthesizer phase noise, amplifier shot noise, and the continuum components of other active devices in the RF system. Examples of the latter are line related and power-supply switching noise, microphonics, and vibration. To assess the impact of, and derive tolerances for, RF-system noise sources, we need to determine the beam's sensitivity to noise from identified sources and derive a tolerance budget. The

sensitivities are to be determined by modeling the RF system's linear response to these sources. Noise magnitudes in existing machines are a starting point for noise intensities, from which sensitivities are used to determine where noise tolerances need to be tightened. This work is in progress, and will be expanded in the preliminary design phase. Digital low-level RF systems have achieved less than 0.1 degree phase and 0.1% amplitude stability [7.5.16], these tolerances should be sufficient for NSLS-II.

7.5.4.1   Master Oscillator and Ring Frequency Synthesizers

The low-level RF and beam control design is at a preliminary stage of defining specifications and architecture. Unlike the power systems, which stay relatively static over long periods of time during the life of the machine and should be transparent to the user, the LLRF and beam control requirements may change several times as the machine evolves, so the design must be flexible. To this end a digital architecture is used. There are several approaches being studied; we present one here as an example. This is similar to the system proposed by Horrabin and Dykes [7.5.17] for Diamond Light Source.

An ultra stable Master Oscillator, offset from the fundamental RF frequency, is mixed with a Direct Digital Synthesizer to provide the ring frequency. This will allow for future implementation of a radial (frequency) feedback loop to stabilize the beam orbit to the sub-micron level. Depending on future considerations, there may be individual DDSs for the booster, ring, and feedback systems, or all systems may be driven by the ring DDS. Separating the systems would allow the booster to synchronize with the linac for injection and then synchronize to the ring for extraction, decoupling the injector from the ring. An example of such a system is shown in Figure 7.5.6. A wide range of Master Oscillator and IF frequencies are feasible, and the exact frequencies would be determined in the design phase.
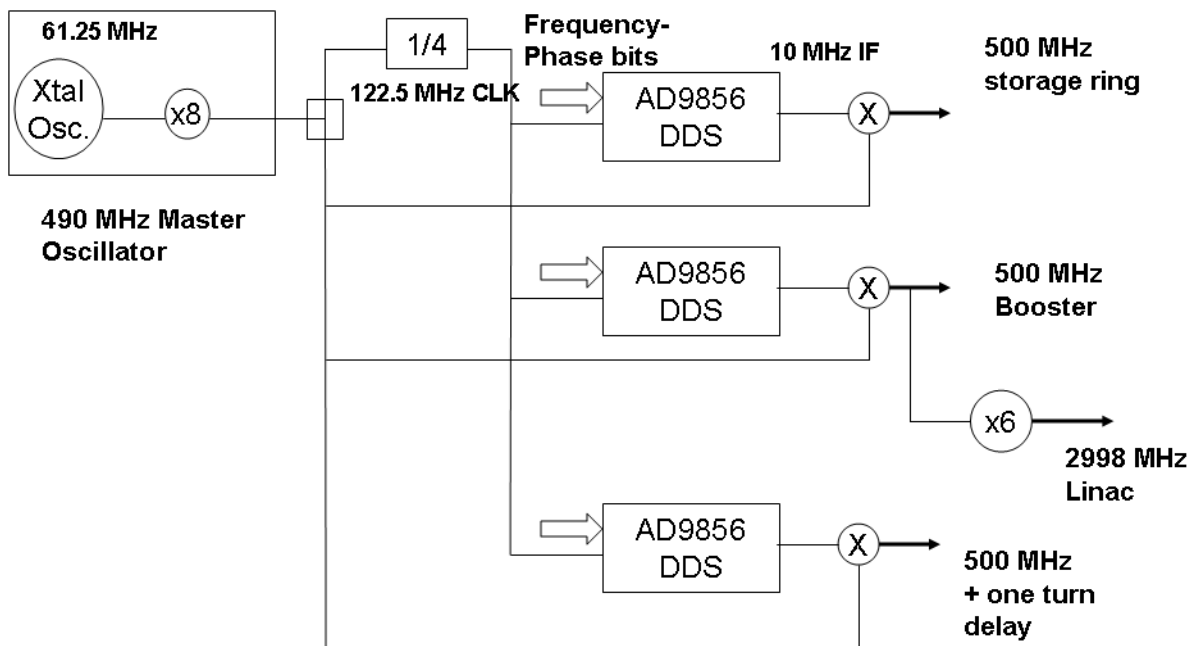

Figure 7.5.6   Example of master oscillator.

7.5.4.2   Cavity Controllers

The cavity-amplifier system has several nested feedback loops to control the amplitude and phase of the RF cavity fields in the presence of beam-loading, mechanical perturbations to the cavity, and residual klystron noise due to power line/DC power supply ripple. The innermost loop is the tuner loop, which tunes the cavity resonance in order to present a purely resistive impedance to the klystron, thus minimizing klystron power. This loop, which is closed around a mechanical tuner, is slow—on the order of 1 Hz. Next is an RF feedback loop that is used to adjust the impedance of the main-cavity accelerating mode. In order to stabilize the cavity fields against fast perturbations, an amplitude and phase loop around the klystron-cavity chain is implemented. Although these can be independent loops, it is more effective to combine them in a common In-phase and Quadrature (I/Q) modulation loop, due to the coupling of the loops by cavity detuning for beam loading.

In addition to the above RF, amplitude, phase, and tuner loops, it may be necessary to implement other loops. A loop for zero-order coupled-bunch-mode feedback from the beam to the RF system to damp Robinson or higher-order longitudinal instabilities may be necessary. A klystron amplitude/phase loop to linearize the klystron, and possibly a feed-forward loop on the anode modulation of the klystron for maximizing klystron efficiency under different operating conditions, may also prove useful.

With the exception of RF feedback, the above loops can be implemented in either analog or digital hardware. Analog systems have the advantage of being simpler and less expensive to produce, and have higher speed and bandwidth. Their disadvantages include the lack of flexibility in changing loop characteristics for varying beam loading, slightly less phase and amplitude accuracy, and DC shifts that are more difficult to control. Digital implementation has the advantage of flexibility, in particular of being able to synthesize the loop filters digitally so that the feedback loops can be programmed for different machine states. Higher accuracy can be achieved, and DC drifts are easier to control. This comes at the price of higher complexity, and requires an additional skill set in high-speed digital design. Careful attention must be paid during the design stage to design in "digital probes" and other debugging tools to monitor and allow trouble shooting of the digital feedback loops.

To maximize the performance of the RF system and allow simple optimization and upgrades over the life of the machine, a digital implementation is our choice for NSLS-II.

The low-level RF cavity field control will be via a digital I/Q modulator-demodulator incorporating up and down conversion, ADCs and DACs interfaced to the digital baseband signal processing, a Field Programmable Gate Array state machine, and interface to the control system. Similar systems have been designed for both hadron and electron machines in recent years [7.5.18, 7.5.19]. A particularly attractive approach is the Cornell design, which has been operating in CESR with the SCRF cavities over the past two years. The system was developed within the VME architecture at Cornell. PC104 and compact PCI architectures for the NSLS-II LLRF system will be explored in the preliminary design phase.

Although the booster RF is simpler because there is only one cavity (no vector sum), and harmonic cavities are easier because they are passive, we assume at this stage that identical storage ring controllers will be used, with the only differences being how they are programmed and their interface with the control system.

7.5.5 Cryogenics

A helium closed-cycle cryogenic system is necessary to provide liquid helium to the superconducting radio frequency cavities. Two 500 MHz (fundamental) and one double cell, 1500 MHz (harmonic) SRF modules for the main storage ring must be maintained at approximately 4.5K during operation of the storage ring and booster. Additional cooling lines and capacity may be needed to cool one 500 MHz SRF cavity to 4.5K for offline development purposes. The cryogenic system includes a refrigerator/liquefier cold box, a main compressor and oil removal system, a recovery compressor and oil removal system, LHe dewars, LHe and liquid nitrogen distributing systems, a gaseous helium management system, cryogenic lines, instrumentation, controls, and safety devices. Each cavity cryostat has a volume of 500 L and stores 400 L of LHe during operation.

7.5.5.1 Factors Influencing Cryogenic System Design

7.5.5.1.1 Single vs. Multiple Refrigerators

The refrigeration system needs to have high reliability with near-zero unscheduled downtime. Using risk and failure analysis criteria, we compared similar systems that use either one large refrigerator or multiple refrigerators. A study to determine the sources of unavailability in existing cryogenic refrigeration systems was undertaken in the past by the TESLA Collaboration at DESY. The results are listed in Table 7.5.4, in order of their occurrence frequency.

Table 7.5.4   Rating of Refrigerator System Unavailability.

Rating	Topic	Example	Multiple Refrigerators
1	External Utility Failure	Electrical power, cooling water, instrument failure	No advantage
2	Blockage by frozen gas or impurities	Air and/or water vapor	Somewhat larger risk tolerance provided
3	Operational problems	Operators, controls, instrumentation,	Greater risk due to more system complexity
4	Single component failure not leading to total plant shutdown	Electrical motor burnout, compressor bearings, leaking oil pump seal, turbine bearing trouble	No advantage over component redundancy within a single refrigerator
5	Catastrophic component failure leading to plant shutdown	Loss of insulation vacuum, rupture of heat exchanger, oil spill into cold process piping	Would have a positive effect

From the information in the table above, we can predict that major downtime will occur as a result of catastrophic component failure, while the effect of any of the other four occurrences is relatively negligible. After consulting with experts and researching other sources that faced similar circumstances, a single refrigerator was selected. To lower risk however, a full inventory of spare components will be required, as well as strict adherence to the individual manufacturer's recommended maintenance schedule.

7.5.5.1.2 Constant versus Variable Loads

The reliability factor is increased by designing refrigerators that are capable of operating efficiently at partial load. When the accelerator is operated at reduced load, or when all modules are not in use, the electrical power and utility usage will be proportionally reduced. This is achieved by automatically modulating the discharge pressure and mass flow rate of the main compressors to match the actual load.

7.5.5.1.3   With or Without External Gas Purity Monitoring System

Gas impurities have an adverse effect on R/L efficiency. Air, for instance, solidifies at approximately 50K. Small solidified air particles can damage the expansion turbine, which runs at a high rotational speed; thus the concentration of impurities in the helium gas must be maintained at less than 10 ppm. The R/L internal adsorber is one source of purification; however, additional external purifiers to further enhance the gas purity level are suggested. At least one external purifier that can operate at partial mass flow rates is recommended. To conserve budget, this has not been included initially, but will installed at a later date, as soon as sufficient budget is available.

7.5.5.2   Mechanical Design Parameters

7.5.5.2.1   Heat Load Budget

There are essentially two types of heat loads: static and dynamic. The static heat loads of the RF cavity cryostats are measured values, recorded by other synchrotron facilities. The dynamic heat loads are calculated based on physics requirements. Heat loads associated with transfer lines, valve boxes, dewar losses, and other components are estimated values based on information provided by vendors, engineering calculations, and professional judgment. Table 7.5.5 itemizes the estimated static and dynamic heat loads of the superconducting cavities and associated cryogenic components at 4.5K.

The waveguides for the 500 MHz cavities operate in liquefaction mode, whereby each requires 5.3 l/hr of LHe for cooling. There is one distribution valve box serving as flow distribution between the LHe dewar and the straight section cryostats.

Table 7.5.5   Cryogenic System Heat Loads Budget and Refrigeration Sizing.

Component(s)	Two Cavities [W]	Three Cavities [W]
500 MHz Cavity (Static + Dynamic (Main Ring)	(25 + 98) x 2	(25 + 65) x 3
RF Valve Box (vendor)	15	15
Wave Guide (NSRRC)	8	12
Harmonic Cavities (Static + Dynamic)	(50 + 50)	(50 + 50)
Transfer lines (0.5 W/m), 50 m	25	25
Dewar loss	5	~5
Subtotal	399	427
R/L with 40% (239 – 268 W) margin	665	712

The projected LN2 required to cool the R/L heat exchangers, SRF modules, and transfer line/valve heat shields is listed in Table 7.5.6.

Table 7.5.6   Cryogenic System Liquid Nitrogen Consumption Estimates.

Component(s)	Two Cavities [L/hr]	Three Cavities [L/hr]
500 MHz cavity	20	30
Harmonic cavities	10	10
Cold Box, 10 pre-cooler	10	10
RF valve box (1)	12	12
Transfer lines (1 W/m), 50 m	12	12
Subtotal	64	74
Margin (20% of subtotal)	13	15
Total	77	89

7.5.5.2.2   Engineering Design Approach

The main storage ring RF systems will initially consist of one 1500 MHz (harmonic) and two 500 MHz (fundamental) Superconducting RF Cavities.

The cryogenic system must operate continuously for at least a full year before scheduled downtime. The design goal, therefore, is to provide a highly reliable and stable cryogenic system supported with required monitoring, alarms, interlocks, and a safety and control system. As the cryogenic system must supply LHe to all of the RF cavities, redundancy of vulnerable components is highly desirable to ensure that continuous operations can be maintained effectively.

Total refrigeration cooling requirements are based on the accumulated heat loads of one double-cell 1500 MHz and two 500 MHz SRF cavities operating simultaneously (see Table 7.5.6). The cryogenic system must minimally provide refrigeration power of 399 W. To enhance reliability, the refrigerator is sized to operate at 60% of its peak cooling capacity, which will reduce wear and tear while providing a comfortable 40% safety margin Therefore, an R/L capable of 700 W cooling capacity (with the LN2 pre cooler) will be specified for this application. The basic cryogenic system flow diagram is shown in Figure 7.5.7.

A single 3,000 L dewar will serve as a buffer storage vessel between the R/L cold box and the RF distribution valve box. The dewar volume is more than twice the volume of total LHe stored in all SRF modules. This reserve volume is estimated to maintain nearly six hours of continuous operation while troubleshooting or minor repairs are being conducted. A carefully planned control system will regulate the LHe production rate to maintain the stored liquid volume in the dewar at the desired level.

A single compressor with an oil removal system will deliver pressurized helium gas to the R/L. An identical compressor/oil removal system will be installed in parallel as a back-up. It must remain ready to operate in the event of an unexpected failure of the main compressor. These two compressors will also alternatively cycle to extend their overall life time. Both compressors will be equipped with a frequency driver to match the cooling load to the compressor's output to maximize system efficiency. A single uninterrupted recovery compressor, along with an oil removal system, will recover the generated boil-off gas in the event of loss of power to the main compressors.

A single gas management system will regulate GHe during various operational conditions. Three 70m^3 tanks capable of storing all generated GHe during warm-up will be used. Two control valves working in concert will regulate GHe flow between the compressor and helium storage tanks.

A gas purifying/monitoring system is not included at this time but it is suggested for sampling the circulating GHe to monitoring purity levels.
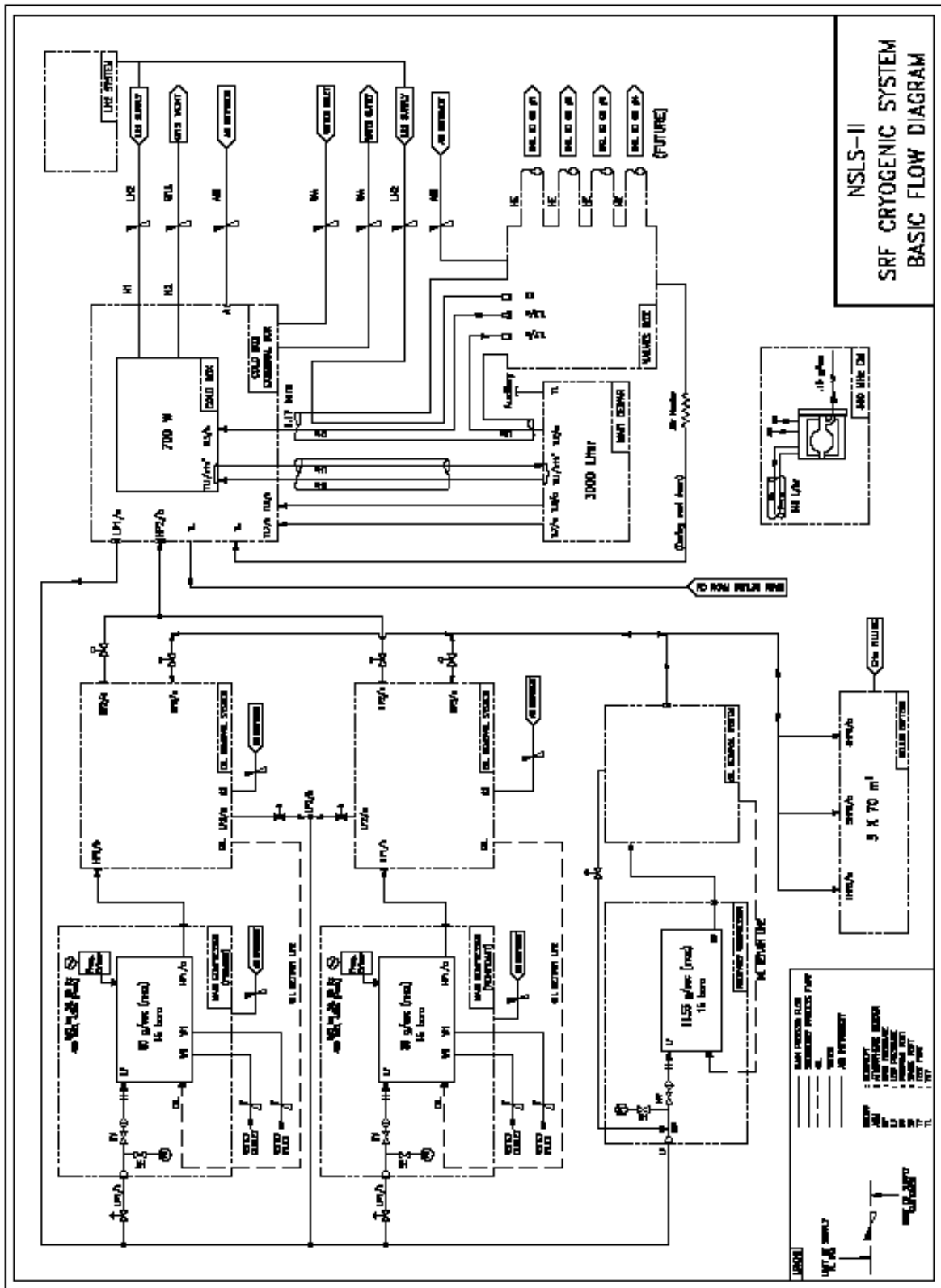
Figure 7.5.7 Basic Cryogenic System Flow Diagram.

As the cryogenic system will be purchased with documentation, as required to meet NSLS-II requirements, interfaces with SRF cryostats and machine control system will be developed during the overall system design. In summary, the major components of the cryogenic system include:

- two screw-type helium compressors and oil removal sets equipped with frequency drivers, where one will act as hot standby
- one turbo-expander type refrigerator–liquefier cold boxes with maximum combined cooling capacity of 700 W
- one gas management system consisting of three carbon steel warm GHe tanks (70 m^3 each)
- one main LHe dewar (3000 L)
- one cryogenic distribution valve boxes capable of serving four SRF cryo-modules
- multi-channel, vacuum-jacketed, LN2 transfer lines with length and size to be determined later
- single vacuum-jacketed LN2 transfer lines, with length and size to be determined later
- appropriate length/size of vacuum jacketed LN2 transfer line
- stainless steel piping for GHe supply and return
- an 84000 L bulk Liquid Nitrogen storage tank to deliver LN2 throughout the system
- central process and control system (including software, hardware, and standard communication ports to provide intelligent to machine control system)
- the appropriate number and type of warm-cold valves, safety devices
- instrumentation, such as pressure/temperature transmitters, gauges, etc.
- a hazard monitoring and control system

Other features for the closed-loop cryogenic system are briefly described as follows:

- The helium compressor sets will be located in a detached compressor room at sufficient distance from the main building to minimize environmental effects such as noise (72 db at 1 m distance) and vibration to the machine/personnel.
- The refrigerator/liquefier cold box and the main LHe dewar will be located in a "cryogenics room" located adjacent to the inner wall between two RF straight sections.
- Three helium gas buffer tanks (70 m^3 each) will act as make-up and recovery of GHe together with a GHe refill tube trailer, which will be located on a platform adjacent to the compressor room.
- Associated helium gas piping will interconnect the components according to the PID drawing (to be developed later).
- One cryogenic distribution control valve box will supply the SRF cavities with required LHe flow to be located adjacent to an RF straight section.
- Multi-channel vacuum-jacketed lines will deliver LHe and GHe between the R/Ls and the storage dewar.
- LHe will be transferred from the main LHe dewar using a positive pressure difference from the helium dewar through a multi-channel line, or by using a set of vacuum-jacketed transfer lines to the cryogenic distribution valve box, and then through a set of cryogenic flexible transfer lines, to the main SRF modules.
- A 84,000 L LN2 storage tank will supply required LN2 to the cryogenic system and SRF cavities, and will be located outside main building. An automated telemetry system will be used to maintain safe LN2 volume and tank operating pressure (3.0 bar absolute).
- A large capacity, LN2 phase separator will be placed next to the cryogenic room (due to intermittent excess noise level), for delivery of constant pressure LN2 to the SRF modules and to the R/L, which are all sensitive to pressure fluctuations.
- Vacuum-jacketed transfer lines will deliver and distribute required LN2 to the cryogenic room and SRF modules.
- A central control monitoring system located in the cryogenic room will act as interface between operators and various components.
- Installation of O2 monitors and interlock systems in all enclosed areas (tunnel, cryogenic, and compressor rooms) will guard personnel against potential Oxygen Deficiency Hazards.

The following section briefly describes functional characteristics of main components.

7.5.5.2.3   Refrigerator/Liquefier Cold Box

The refrigerator/liquefier cold box is required to reliably produce combined 700 W of refrigeration and LHe at 4.5K. The principle design of R/L is based on a two-turbine, in series, Claude Cycle with six stages of heat exchangers (see Figure 7.5.7). The gas-bearing turbine expander-type 4.5K R/Ls have demonstrated reliability and efficiency during the past 30 years. Commercially-manufactured systems such as Air Liquide's HELIAL and Linde's TFC models have been used by other synchrotron facilities and equipped with comprehensive instrumentation and control systems.

High-pressure helium gas from the compression system enters the cold box system at 298K. Following removal of impurities in the inlet via a <50 micron filter, the flow is fed to a series of heat exchangers that are cooled by the returning low-pressure gas stream. LN2 is used as to pre-cool the first heat exchanger and to help cool the HP stream to 80K. At the outlet of the second heat exchanger, the HP stream is then fed into an 80K adsorber, where air pollutants are removed. The stream exits the particulate filter downstream of the adsorber and is then split into two parts: the gas that is expanded in the two turbines in series (in the so-called Brayton Cycle part), and the gas that is processed in the Joule-Thomson circuit (in the so-called Joule-Thomson cycle part).

The expansion turbines include a stator and a rotor. The rotor consists of a cold wheel, a brake wheel, and a gas bearing. Fully automated R/Ls with control systems driven by PLCs are preferred. Some of the automation features under consideration are:

- automatic re-start of liquefier after a breakdown of electrical power, cooling water, or instrument air
- the capability to start and stop safely at any time and under any condition without requiring special precautions
- remote monitoring capability from onsite or offsite locations
- the capability to perform remote diagnostics and troubleshooting (from onsite or offsite)

7.5.5.2.4   Liquid Helium Storage Dewars

A single 3,000 L LHe dewar is used for liquid storage and to transfer LHe to the SRF modules through the cryogenic distribution valve box via a differential pressure transfer. The main LHe dewar acts as a buffer and stores sufficient liquid during cool-down, warm-up, and normal operation. The 3,000 L capacity was selected to provide at least six hours of uninterrupted operation while minor troubleshooting is being conducted.

The dewar will be constructed using an inner insulated vacuum vessel and an outer vessel, both made of 304 stainless steel. There will be adequate access ports for helium transfer and instrumentation. There will be an additional inlet for feeding the dewar from an external source, should this be necessary. The main parameters and some of the design features are as follows:

- maximum operating pressure: 2 bar absolute
- steady-state operating pressure: 1.2 to 1.6 bar absolute (17.4 – 23.2 psia)
- dewar pressure fluctuation: ±3 mbar (0.0435 psi)
- insulating Vacuum Pressure: $<1.0 \times 10^{-5}$ mbar, sustainable of >5 years, when dewar is cold
- dewar level fluctuation during steady state operation: ±1% of full scale
- level indicator/sensor resolution: 1% of digital display
- radiation shields will be cooled with helium boil-off (LN2 shields are not permitted). The boil off gas will be sent to compressor suction line, through a series of check valves.
- maximum allowable heat leak, including penetrations and necks: 5 W

- Dual 500 W heaters (removable, one as spare) with one DC power supply/controller installed inside the main liquid dewar for capacity and refrigerators control purposes. The heater load will be controlled by a dedicated PID controller reading the LHe level sensor.
- Heater resolution: ±5 W
- Two superconducting LHe level detectors/sensors (a differential pressure level detector is not acceptable) and one indicator
- Two redundant pressure transmitters will provide remote monitoring of dewar vapor pressure.
- A mechanical pressure gauge with resolution of 0.25% full scale and with a maximum of 2.5 bara full-scale for local measurement of the helium vapor pressure
- The LHe vessels have dual in-line relief valves and a rupture disk to handle vaporized gas in case of catastrophic event such as fire or loss of vacuum. The pressure settings of the burst disk will follow the ASME code.
- The outer vessel will be equipped with vacuum pump-out port, mechanical pressure gauge, and pressure transmitter.

The access ports and penetrations are:

- MCL for transfer of LHe and vapor return between R/L and LHe dewar
- MCL for transfer of LHe and vapor return between the dewar and RF distribution valve box (to be sized for liquid transfer rate during cool down and normal operation of SRF cavities)
- one port for external fill/withdrawal at 500 L/hr flow (for simultaneous operation of three fundamental and one harmonic cavity at a pressure difference of 2 psi)
- one combined for relief/burst disk system and normal warm-up

All other applicable manufacturing and design requirements will be specified during the next design phase.

7.5.5.2.5 Main Helium Compressor Stations

Two oil-lubricated screw-type compressors (one as hot standby) will be designed to feed (at max) 80 g/s at 15 bar absolute of pressurized GHe to the R/L box. On the discharge side of each compressor station, the helium and oil mixture will first undergo separation in the bulk oil separator. At the outlet of the compressor, the temperatures of the helium and oil gas mixture reach about 395K. This is cooled down to 298K in a water-cooled heat exchanger. The helium stream then flows through the final oil removal system, whereby the remaining oil (either aerosols or vapor) is removed. Oil coming from the separator is first cooled by a water-cooled heat exchanger and then re-injected into the compressor.

Each compressor will be equipped with a frequency driver, housed in an external cabinet. The drive motor of the compressor package should therefore be able to control load variation between 20 Hz to 60 Hz (corresponding to one-third to full flow). The screw compressors inherently are low-vibration machines that normally do not require massive foundations. Vibration dampers, however, will be identified and implemented at the time of installation.

A systematic maintenance program will be implemented to reduce the possibility of unscheduled downtime during normal operation.

7.5.5.2.6 Helium Recovery Compressor

An automatically operated screw-type recovery compressor with mass flow rate of at least 11.53 g/s, equipped with uninterrupted power supply, will be used to pump the generated helium gases from warmup or shutdown to the GHe storage tanks without loss of helium. This compressor will have same pressure characteristics (1.05 bara suction and 15 bara discharge pressure) with a minimum flow rate of 4.56 m^3/min. The start time of emergency power will be about 20 s, to avoid the difficulty of starting at high suction pressure.

The recovery compressor will start pumping at about 1.22 bara immediately if the main cryogenic plant shuts down or the suction line pressure drops below 1.08 bara. The recovery compressor will be able to switch to full gas flow automatically when the suction line pressure reaches 1.36 bara again during a 2-hour period. The recovery compressor's start time to achieve full capacity will be set during the operational testing phase.

7.5.5.2.7   Gas Management

Helium inventory in the refrigeration system is automatically adjusted by the gas management system as the refrigeration/ liquefaction load changes. The gas management system will consist of two control valves. One valve automatically sends excess helium to the buffers (for example, during quenches or warmups) One valve adds helium to the system from the buffer tank when the liquefaction capacity is higher than flow recovered from loads.

These two valves work in concert with the bypass recycle valve, which automatically recycles excess flow from compressor discharge to suction. These two valves control the liquefaction and refrigeration rate. A frequency driver will reduce the total cycle mass flow rate in case of excess flow from the compressors.

An automatic pressure-controlled bypass valve will be installed between the discharge line and the suction line of each compressor. This bypass valve will form a closed loop with the main compressors, to maintain and limit the discharge pressure.

Pressure transmitters and indicators with analog or digital output will be installed on both the discharge and suction lines near the main compressors. Similar transmitters will be installed near the suction side of the distribution valves boxes. Both compressors will be equipped with suitable suction and discharge relief valves.

Several spare ports with shut-off valves will be placed on both the discharge and suction lines in the compressor room and also on the high-pressure line near the refrigerators/liquefiers. The makeup/recovery control valves will be in the compressor room. Several other smaller ports will be on both the discharge and suction lines of the compressors and oil removals for gauges, sensors, and gas sampling purposes.

7.5.5.2.8   GHe Storage Tanks

Three tanks, each with water volume of 70 m^3, will serve as GHe recovery and makeup storage volumes. These tanks will be designed for a gauge pressure of 20 bar (290 psig). The maximum operating pressure will be the same as the maximum discharge pressure of the recovery compressors, 15 bar absolute (217.7 psia). The minimum operating gauge pressure is 2 bar (29 psig). The minimum design gauge pressure will be –1 bar for evacuation purposes. The design specifications will include all appropriate ASME Boiler and Pressure Vessel Codes, Section VIII, Divisions I (Unfired Pressure Vessels) and IX (Welding and Brazing Qualification), and Safety Relief Valves. Material and other geometric features will be detailed before purchasing.

7.5.5.2.9   Ballast and Surge Tanks

These tanks will stabilize pressure variations from the refrigerators' operation. Ballast tanks with the same design pressure as the buffer tanks will be installed at the high-pressure inlet side of the refrigerator. The surge tanks will be designed for lower pressure and will be installed near the suction side of the compressor. Both of these tanks will have an approximate volume of five m^3 and will be built with all applicable pressure vessel codes and safety devices.

7.5.5.2.10   Insulating Vacuum Pumping System

All vacuum insulating space must have pressure lower than 10^{-4} Torr for optimum performance. For this reason, a two-stage pumping set is recommended. The primary pump will be a rotary vane roughing

mechanical pump. This pump will be connected in series with a secondary oil diffusion pump, which will be capable of attaining a vacuum level of 10^{-6} Torr at cold conditions. The process controllers will control the vacuum pumps based on information from vacuum relay signals/gauges. The size of this mechanical vacuum pump will be determined based on final design needs. The vacuum pump will have primary vacuum valves and vacuum gauges to allow remote control of the vacuum system.

7.5.5.2.11   Valves

Different types of valves will be used throughout the cryogenic system. All valve seals will be soft seat and replaceable. Warm, noncontrol valves will be vacuum-tight ball valves with elastomer seats and seals or all-metal diaphragm-type refrigeration valves. Cold valves will be of low heat-leak extended stem design. All valves, with the exception of the JT and compressors bypass valves, will be selected without having sonic flow during steady-state conditions.

7.5.5.2.12   Emergency Helium Recovery

In the event of an unexpected or intentional shutdown of the main cryogenic systems, all the LHe in the main dewars, transfer lines, and the main SRF modules will be recovered to the gaseous storage tanks by the recovery compressors' control system.

All SRF modules must be protected against over-pressurization. The cryogenic system will receive a fail-safe signal to initiate securing the SRF modules as follows.

- The helium level/control feed valves in the cryogenic distribution valve box for the SRF modules are turned off.
- The DC heaters in the helium vessel of the SRF modules are turned off.
- The RF power to the SRF modules is turned off.
- The intercept flow valves are turned off.
- The DC heaters in the main LHe dewars are turned off.

7.5.5.2.13   Emergency Power

Cryogenic systems are susceptible to damage from abrupt power losses. Loss of electrical power, for example, could cause an unexpected system shutdown, which would require continuous operation of the recovery compressor to recover generated boiled-off GHe to the helium storage tanks. The recovery compressor, main helium dewars, cryogenic distribution valve box, and the cryogenic electronics of the SRF modules require a sufficient source of emergency power, as does the Oxygen Deficiency Monitoring systems, which must have an Uninterruptible Power Supply system.

7.5.5.2.14   Utilities Requirements

All utilities requirements for individual cryogenic components such as power, current and voltage, water cooling, instrument air, and so forth have been listed in Table 7.5.7.

7.5.5.2.15   Helium Transfer Lines

Single- or multi-channel transfer lines may be used to transfer liquid or GHe to various components such as to/from the main LHe dewar, SRF distribution valve box, or SRF module. There are three different helium gas lines:

- one suction line to transfer low-pressure helium gas from SRF modules (waveguides), valve boxes, the main dewar (in case of relief or burst), and the refrigerators/liquefier to the main compressors

- one discharge line to transfer high-pressure helium gas from the main/recovery compressors to oil removals, to the refrigerators/liquefiers, cold box, and gaseous storage tanks
- one makeup/recovery line between suction/discharge of the compressors and GHe storage tanks

All these lines will be capable of handling the individual required gas flow rate within specified pressure drops, as will be determined during the design stage. The pressure drops for each line correspond to the line geometry and flow conditions and will be calculated as required during the design phase.

The geometric design of these lines will be dictated by pressure drop, state, and flow-rate requirements. The length, outer diameter, inner diameter, and wall thicknesses will be selected to satisfy the design requirements (flow rate, pressures, heat leak, and safety). Seamless, high-quality 316L stainless steel tube will be used to construct the inner and outer sections. The use of copper tubing to carry LN2 for cooling radiation shields will be permitted provided the design conforms to all applicable codes.

Single- and multi-channel lines may be used to transfer LHe between various cryogenic components. These vacuum-jacketed lines are also to be made from high-quality seamless stainless steel tubing. The lines and mating connections of the SCL or MCL will be constructed to have minimum heat leak, will resist damage from thermal expansion and contraction, and will utilize smooth, seamless, low-pressure drop construction.

7.5.5.2.16   Nitrogen Transfer Lines

The LN2 lines will transfer the LN2 from the nitrogen storage tank to various components. There will be different sizes to transfer appropriate flow rate among inter-connecting components. The main line from the LN2 tank to the phase separator and then to the LN2 distribution manifold will be capable of handing a LN2 flow rate of 200 l/hr at <.5 bar pressure drop. The heat loss of the LN2 lines will be specified to have less than 0.5 watt/m at 80K (exclusive of valves and bayonets). All LN2 transfer lines will be the vacuum-jacketed type, and made of seamless stainless steel. The inner lines will be provided with flexible sections to compensate for thermal expansion and contraction.

Suitable keep-full valves will be installed along the fixed lines to ensure single-phase liquid flow to designated components when pressure stability is essential (e.g., SRF modules). The insulating vacuum space of the lines will take into account the relative humidity factor, dew point, and seasonal temperature variations to ensure it is condensation-free at all times. In addition to combined pump-out/burst ports, the line will have pressure and temperature transmitters with digital or analog output signals for monitoring and interlock.

7.5.5.2.17   LN2 Storage Tank, LN2 Phase Separator

An 84,000 L bulk LN2 storage dewar located outside the storage ring will supply LN2 as needed to the helium cryogenic system, as well as to the Liquid Nitrogen Distribution System. The estimated average withdrawal of ~400 L/hr will use 11% of the stored liquid daily. Based on this estimated rate of consumption, the nitrogen tank must be refilled at least twice weekly for an uninterrupted supply of the LN2 to the cryogenic system. Installation of wireless telemetry will ensure an adequate supply of LN2 by the LN2 supplier. This device will provide remote information of the current liquid level and tank's pressure to the central control system. A minimum of two LN2 withdrawals will be specified, one for direct supply to the cryogenic room and one for supply to vaporizers supplying GN2 to the cryogenic room instrumentation. A gas vent line will be installed to vent gas to the outside buildings. Redundant safety devices, such as relief valves, rupture disks, and various sensing devices will ensure maximum operational safety. Incorporating the use of a vertical fin pressure building system will reduce frost and ice buildup.

The supply pressure to the SRF cavities and the refrigerator pre-cooler will fluctuate, due to uneven withdrawal, and also when the tank is being refilled by the delivery truck. Operating pressure of the SRF cavities and the refrigerators' pre-cooler efficiency will be compromised during such conditions. Therefore, a

sufficiently large phase separator (necessary due to the large flow rates) will ensure steady pressure to each SRF cavity, the refrigerators, distribution valve boxes, and transfer line heat shields.

Table 7.5.7   Cryogenic System Utilities Requirements.

Item, (Qty)	Location	Power	Water Needs	Compressed Air	Ventilating Air	Reference
Main compressors and the oil removal systems (2)	Comp. Room	265 kW, 3phase, 60 Hz, 400 VAC, 450 A (Peak Current), interruptible	Chilled: 28 m³/h, Ti=15C, ΔT=15 CPi (max) = 7barg, ΔP=2.5bar	21 m³/h	10,000 m3/h	AL
Recovery compressor and the oil removal system (1)	Comp. Room	43 kW , 3 phase, 60 Hz, 400 UPS -VAC, , 20A nominal intensity at 0 load, 64 A nominal intensity at full load. no interruption	Chilled: 4 m³/h	2 m³ /h		NSRRC, AL
Refrigerator (1)	Cryo Room	10 kW, 60 Hz, 230 UPS - VAC, interruptible	Deionized: 170 L/h Ti=20-30°C, ΔT=10°C, Pi (min-max) = 3-7 barg	10 m³/h		NSRRC, AL
LHe dewar (1)	Cryo Room	1kW, 110 VAC (Heaters)	-		-	
RF valve Box (1)	Tunnel Roof	TBD	-	50 m³ / hr		NSRRC
Multi-channel transfer lines (As required)	Cryo Room	TBD	-	50 m³/h		
Monitor system and vacuum pump for cryogenic plant (1)	Cryo Room	40 A, 3 phase, 480 volt, no interruption 40 A, 3 phase, 380 volt, interruptible	-	-		NSRRC
Dryer for He purifier system (1)		12 kW, 1 phase, 220 volt, no interruptible	-	4 m³/h		NSRRC
LN2 phase separator (1)	Near Cryo Room	110 VAC – 60 Hz, 5 A	-	Small amount	-	-

7.5.5.2.18   Cryogenic System Layout

A flow schematic of the cryogenic system is shown in Figure 7.5.7. The two 500 MHz (fundamental) and one double-cell 1500 MHz (harmonic) SRF modules will occupy a single straight section. A designated space in the neighboring straight section is planned for an additional 500 MHz SRF module to be installed later. These two neighboring straight sections were located near the linac and most of the NSLS-II offices, where the fewest beamlines are located.

Currently we envision four rooms dedicated to the RF power supplies and cryogenic systems. These rooms will be adjacent to the RF straight sections, minimizing the waveguide length and heat load from the helium transfer lines between the cryogenic room and SRF modules. Two power supply rooms are directly adjacent to each RF straight section. The cryogenic room is deliberately placed almost at equal distance from each straight section, between the power supply rooms. Another room adjacent to the cryogenic and power supply rooms is planned for testing SRF modules prior to installation, troubleshooting, and for R&D purposes. The compressor room and gas management buffer tanks have been separated and placed farther from the main building, to isolate induced vibration and noise.

The cryogenic room houses the refrigerator, LHe dewar, inter-connecting transfer lines, multi-channel distributing manifolds, and local control system. The adjacent RF test room is dedicated for pre-installation testing and R&D purposes.

7.5.5.2.19   Oxygen Deficiency Hazard Monitoring and Control System

Oxygen Deficiency Hazards are present when atmospheric oxygen content falls below 19.5% by volume. The BNL Standard Based Management System has strict guidelines in compliance with the Occupational Safety and Health Administration Respiratory Protection Standard 29CRF1910.134 (see Table 7.5.8).

The main potential sources of reduced oxygen are from unplanned discharge of cryogens into confined spaces. Liquefied gases such as helium and nitrogen have the potential to cause ODH conditions, since expanded gases can displace air rapidly when released to the atmosphere.

For NSLS-II, a complete ODH analysis is required for each area (tunnel, cryogenic room, and compressor room), for all possible scenarios, in order to plan and put appropriate controls and measures in place. For the purpose of this report, an ODH classification of 1 is assumed, which among several requirements mandates the implementation of personal oxygen monitoring systems.

Table 7.5.8   ODH Control Measures.

	ODH Class				
Environmental Controls	**0**	**1**	**2**	**3**	**4**
1. Warning signs	■	■	■	■	■
2. Ventilation			■	■	■
ODH-Qualified Personnel Controls					
3. Medical approval as ODH-qualified		■	■	■	■
4. ODH training	■	■	■	■	■
5. Personal oxygen monitor		■	■	■	■
6. Self-rescue supplied atmosphere respirator		■	■	■	
7. Multiple personnel in communication			■		
8. Unexposed observer				■	■
9. Self-contained breathing apparatus					■

Multi-channel gas monitoring systems, such as Safe T Net 410 (up to four channels), have been considered for installation in each area. These microprocessor-based controllers are designed to accept up to four combustible oxygen transmitters. Features include digital readout display, LED alarm indication, 4 to 20 mA output, individual low and high alarm, and relay signals for interlock purposes.

7.5.5.3   Preventive Maintenance Programs

The overall availability of the cryogenic system is defined as the ratio of the actual delivery time to the scheduled operating time. Synchrotron light source facilities are normally operated continuously, 24 hours per day, seven days a week, excluding short studies or maintenance periods and one or two extended periods of machine maintenance per year when the facility is shut down for preventative maintenance, upgrades, and repairs. This is necessary to decrease the number of unscheduled breakdowns. Routine preventive maintenance must therefore be conducted according to manufacturers' recommendations, and, for in-house designed equipment, from past operational experience and engineering judgment.

In some cases, vendors' input via remote monitoring systems may be required. Remote monitoring and storage of data may enable technicians to intervene and troubleshoot problems before complete breakdown occurs. The nature and extent of this capability will be defined during the system design phase.

7.5.5.4   Electrical Design and Power Supplies

The cryogenic system for the RF cavities will include power supplies as required; however, prime power is needed for the cryogenic system components such as the refrigerators, liquefiers, diagnostics, controls, etc. For personnel safety systems such as the ODH system, uninterruptible electrical power is also required.

Prime power inputs required for the cryogenic system will be specified as 115 V, 60 Hz AC, 208 V or 230 V 60 Hz AC, and 480 V 60 Hz AC. Electrical wiring and electrical components will be installed according to BNL, NFPA, and OSHA specifications. Wiring and schematics will be developed as needed for documentation and troubleshooting purposes. As applicable, electrical components will be purchased that are NRTL approved.

7.5.5.5   Control System

Process control systems will be driven by PLCs. The process logic architecture is depicted in Figure 7.5.8 (next page). The main PLC controls the entire helium liquefaction system. This PLC can communicate to a flat screen and is capable of providing an alarm, shutdown protection, local display, and other specified control functions. The compressor's PLC will transmit the specified signals to the main control panel, located at the liquefiers via a digital data interface. The compressor's control panels are to be furnished with a remote/local key switch to transfer starting capabilities between the compressor's panel and the main control panels. The CPUs, RAM, interface boards, power supply, and other components will be defined later.

The overall logic control architecture will be defined during the detail design stage when all control functions will be integrated and communicated to the machine control system.

References

[7.5.1]   W. Brauns, www.gdfidl.de
[7.5.2]   K. Halbach and R. F. Holsinger, "SUPERFISH - A Computer Program for Evaluation of RF Cavities with Cylindrical Symmetry," Particle Accelerators **7** (1976) 213-222.
[7.5.3]   D. Myakishev, "CLANS2 - A Code for Calculation of Multipole Modes in Axisymmetric Cavities with Absorber Ferrites," Proceedings of the 1999 Particle Accelerator Conference, NYC.
[7.5.4]   R. A. Rimmer et al., "An RF Cavity for the NLC Damping Rings," Proceedings of the 2001 Particle Accelerator Conference.
[7.5.5]   S. Mitsunobu et al., "Status and Development of Superconducting Cavity for KEK-B," Proceedings of the 1997 Particle Accelerator Conference.
[7.5.6]   J. Kirchgessner, Part. Accel. 46(1):151 1995.
[7.5.7]   K.W. Robinson, CEAL-1010, Cambridge Electron Accelerator, Cambridge, MA (1964).
[7.5.8]   Y. Miyahara et al., "Equilibrium Phase Instability in the Double RF System for Landau Damping," NIM A-260 (1987 p 518-528.
[7.5.9]   R.A. Bosch et al., "Robinson Instabilities with a Higher-Harmonic Cavity," Phys Rev ST-AB **4**, p. 74401 (2001).
[7.5.10]   M. de Jong et al., J. Microwave Power Electromagnetic Energy, **27**:136-142, 1992.
[7.5.11]   M. Jensen et al., "First Results of the IOT Based 300 kW 500 MHz amplifier for the Diamond Light Source," PAC 2005, Knoxville, TN.
[7.5.12]   F. Perez et al., "New Developments for the RF System of the ALBA Storage Ring", EPAC 2006, Edinburgh, Scotland.
[7.5.13]   P. Marchand, et al., "High Power (35 kW and 190 kW) 352 MHz Solid State Amplifiers for the SOLEIL Synchrotron," PAC 2005, Knoxville, TN.
[7.5.14]   Hanspeter Vogel, ACCEL. Private communication.

[7.5.15] M. Svandrlik, et al., "The Super-3HC Project: An Idle Superconducting Harmonic Cavity for Bunch Length
          Manipulation," EPAC 2000.
[7.5.16] S. Simrock, "Digital Low-Level RF Controls for the Future Superconducting Linear Colliders," PAC 2005,
          Knoxville, TN.
[7.5.17] C.W. Horrabin, and D.M. Dykes, "Diamond Low Power RF System," EPAC 96.
[7.5.18] J.M. Brennan et al., "RHIC RF beam control," EPAC-2001.
[7.5.19] M. Liepe, S. Belomestnykh, et al., "A New Digital Control System for CESR-C and the Cornell ERL," PAC
          2003, Portland, OR.
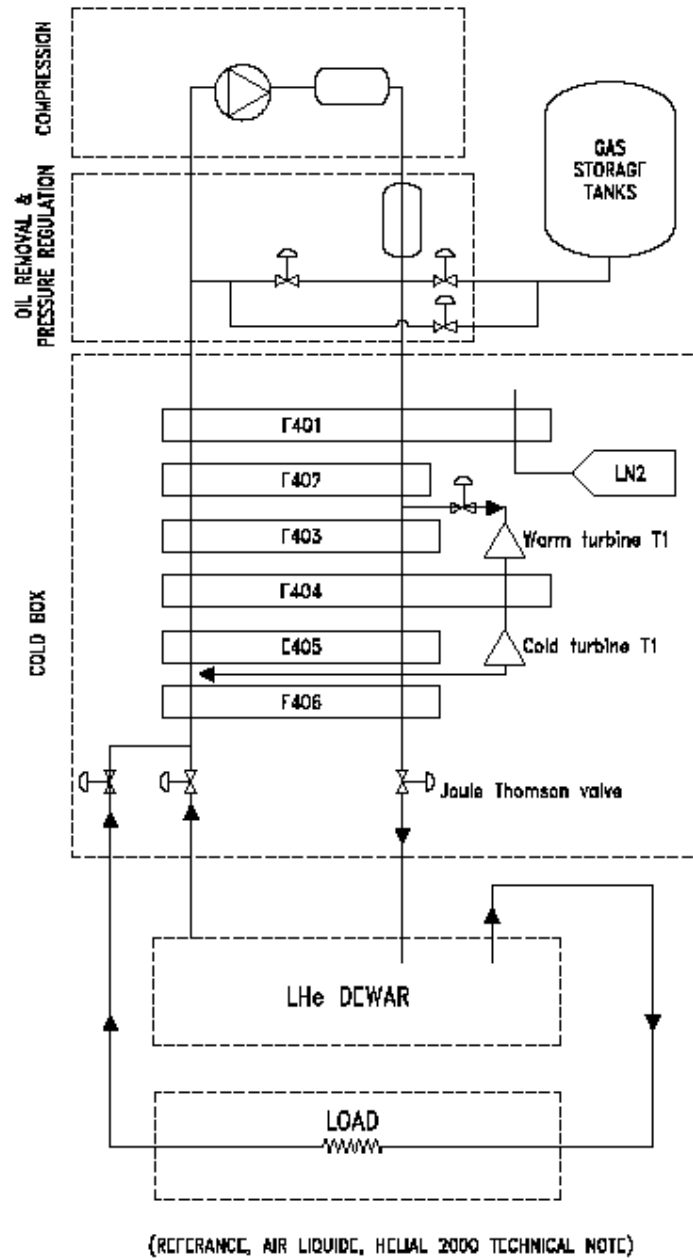
Figure 7.5.8   Cold box, simplified flow diagram.

7.6   Injection System

To minimize disruption to operations, the full-energy injection system will run most of the time in top-off mode. It will also be capable of filling the ring from empty to full charge in a reasonable time.

The injection system consists of a 200 MeV linac, followed by a booster housed in the main ring tunnel and hung from the ceiling above the main synchrotron, as described in Chapter 6. The capability to increase the injector linac energy is built into the design. The large circumference of the booster (780 m) makes injection and extraction a relatively simple operation, due to the long revolution periods (>2.5 μsec) of both the booster and the main ring, at least as far as rise times and fall times of the pulsed magnetic components are concerned.

7.6.1   Injection Sequence

The injection process to fill the ring from zero current occurs at the rate of 1 Hz, and bunches are transferred to the main ring nominally 40 at a time (this number can easily be increased to 100 or more bunches) to fill consecutive about 1,040 of the 1,300 RF buckets available. Bunch groups enter the ring in sequence, starting with the front of the ring train and stepping sequentially back in time along the filled ring bunch train until the end is reached, then skipping over the empty section and starting again at the head of the bunch train, until the required current has been established. Assuming the same amount of charge (7 nC per macropulse) as for the top-off mode, the duration of the initial fill is about 3 minutes with the injection system running at a 1 Hz repetition rate. This value is sufficiently low; therefore, there are no additional requirements for the injection system in terms of the initial fill.

Top-off operation to keep the current within ±0.5% of the nominal value will be the standard operating mode of NSLS-II. The frequency of operation to keep the current within these boundaries depends on the beam lifetime and is expected to take place about once per minute. The injected bunch trains from the booster (nominally 40 buckets), are stepped sequentially around the ring bunch structure. Users expect bunches to stay relatively constant in charge relative to each other (a difference of ±10% has been adopted). We are considering several possible techniques for providing a filling pattern with sufficient uniformity.

7.6.2   Ring Injection Scope

The entire ring injection system consists of four distinct component assemblies: 1) linac and electron gun, 2) beam transport line, 3) the booster, discussed in Chapter 5, and 4) the booster-to-storage ring transfer system. Three of these assemblies are briefly discussed below.

7.6.2.1   Linac and Electron Gun

The first component of the ring injection system is the linear accelerator (linac), including the electron gun, which is a grid-controlled dispenser cathode running at -100 kV, capable of peak pulse currents of up to 1.5 A. The low-energy beam transport system that brings the gun current from the gun to the linac includes four or more focusing solenoids, a subharmonic buncher cavity that imposes the ring/booster RF structure (~500 MHz) on the drifting beam, and a pre-buncher cavity that imposes the linac RF structure (~3000 MHz) on the 500 MHz bunches. At least two fast beam current monitors must be included here, to be able to detect the bunching of the beam at both frequencies before injection into the linac. The gun pulse will nominally be 80 nsec long, supplying 40 buckets of ring charge at 500 MHz.

The linac itself comprises four 2/3π traveling wave iris-loaded waveguide accelerating sections, each driven at 3000 MHz by a single 35 MW peak power non-sledded klystron fed by its associated modulator. The linac output energy is very conservatively rated at 200 MeV, with the typical energy spread from an S-

band linac of ±0.5%. The linac also requires at least four X–Y steering coils, their power supplies, and beam position monitors. It is described in more detail in Chapter 5.

7.6.2.2   Booster-to-Storage Ring Transfer System

The fourth component is the booster-to-storage ring transfer system, which includes the extraction system, the transport line to the ring, and the injection straight in the storage ring. The transport lines need to match the Twiss parameters of the linac or booster beam to the booster or ring acceptance at the injection point. The trajectory of the electron beam gets matched to the storage ring injection straight by four bending magnets. Matching of the machine functions is accomplished with 17 quadrupoles. These transport lines, along with the appropriate numbers of beam current and position monitors and X–Y steering magnets, are described in more detail in Chapter 6.

A long, strong-pulsed magnet close to the circulating beam can perturb the orbit of the circulating beam significantly. To minimize this effect, we keep this magnet as short as possible and construct it as a straight eddy current-shielded type. We will use a second pulsed magnet upstream of the final septum; this will be a longer, higher-field pulsed magnet, farther away from the storage ring beam and constructed of thin silicon steel laminations arranged in a curve following the injected electron beam trajectory. This magnet provides most of the final bend of the transport line. Optimization of these two magnets is still in progress. The injection straight section (Figure 7.6.1) is an 8 m dispersion-free straight in the storage ring containing the entire injection bump. The ring injection hardware consists of 1) a pre-septum with end-field compensated, 750 mm laminated, steel-pulsed dipole (Table 7.6.1) 2), a final eddy current channel shielded septum magnet that is 500 mm long (Table 7.6.1), and 3) four injection kickers that are 750 mm long, (Table 7.6.2).

We are assuming 1) a space between the last ring component and the first kicker at the upstream end of the injection straight, 2) a spacing center-to-center of the first and second kickers to achieve a beam displacement of 15 mm, and 3) a mirror image of the kicker spacing at the downstream end of the ring straight section. This will leave a 3.6 m space, which is enough room for the proposed injection septum configuration, allowing the injection process in horizontal phase space to be achieved (Figure 7.6.1). The final injection septum at the end of the transport line will bend the beam coming from the transport line into a trajectory parallel to the displaced coasting beam in the ring.
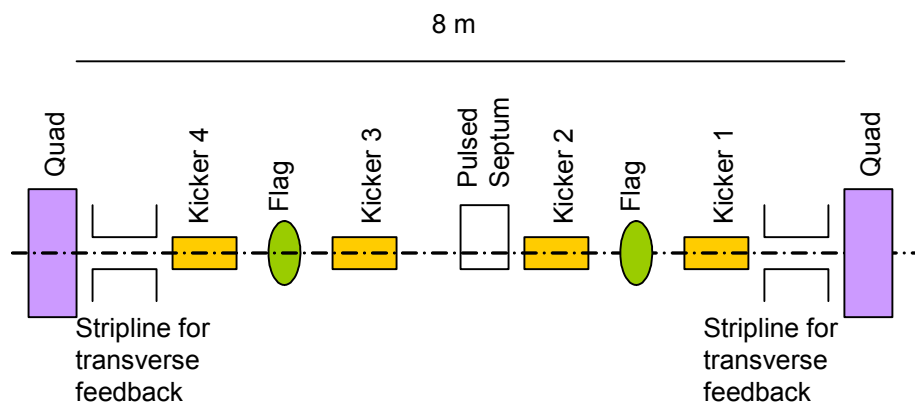

Figure 7.6.1   Arrangement of the injection straight section.

Table 7.6.1   Parameters of the Septum Magnets.

Pre-septum magnet	
Field [T]	1.1
Length[m]	0.75
Angle [mrad]	83
Aperture, H xV [mm]	20 x10
Current Amplitude[kA]	12
Inductance[µH]	1.8
Voltage [V]	600
Pulse shape	100 µsec ½ sine wave
Design	10 mil silicon steel laminations
Final injection septum magnet	
Field [T]	0.9
Length [m]	0.5
Angle [mrad]	45
Aperture, H xV [mm]	20 x10
Current amplitude [kA]	10
Inductance [µH]	1.2
Voltage [V]	600
Injected pulse shape	60 µsec period, full sine wave
Design	Ferrite EBG V270-035A

The ring injection kickers will be run in series from a single capacitor bank and are connected together by low-impedance transmission lines. Experience at NSLS has shown that the insertion impedance of well-constructed transmission lines is insignificant. In this way, with some tuning, the disturbance to the stored beam due to the injection process can be minimized, as any slight mismatch and field jitter are common to all four pulsed magnets.

Table 7.6.2   Parameters of the Injection Kickers.

Ring injection kickers [number)	4
Field [T]	0.193
Length [m]	0.75
Angle [mrad]	14.4
Aperture, H xV [mm]	70 x25
Current Amplitude [kA]	5.34
Inductance [µH]	1.3
Voltage [V]	4,500
Temporal pulse shape	5 µsec at the base, ½ -sine wave
Design	Ferrite CMD 5005

Special attention will be paid to minimizing the disturbance of the stored beam orbit from transients induced by the pulsed magnets. Alternative arrangements of the injection straight section will receive attention in our future studies. Namely, using the Lambertson injection septum with the transport line descending vertically may provide substantial benefits. The Lambertson septum magnet is fed by a DC, not pulsed, power supply, which eliminates a major component of the disturbance for the stored beam orbit. Requirements on the ring dynamic aperture for this injection scheme will be carefully examined.

7.6.3   Injection Simulations

Given the injection straight set-up, we performed simulations of the injected beam dynamics. These studies indicate the design is feasible. To quantify requirements for the injector, three values of the injected beam emittance were used for tracking the electron bunch through the NSLS-II lattice. Initial efforts included modeling the injection process using ELEGANT and determining the ring stay-clear aperture required for injection using TRACY-2. Both of these studies are discussed below. Future work will include calculating tolerances for the injected bunch and estimating the loss budget and loss patterns.

7.6.3.1   Phase Space of the Injected Beam

To determine the minimum acceptance required by the injection process, we simulated the electron distribution in x, x′ phase space after the injection, using the particle-tracking code ELEGANT. In Figure 7.6.2 we plot the result for three different cases of the injected beam with emittance 10, 50, and 100 nm, respectively (Table 7.6.3). For each case, the beta function and injection offset are optimized to reduce the required acceptance. The plot gives the electron distribution for the first five turns indicated by the five colors, as shown by the key. Note that when the emittance increases to 100 nm, as the betatron oscillation amplitude increases, the tune is approaching 0.33; hence, the fourth-turn distribution almost overlaps with the first turn. The horizontal maximum increases from 7 mm to ~10 mm, while the maximum x′ increases from 0.35 mrad to ~0.5 mrad. This simulation showed that storage ring acceptance is adequate for injection of the beam with emittance up to 100 nm. This tracking was done for the bare lattice without RF, synchrotron radiation, or errors. Including those additional effects will be the subject for future work.
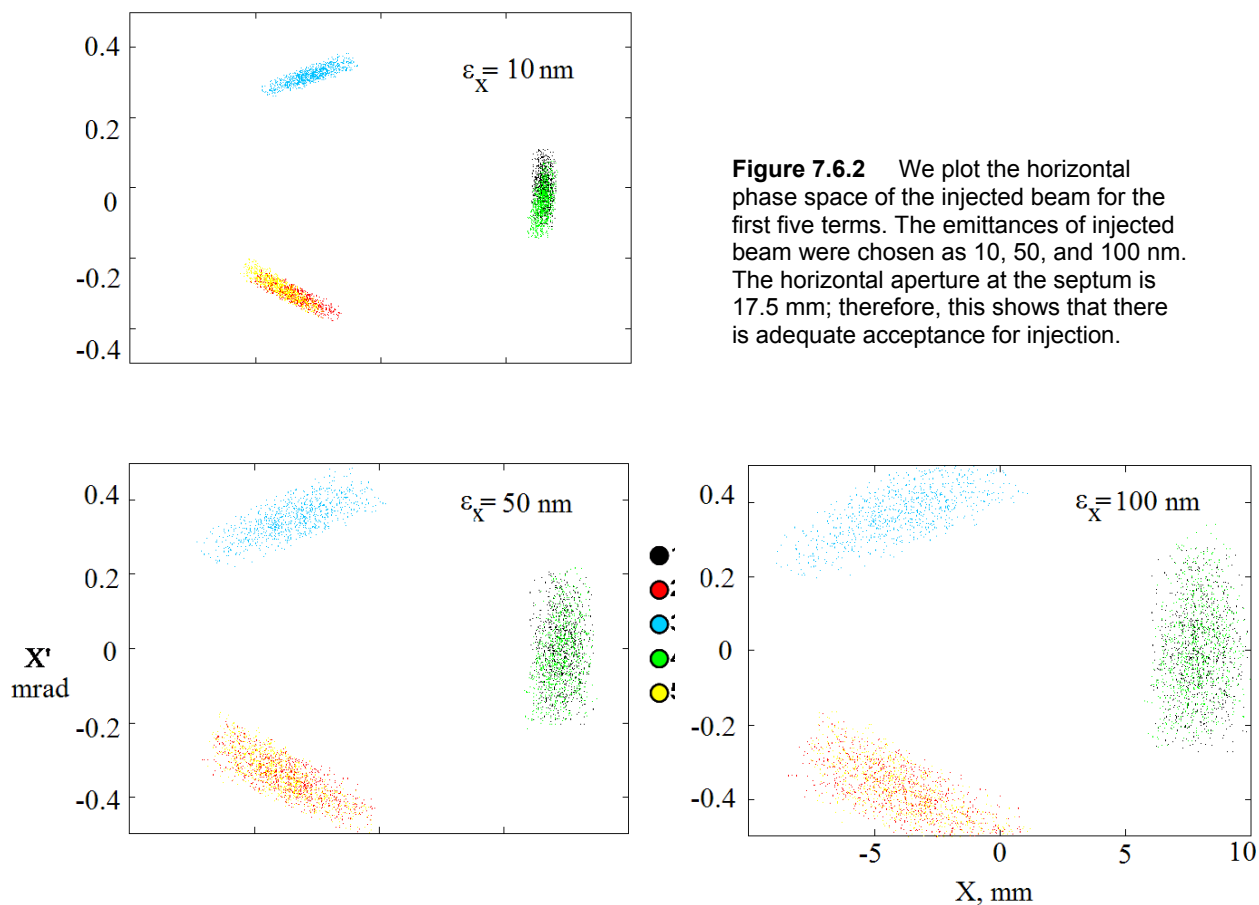
Figure 7.6.2   We plot the horizontal phase space of the injected beam for the first five terms. The emittances of injected beam were chosen as 10, 50, and 100 nm. The horizontal aperture at the septum is 17.5 mm; therefore, this shows that there is adequate acceptance for injection.

Table 7.6.3 Input Beam Parameters. Injected beam is matched to provide minimum stay clear aperture for each value of emittance. ∆E/E = 0.05% in all cases, vertical beam size calculated with coupling κ = 0.1.

Horizontal emittance (nm-rad)	Initial displacement from stored beam (mm)	3x RMS horizontal beam size (mm)	3x RMS horizontal beam divergence (mrad)
10	6.5	0.62	0.15
50	7.3	1.65	0.27
100	7.9	2.47	0.36

7.6.3.2   Stay-Clear Aperture Required for Injection

Tracking results from InjTrack, a TRACY-2 module for tracking the injected beam at NSLS-II, are presented here. After correcting for errors, we will use the results to define the minimum aperture NSLS-II requires for injection.

The results are tracked with radiation and RF cavity off for the entire lattice, and then the maximum of beam envelope for each cell is plotted in Figures 7.6.3 (H) and 7.6.4 (V). The upper and lower curves correspond to the 17.5 mm septum aperture projected around the ring with $\sqrt{\beta_x(s)/\beta_x^{sept}}$. This is repeated for the vertical plane using the insertion device half-gap of 2.5 mm. Three curves represent required stay-clear aperture for tracking beam with the three emittances of 10, 50, and 100 nm. Results show that our design has sufficient physical aperture for injection. In the future, we plan to extend this analysis by tracking with errors, synchrotron motion, and radiation damping.
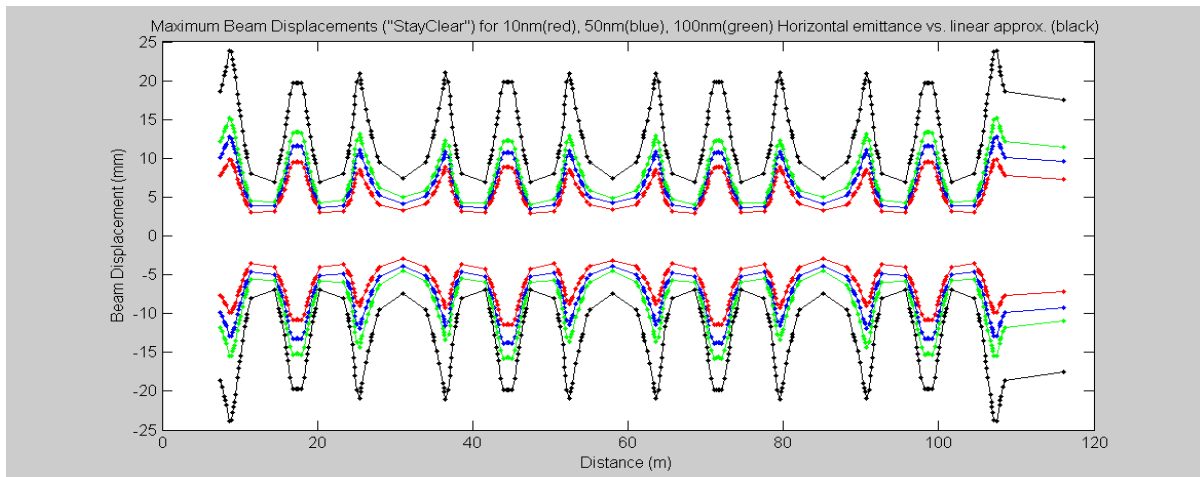
Figure 7.6.3   Beam (H) is injected at an initial displacement of ~17.5 mm (septum location).
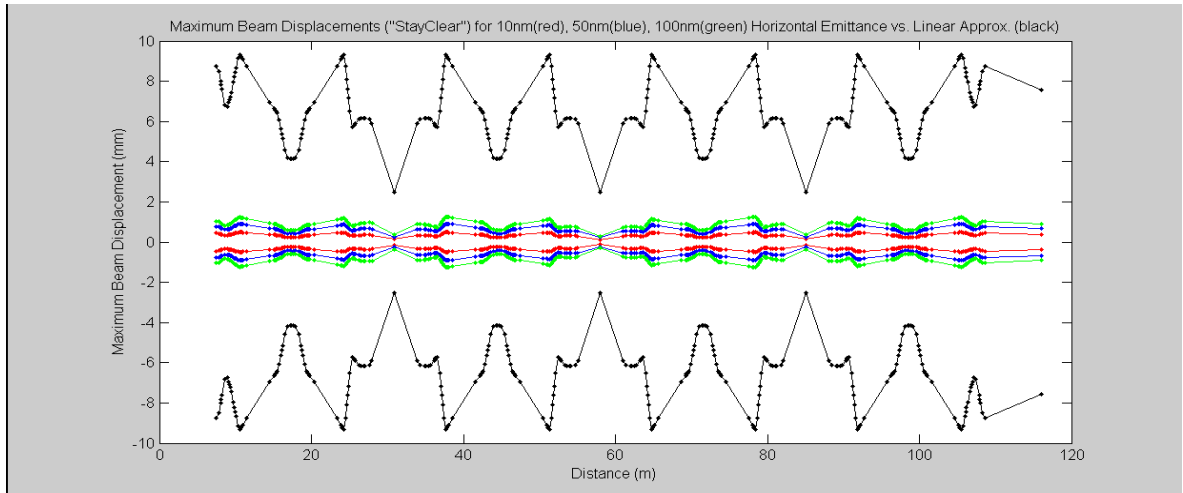
Figure 7.6.4   Injected beam envelope (V). Physical aperture at ID half-gap of 2.5 mm.

Reference

[7.6.1]   B. Kalantari, V. Schlott, T. Korhonen, Proc. of EPAC-2004, Lucerne, Switzerland, p. 2882.

7.7   Beam Scrapers and Photon Absorbers

7.7.1   Beam Scrapers

Two pairs of electron beam scrapers will be used for accelerator physics measurements of the aperture and beam lifetime limits. The thickness must be $\sim 5 X_o$ (radiation lengths) for the electron beam. The horizontal blades must be in the same plane and adjustable from full open (vacuum chamber width) to the chamber centerline with a resolution of ~ 1 μm and a reproducibility of ~ 5 μm. One location for the horizontal scrapers is in one of the dispersion regions next to the BPM and the SF2 sextupole, where there is high β_x and dispersion. The second location for horizontal scrapers is in the SID between the Q33 and S22 sextupoles, the maximum β_x for the ring. The two vertical scrapers will be placed near the high β_y in the dispersion region (D5A at $\Delta\mu_y \sim \pi/2$ from the injection septum) and the LID (D4B at $\Delta\mu_y \sim 2\pi$ from the injection septum). These scrapers will provide controlled physical apertures to prevent large-amplitude particles (from the injector) from hitting the small-gap undulators, later in the ring. The scrapers will also provide defined apertures for understanding the dynamic aperture and lifetime in the ring.

7.7.1.1   Conceptual Design

To maximize their effectiveness as well as to simplify their engineering design, the two pairs of beam scrapers required will actually consist of four separate units: two horizontal and two vertical scrapers. These scrapers will serve as protective devices for the IDs. They will also be used as diagnostic tools during the commissioning phase and during machine studies.

Previous reports [7.7.1] have indicated that Touschek scattering is the dominant source of ID damage. Work done at APS has shown that scrapers should be located in a low-emittance lattice to effectively protect the IDs. This suggests that the horizontal scrapers should be installed where there is adequate dispersion at the scrapers as well as a large horizontal beta function. Touschek scattering presumably not only imparts a large energy deviation, but also induces large betatron oscillations for the scattered particles. A significant concern, however, is that the scrapers may compromise injection efficiency—or worst yet, may even produce more ID damage if the injected beam hits the scrapers, creating a shower that propagates to the IDs. To address this concern, we will carefully study the development work done at APS.

All four units planned for NSLS-II will share the same engineering design and be built identically—the horizontal and vertical scrapers differing only in the final mounting and installation. Each unit will have two jaws or blades that can move independently from one another, each being driven by precisely controlled stepping motors. The blades will be made of Glidcop, a dispersion-strengthened copper with excellent thermal and electrical properties at elevated temperatures. Each of the blade assemblies will have a water-cooling circuit to minimize thermal expansion of the blades when they are hit by the dipole radiation fan.

Furthermore, to minimize impedance problems, the shape of the blades will be determined by detailed numerical simulation. These studies are still in progress and the results are preliminary. Figures 7.7.1 and 7.7.2 show two views of the design of an existing scraper at APS. The NSLS-II scraper design will be based on this APS design, with appropriate modifications to match the chamber geometry. Figure 7.7.3 shows a preliminary layout of the possible NSLS-II scraper.

Each scraper unit will be mounted directly on the vacuum chamber and the adjustable blades can be repositioned remotely. Once they are in the desired position, however, they must stay in place within the required tolerance.
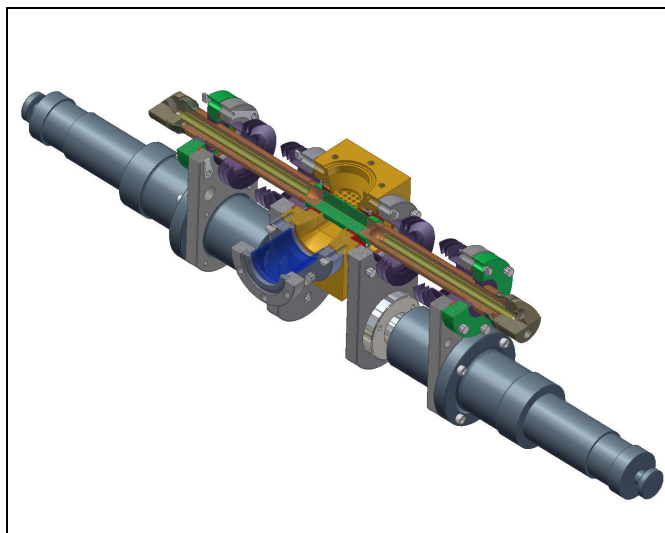
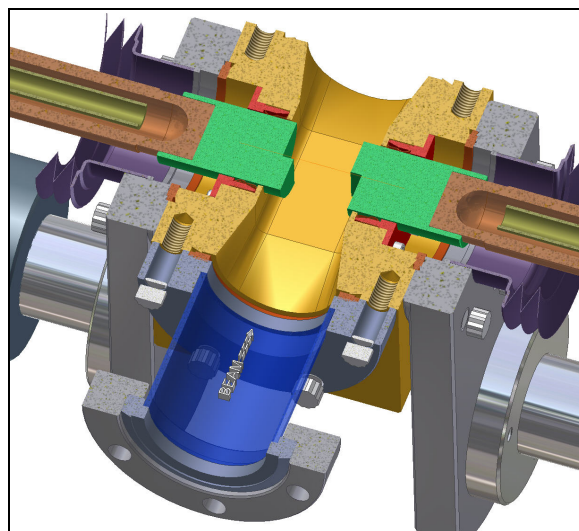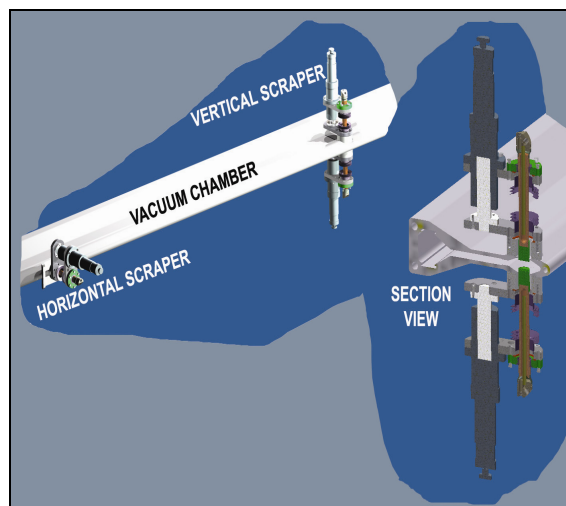**Figure 7.7.1**   (top left) Sectional view of APS scraper assembly, round blades (closed).

Figure 7.7.2   (top right) Sectional view of APS scraper assembly, blades partially opened.

Figure 7.7.3   (right) Conceptual layout of NSLS-II scraper (two views)

7.7.2   Photon Absorbers

Discrete photon absorbers will be installed in the vacuum chambers to protect their uncooled surfaces from the radiation fans of the bending magnets and IDs. Shielding the vacuum chambers from radiation fans also minimizes their thermal distortions and leads to better thermal stability of the PUEs attached to the chambers. To protect the chambers from exposure to unintentional beam deviations, PUE interlocks at insertion devices will be set at $\pm$ 0.25 mrad [7.7.2]. The positional error budgets consisting of orbit error, mechanical, and survey tolerances will be set at $\pm$2 mm.

As discussed in Chapter 8, the peak power densities of the bending magnets, damping wigglers, and cryogenic permanent magnet undulators are 0.088 kW/mrad^2, 55.30 kW/mrad^2, and 77.86 kW/mrad^2, respectively, for a 500 mA beam at 3 GeV. The power density of the BM is uniform in its horizontal fan of 104.7 mrad (6º) except at the edges. For the DW and CPMU devices, the horizontal power density profiles are shown in Figure 7.7.4. The vertical power density profile, common for all devices, is shown in Figure 7.7.5.

Horizontal Power Density Profile
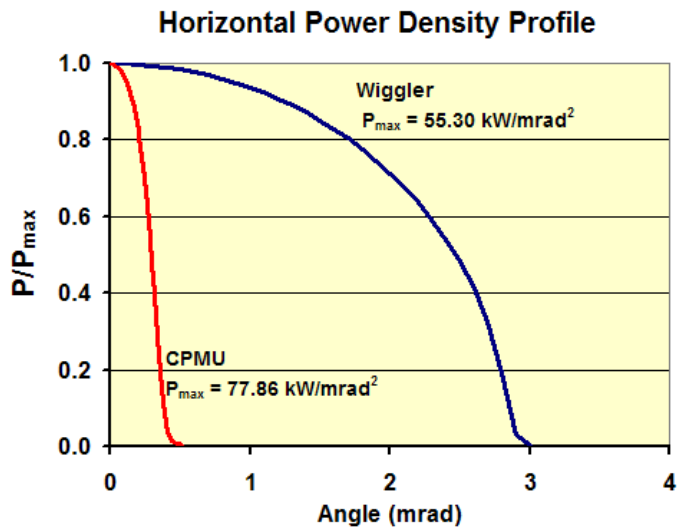
Figure 7.7.4 Horizontal power density profiles, P/P_{max}, of damping wiggler and CPMU. P_{max} is obtained at 500 mA beam current.

Vertical Power Density Profile
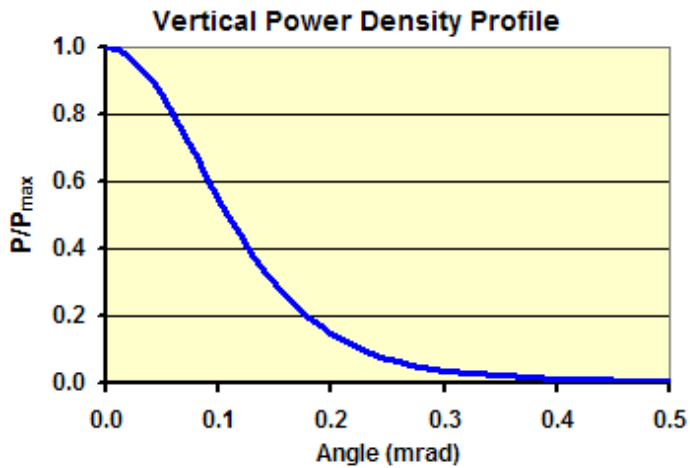
Figure 7.7.5 Vertical power density profile, P/P_{max} for damping wiggler and CPMU.

The CPMU radiation fan is narrow in both directions and can be extracted with adequate clearance through the 76 mm (H) × 25 mm (V) apertures of Chambers 1 and 2 and the 15 mm slot of Chamber 2 (see Figures 7.3.1 and 7.3.3). The BM and DW radiation fans in Chamber 2 (Figure 7.7.6), however, require clipping by two absorbers, namely, a crotch absorber and a wiggler absorber. Because of the high power density of the DW radiation, these absorbers clip the outer edges of the DW horizontal fan just enough to allow the clipped fan to be extracted to the front end.
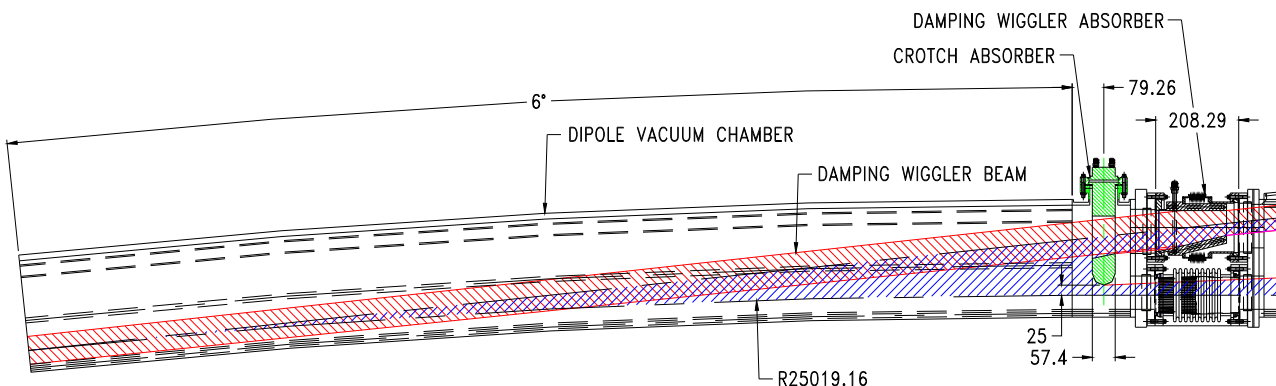
Figure 7.7.6 Clipping of BM and DW x-ray fans by crotch and wiggler absorbers in Chamber 2. The BM radiation fan (blue color) partially overlaps the DW radiation fan (red color).

7.7.2.1 Conceptual Designs of Photon Absorbers

Figure 7.7.7a shows a 3D model of the crotch absorber. The absorber is made from a Glidcop® block with brazed water-cooling channels of OFHC copper. Also brazed to the Glidcop block are a stainless-steel flange and a water manifold. A rectangular slot in the center of this block allows DW or CPMU radiation fans to pass through without interception (only the inboard edge of the DW fan is slightly clipped). The crotch absorber is inserted into the downstream aperture of Chamber 2 such that its nose tip is 5 mm inside the aperture (i.e., 30 mm outboard from the center of the aperture). The tip intercepts a total of 814 W of beam power with a maximum power density of 5.54 W/mm^2. A thermal analysis of the crotch absorber was carried out using ANSYS software. The results, plotted in Figure 7.7.7.2b, show a peak temperature of 102ºC, which is substantially lower than the maximum allowable temperature of 450ºC for Glidcop. OFHC copper would normally be used for a low temperature rise of ~100ºC. However, Glidcop will ensure the dimensional stability of the nose tip after brazing cycles and will allow a slight clipping of the inboard edge of the DW fan.
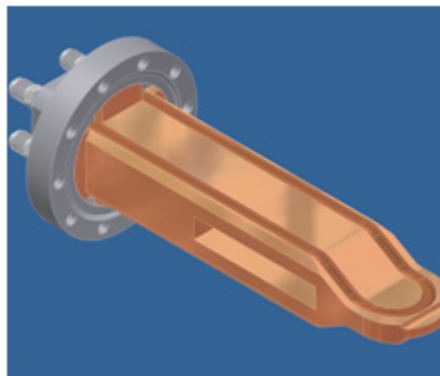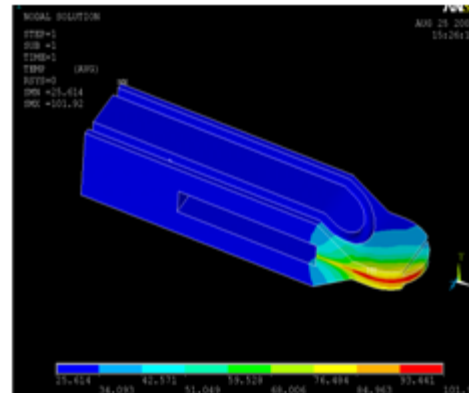

Figure 7.7.7 Crotch absorber.

a) 3D model.

b) Temperature contours from Ansys FE analysis showing a peak temperature of 102ºC.

The damping wiggler absorber, shown in Figure 7.7.8a, fits in the 208 mm space between Chambers 2 and 3 on the outboard side. The upstream end of the absorber is brazed to a flange that mates with the flange of Chamber 2. The downstream end is cantilevered inside a bellows assembly to allow for thermal expansions of the chambers during bakeout. Two water cooling channels are provided on each vertical side of the Glidcop block to absorb power from the outer extents of the horizontal DW x-ray fan at a grazing incidence of

6º. The total power intercepted by the two vertical sides is 11.6 kW, with a peak power density of 47.8 W/mm^2.

An ANSYS FE thermal analysis of the wiggler absorber predicted a peak surface temperature of 398ºC. The temperature profile, plotted in Figure 7.7.7b, shows high temperatures directly under the beam footprint.

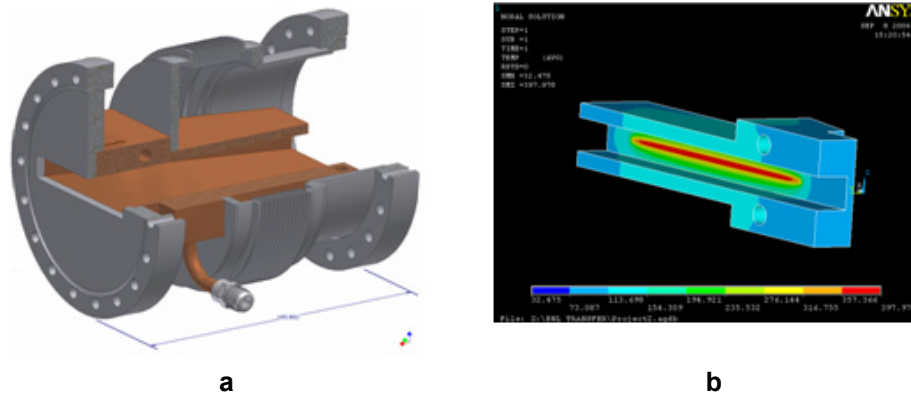Assuming a water flow of 2 GPM in each of the cooling channels, the average bulk water temperature rise will be 5.5ºC.

a   **b**

Figure 7.7.8   Damping wiggler absorber. **a**) Cut-out of a 3D model showing Glidcop block, cooling channels, bellows, and flanges. **b**) Temperature contours from an ANSYS FE analysis with a peak temperature of 398ºC.

Another crotch absorber will be used in Chamber 4 with a slot width that will allow the user-specified width of the dipole radiation fan to exit to the front end. Additionally, counter-flow and flange absorbers (Figure 7.7.9) will be used in Chambers 1, 3, and 5 to intercept unused dipole radiation fans.

Counter-Flow Absorber   **Flange Absorber**

Figure 7.7.9   Counter-flow and flange absorbers for the storage ring vacuum chambers.

References

[7.7.1]   Borland, M. "ID Protection with Fast-Moving Scrapers," OAG-TN-2004-050, November 11, 2004.
[7.7.2]   V. Ravindranath, S. Sharma, B. Rusthoven, M Gosz, L. Zhang, and J. Biasci, "Thermal Fatigue Life Prediction of Al-15," proceedings, MEDSI-2006 Workshop, SPring-8, Himeji, Japan, May 24-26, 2006.

7.8 Storage Ring Diagnostics and Instrumentation

7.8.1 Introduction

State-of-the-art advanced diagnostics and instrumentation systems are required for a smooth and rapid commissioning and for productive and successful operation of the NSLS-II storage ring. This section provides a list of the monitored parameters, technical solutions with some alternative variants, and the required specifications to achieve these goals. Table 7.8.1 shows a summary of these various instrumentation components.

Table 7.8.1   Beam Diagnostics and Instrumentation for Storage Ring.

Monitor	Quantity	Function
4-button pick-ups	226	Beam position, dispersion, response matrix, turn-by-turn dynamics
Stripline pick-ups	1	Longitudinal and transverse frequency components
RF-drive stripline and amplifier	1	Betatron tune
Loss monitors	10	Beam loss
Fluorescent flags	4	Injection position, profile
Transverse feedback system	1	Suppress beam instabilities
Optical ports for visible radiation	2	To provide light for streak camera, FireWire camera and emittance monitor
Streak-camera	1	Bunch length
DC current transformer	2	Beam current
Fast current transformer	2	Filling pattern
X and Y beam scrapers	2	Machine studies, halo
FireWire camera	1	Transverse beam characteristics
Emittance monitor	1	Transverse emittances
Diagnostics undulator	1	Energy spread, beam divergence, momentum compaction factor
Pinhole camera	1	Horizontal emittance
Counter	1	RF frequency monitor
Photon BPMs	2 per installed undulator	Photon beam angle and position

As a basic policy, whenever possible, we will pursue the utilization of commercial-off-the-shelf devices in order to reduce cost as well to achieve better reliability. Most of the existing diagnostics equipment today already satisfies the basic requirements for NSLS-II and only a few, if any, need further development.

Full utilization of the micron size electron beam requires sub-micron resolution of the orbit monitoring system, in order to provide the required position stability. Priority consideration will be given at the earliest stages of design to provide instruments for the detection and remedy of factors that affect beam quality.

7.8.2 Physics Design and Parameters

The following beam parameters will be monitored:

- closed orbit
- working point (tune for the both planes)
- circulating current and beam lifetime
- filling pattern
- emittance for both planes
- individual bunch length

- position of the photon beam for the insertion devices
- coherent bunch instabilities
- distribution of beam losses around the ring

During beam studies the following parameters will be measured:

- linear optics
- dispersion for both planes
- chromaticity for the both planes
- coupling
- momentum compaction
- energy spread
- beam based alignment of quadrupoles and sextupoles
- nonlinear resonances
- synchrotron frequency
- RF system parameters
- vacuum chamber impedances

7.8.3   Intercepting Diagnostics

Four flags will provide information on the shape and position of the injected beam and will assure proper matching of the injected beam. Two flags will be placed in the injection straight: the first one will be used to observe the incoming beam from the booster. The second flag, installed before the first kicker, will allow observation of the injected beam shape after one turn. The third flag will be installed after the first bend downstream of the injection straight. The fourth flag location will provide data on beam position and the beam approximately half a circumference away from the injection straight. The flag material will be cerium-doped yttrium aluminum garnet, which has excellent resolution (about 30 μm) and radiation stability [7.8.1]. The estimated horizontal beam size coming from the booster is $\sigma_x = 400$ μm, and vertical size for 2% coupling is $\sigma_y = 60$ μm. If the spatial resolution of the YAG:Ce flag is found inadequate, then optical transition radiation can be used.

To avoid impedance problems, the flag will be designed to ensure a smooth vacuum chamber wall when the screen is fully retracted. Spring-loaded RF-fingers will be used to provide electrical contact in order to avoid trapped modes for the wake fields. A typical flag assembly used at APS is shown in Figure 7.8.1, and the RF fingers are shown in Figure 7.8.2. To use this design we will need only to modify the vacuum chamber aperture to match the NSLS-II geometry.

Figure 7.8.1   Design of the flag used for the diagnostic of the electron beam injected into the storage ring.
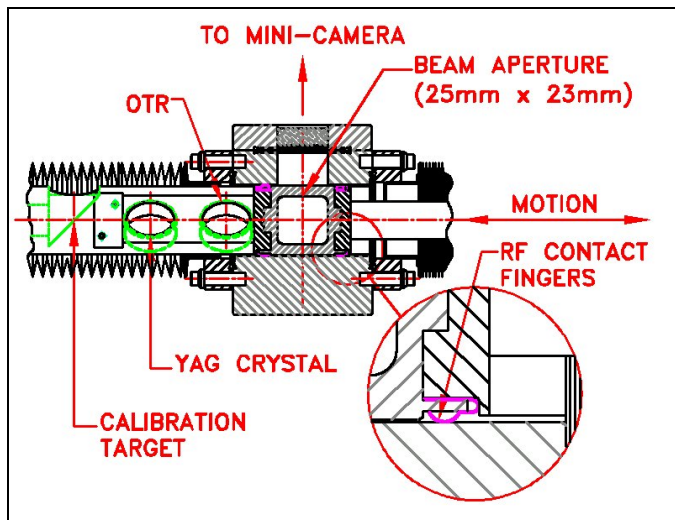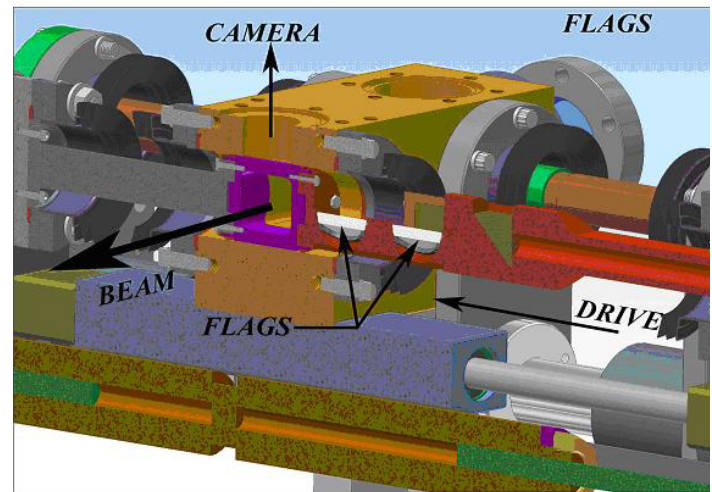

Figure 7.8.2   RF fingers (with detail), providing smoothness in the vacuum chamber.

7.8.4   Circulating Current

7.8.4.1   Filling Pattern Measurement

To maintain uniform fill and mitigate dependence of the BPM receivers on the filling pattern, two in-flange fast current transformers will measure the charge of individual bunches [7.8.2]. They have 1.75 GHz bandwidth with 200 ps rise time. The information obtained will be used in the top-off algorithm. The signal from the FCT will be used as input for top-off safety interlock. Figure 7.8.3 shows a typical in-flange fast current transformer that can be directly mounted on the beam chamber. An elliptical aperture, matching the shape of the storage ring vacuum chamber, will be used (Figure 7.8.4).

Figure 7.8.3
Bergoz In-Flange
Fast Current Transformer.
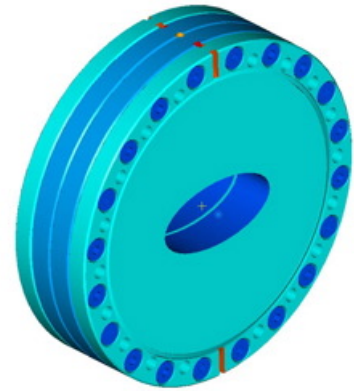
Figure 7.8.4
Elliptical aperture of the
in-flange current transformer
utilized at DESY.

7.8.4.2   DCCT

Two DC current transformers (PCT by Bergoz) will monitor the stored current, providing redundant measurement capability [7.8.2]. The Bergoz New Parametric Current Transformer (Figure 7.8.5) is the latest evolution of the Unser transformer, commonly known as DCCT, developed at CERN in 1966 by Klaus B. Unser.

DCCT has large dynamic range and high bandwidth, making it a versatile device for measuring lifetime and injection efficiency. It is insensitive to synchrotron revolution frequency and bunch fill pattern, with residual modulator ripple being eliminated, thus enabling full bandwidth operation down to a very low current.
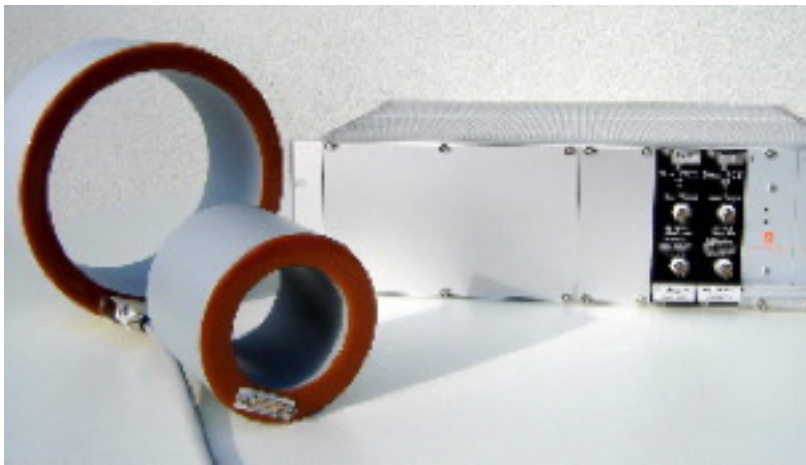
Figure 7.8.5   Bergoz New Parametric Current Transformer.

The NPCT-115-C30-H model has a radiation-hardened sensor and four ranges (± 20 mA, ± 200 mA, ± 2 A, ± 20 A) with remote control by TTL signals. Its resolution is better than 5 $\mu A/Hz^{1/2}$. We expect that the NPCT described previously will also be available as an in-flange unit.

7.8.5   RF Diagnostics

7.8.5.1   RF BPMs

The optics of the NSLS-II storage ring is shown in Figure 7.8.6. In the baseline design there will be seven BPMs for each cell. Straights with insertion devices, however, will be provided with two additional BPMs, shown in the figure as user BPMs.
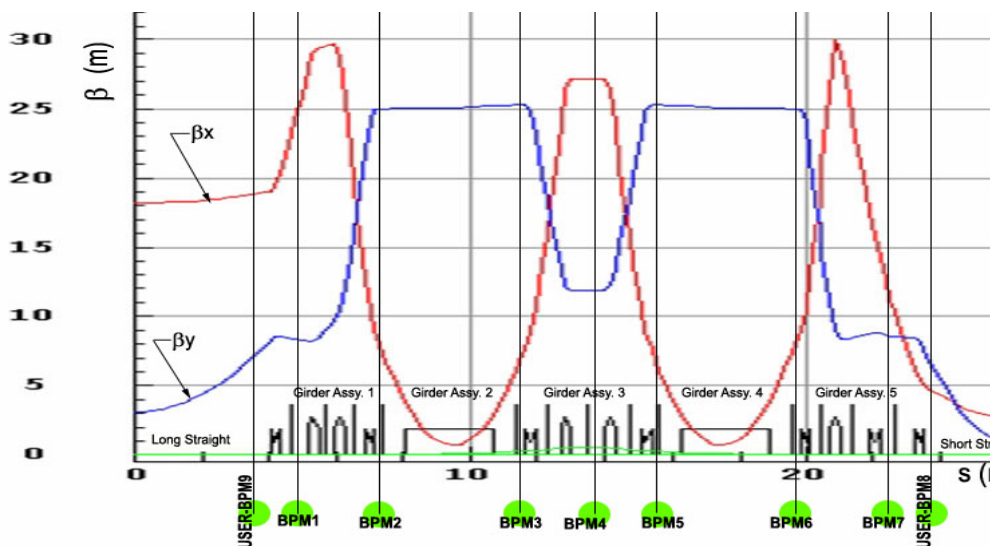
Figure 7.8.6 NSLS-II cell with BPM locations.

The high precision pick-up electrodes will utilize button design and will be diagonally incorporated into the aluminum extrusion vacuum chamber. Figure 7.8.7 shows the cross-section of the basic construction of the four-button pick-up electrodes. An average current of 500 mA circulating in the storage ring is expected to produce –1.1 dBm signal into 50 Ω load at 500 MHz. This estimate is done for a button, shown in Figure 7.8.8, with 5 mm radius and 4 pF capacitance. The buttons are spaced with a distance to the beam of 20 mm. The sensitivities for both vertical and horizontal directions will be established during preliminary design.
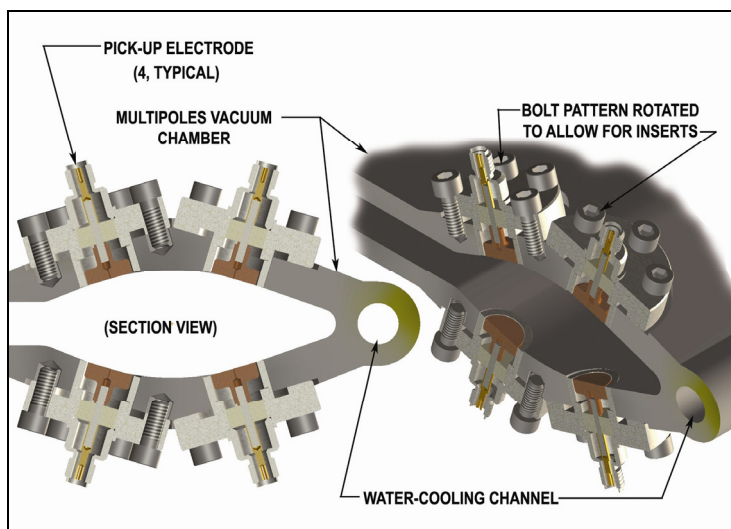
**Figure 7.8.7**   Four-button, two-plane pick-up electrodes mounted on the vacuum chamber.

Libera Electronic Modules, manufactured by I-Tech [7.8.3, 7.8.4], will process the signal from the BPM buttons. The RMS uncertainty of the beam position is 0.2 µm in 1 kHz bandwidth for the buttons placed on

the 10 mm radius. The digital design of the modules provides the possibility of turn-to-turn beam position measurements with 10 μm accuracy.

The chamber with BPM buttons will be mounted on a girder by precisely machined supports, to provide high stability. Small alignment errors as well as electrical offsets and errors in the BPM system will be accounted for at the commissioning using beam-based alignment, which is straightforward due to the individual power supplies.

The NSLS-II storage ring utilizes very strong sextupoles. This makes it very important to have the orbit of the circulating beam as close as possible to the magnetic centers of the sextupoles. We will rely on highly accurate relative alignment of the sextupoles and quadrupoles on the same girder. In addition, a beam-based alignment procedure will be used for the sextupoles.

Figure 7.8.8 Design of the BPM button for the storage ring.
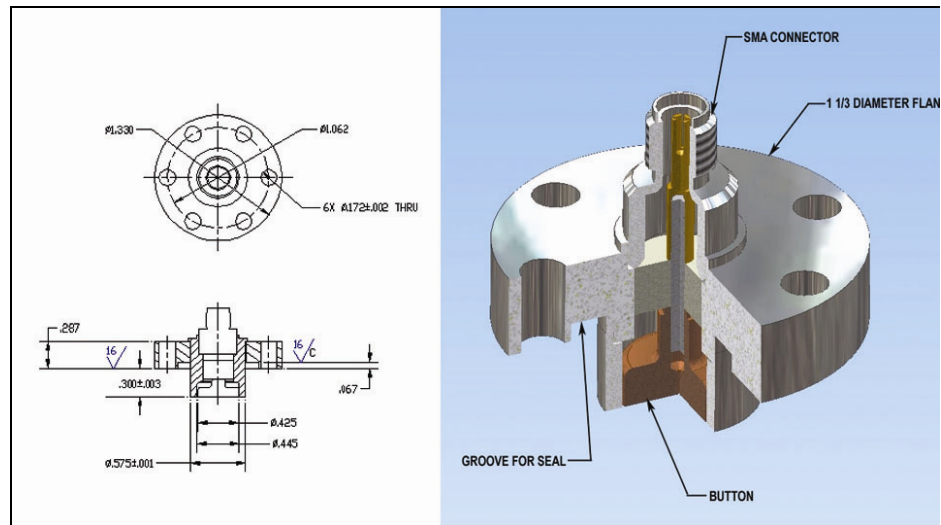
7.8.5.2   Tune Monitor

The vertical and horizontal betatron tunes will be monitored using a network analyzer [7.8.5, 7.8.6]. The analyzer's source will be connected to the excitation striplines through a buffer amplifier. The signal from the receiver striplines will be combined with hybrids to produce vertical or horizontal signals, which will be down converted below the revolution frequency and fed to the input of the network analyzer. Such an approach allows utilization of the maximal driving strength and sensitivity of the striplines and makes measurement of the tunes less sensitive to changes in the revolution frequency.
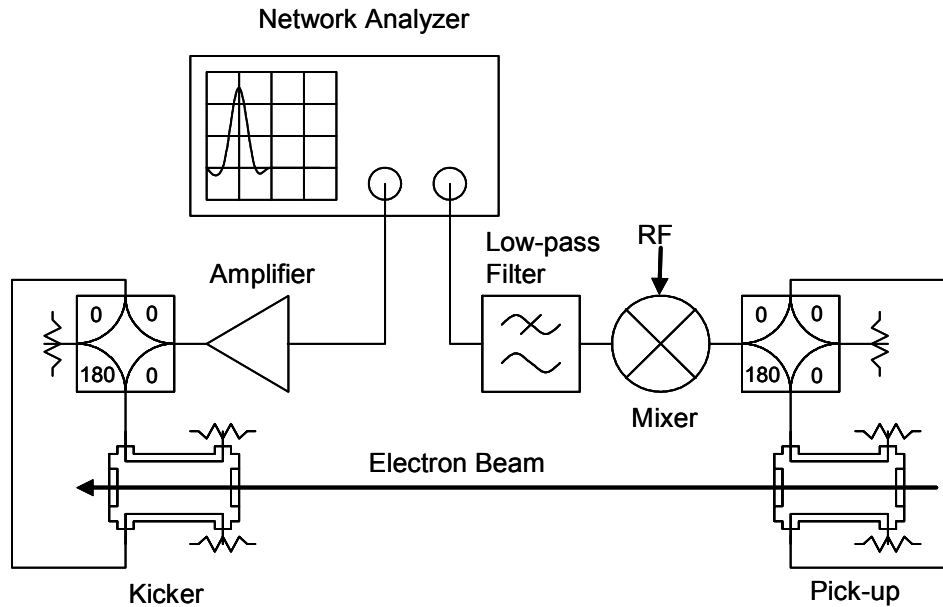
Network Analyzer

Figure 7.8.9 Layout of the tune measurement system.

An alternative solution can utilize a tune tracker (PLL-based) similar to the one utilized at RHIC [7.8.7].

7.8.5.3   Beam Stability Monitoring

The signal from one of the striplines will be connected to an RF spectrum analyzer. The sidebands observed can be used to analyze electron beam stability and find the synchrotron frequency. Summing the signal from opposite striplines helps to eliminate components with transverse oscillations, while maintaining the signal with phase motion of the electron bunches. The difference signal will be used to observe transverse oscillations of the electron beam.
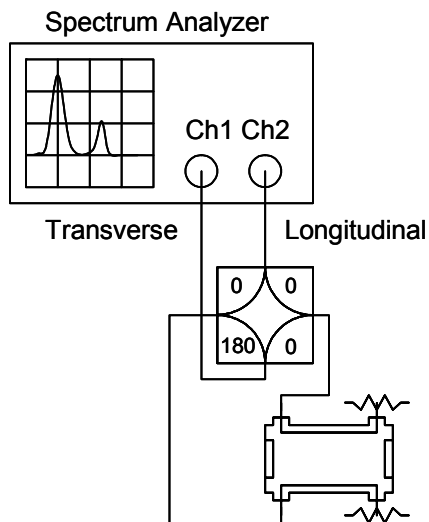
Spectrum Analyzer

Figure 7.8.10 System for the observation of beam stability.

7.8.5.4   Transverse Feedback System

The resistive wall wake can make the electron beam in the storage ring unstable. Increasing the chromaticity may not be sufficient, due to limitations on sextupole strength resulting from loss of dynamic aperture required for beam lifetime and injection. The required stability can be provided by a digital bunch-by-bunch transverse feedback system [7.8.8, 7.8.9]. A broadband signal measuring the position of the individual bunches will be provided by a stripline pick-up. It will be sampled with a fast ADC (sampling rate 500 MHz). A digital filter will calculate the desired correction signal, which is generated by a DAC. The correction kicks are fed through a broadband amplifier and drive the electron beam using the second stripline.
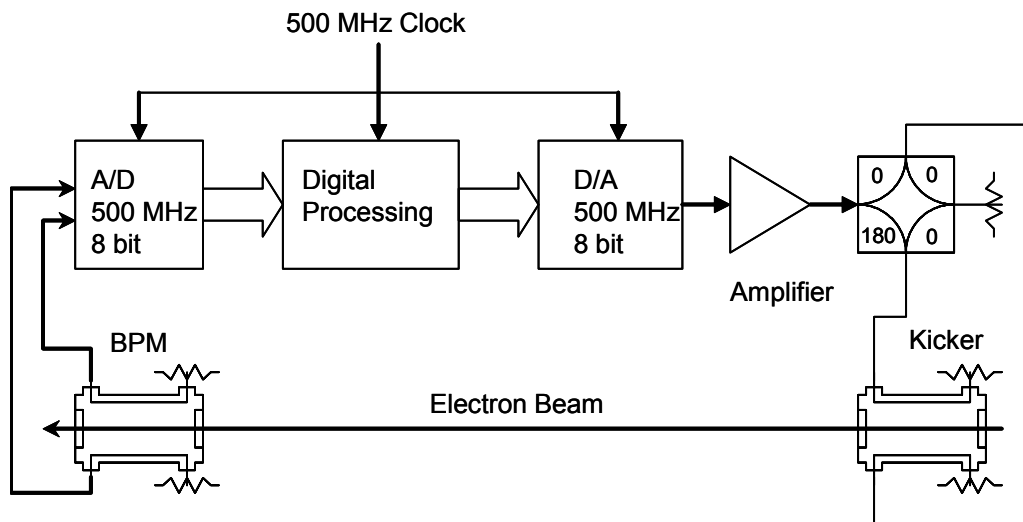

Figure 7.8.11   Conceptual layout of the transverse feedback system.

7.8.6   Synchrotron Radiation Diagnostics

7.8.6.1   Overview

This section describes diagnostics for the NSLS-II storage ring that utilize visible and x-ray synchrotron radiation generated in a bending magnet and an x-ray undulator. Table 7.8.2 shows the types and quantities of diagnostics for the storage ring.

Table 7.8.2 Complement of the Optical Diagnostics for the NSLS-II Storage Ring.

Monitor type	Quantity	Function	Range	Resolution	Bandwidth
Two slit optical interferometer	1	Horizontal emittance Vertical emittance	2.5 nm-rad 8 pm-rad	5 pm-rad 1 pm-rad	100 Hz
Streak-camera	1	Bunch length	10 – 50 ps	2 ps	8 Hz
Photon BPM	2 per beamline	Angle and position of ID radiation	10 mm	0.01 mm	1 Hz
Diagnostics undulator with pinhole camera	1	Horizontal emittance energy spread momentum compaction factor	0.5 – 2.5 nm-rad 0.2 – 2% 10^{-4}		
FireWire camera	1	Beam profile		640x480	120 fps

7.8.6.2   Two-Slit Optical Interferometer

For measuring the ultra low vertical emittance of the storage ring, we plan to use the interferometric method developed at KEK [7.8.10] for measuring ultra small beam sizes. Visible or UV light emitted by the circulating beam passes through a pair of slits separated by distance D and placed at distance L from the source. A lens is used for focusing the diffracted beam on a camera to observe the interference pattern in the far field region. A narrowband filter selects the observation wavelength, λ. The optical set-up is shown in Figure 7.8.12. Due to the non-zero beam size σ, the observed intensity profile will be constructed from the interference patterns coming from the different angles.

Figure 7.8.12   Layout of emittance monitor utilizing a two slit interferometer. Vertical slits are used for horizontal emittance measurement and horizontal slits are used for vertical emittance measurement. A water cooled mirror is needed to avoid exposure of the image sensors to x-rays.
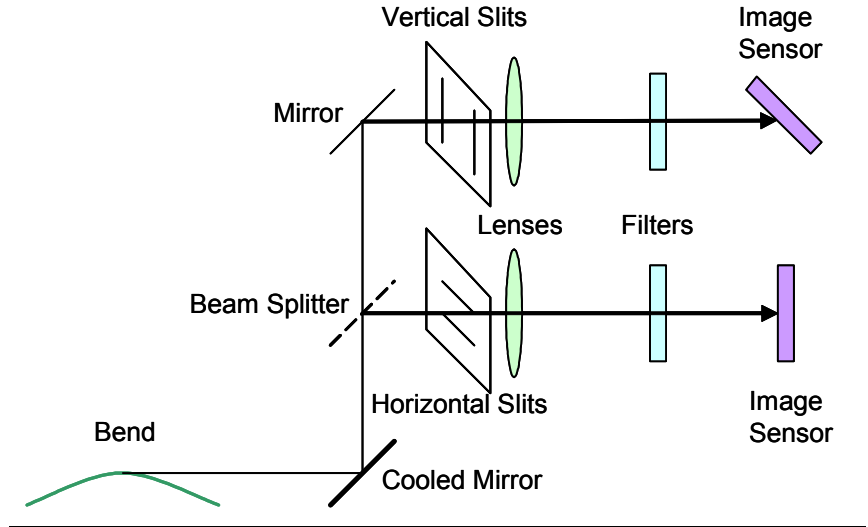
The interference visibility $V = \dfrac{I_{\max} - I_{\min}}{I_{\max} + I_{\min}}$ is given by the formula [7.8.10]:

$$V = e^{-2\pi^2 (D\sigma / L\lambda)^2}$$

(7.8-1)

For synchrotron radiation from the bending magnet, in the vertical plane with a slit width, D, of 16.6 mm and placed at distance L, of 5 m from the source, with observation wavelength, λ, 250 nm, the visibility, V, is expected to be 0.5 for 8 pm-rad vertical emittance and $\beta_y = 25$ m. The calculated intensity profile is shown in Figure 7.8.13. In such conditions, 5% accuracy in the measurement of visibility gives 7% precision of the beam size (and hence emittance) measurements.

Figure 7.8.13 Calculated profile of the intensity of diffracted light for 1 mm slits. Observation plane is 5 m away from the slits.
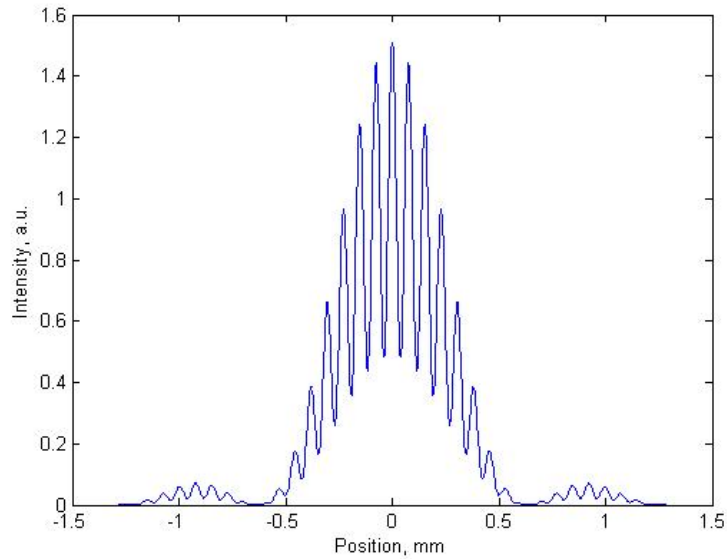
7.8.6.3 Bunch Length Measurement

A double-sweep streak-camera Hamamatsu model C5680 [7.8.11], shown in Figure 7.8.14, will be used to measure the longitudinal beam dynamics. Its versatility and high sensitivity make it an excellent choice for monitoring the bunch length with sub-picosecond resolution and studying beam instabilities. The streak camera will be equipped with A1976-01 input optics with an N5716 streak tube. The parameters are shown in Table 7.8.3. The synchroscan feature provides low-phase jitter for synchronous summing of signals and tracking phase dynamics.

Table 7.8.3 C5860 Streak Camera Parameters.

Spectral response characteristics [nm]	200 to 850
Minimal radiant sensitivity [mA/W]	2 at 240 nm, 1 at 820 nm
Synchroscan frequency (factory setting) [MHz]	100
Temporal resolution at 800 nm (FWMH) [ps]	2
Sweep range	200 ps to 1/6Fs (Fs is synchroscan frequency)
Dual time sweep range [s]	10^{-7} to 10^{-1}
Camera resolution [pixels]	1280x1024
Frame rate [Hz]	8
Dynamic range [bit]	12

The streak camera will be shared with the booster. An optical beamline from the booster will be used to transport a beam of synchrotron radiation from the booster bending magnet to the streak camera.

Figure 7.8.14   View of the C5860 streak camera.

7.8.6.4   Photon Beam Position Monitors

Photon beam position monitors similar to the ones used at APS as shown in (Figure 7.8.15) will be used for monitoring radiation from the insertion devices [7.8.12]; the blades, of course, will be designed and optimized to suit the requirements of NSLS-II. The information obtained on the angle and position of the photon beam will be incorporated into the orbit feedback system to provide the beam stability required for user applications. Two photon BPMs will be used for each beamline. The BPM assembly will be mounted on a stable post and its location (elevation and transverse position) will be adjusted with 2D translation stages. Utilizing such devices has been shown to enable pointing stability of the photon beam with peak-to-peak drift of less than 2 µrad over six days [7.8.12].
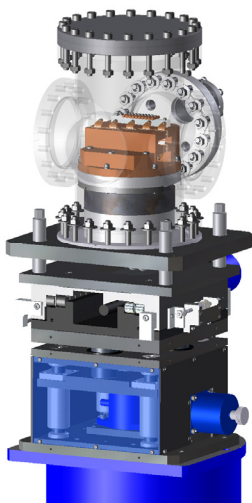

Figure 7.8.15   APS Photon beam position monitor.

7.8.6.5   Optical Synchrotron Radiation

An IEEE1394 camera will be used for observation of the OSR from the electron beam. Such an approach eliminates the need for a frame-grabber and makes display of the beam on the control computer straightforward. The camera has an external trigger capability and exposure control from 10 µsec to 5 sec.

Position sensitive photodiodes that provide signal depending on the location of the center of gravity of the optical beam, can be incorporated into the orbit feedback system as well as results of image processing. The model S2044 (in the right bottom corner of Figure 7.8.16) has 0.6 µm sensitivity and 0.3 µsec rise time. They will be used to monitor beam stability for the IR users.

Figure 7.8.16   Position-sensitive diodes by Hamamatsu.
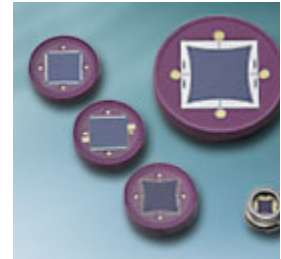
7.8.6.6   Diagnostics Undulator

The diagnostics undulator will allow independent measurement of the energy spread and horizontal emittance. The momentum compaction factor can be also measured. We plan to utilize one of the user beamline undulators in a 5 m straight. This beamline will be equipped with an additional high resolution fluorescent screen and a retractable pinhole (Figure 7.8.17). Use of the radiation from this undulator for diagnostic purposes will be restricted to periods when it is not needed by the users.
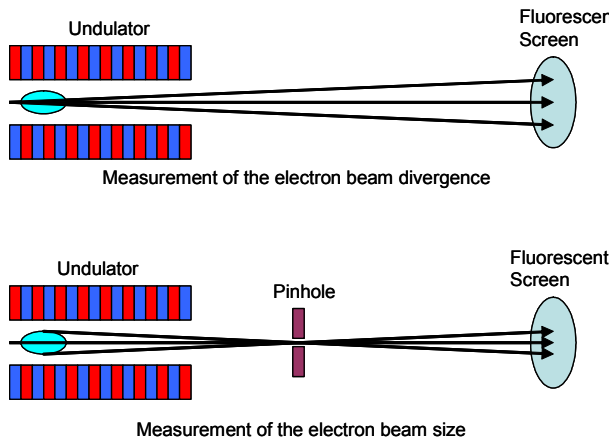

Undulator · Fluorescer Screen
Measurement of the electron beam divergence

Figure 7.8.17   Beam diagnostics with undulator radiation.

Undulator · Pinhole · Fluorescent Screen
Measurement of the electron beam size

The β-functions in the straight are $\beta_{xmin} = 2.5$ m and $\beta_{ymin} = 1.0$ m. The U19 undulator, proposed for usage, has 19 mm period and 3 m length.

For measuring the divergence of the electron beam, the transverse profile of the undulator radiation will be obtained. In order to increase the system resolution, small undulator K values will be utilized. These will also help to keep the power from higher harmonics low and avoid distortion of the power profile. For $K = 0.3$, the power density of the 3rd harmonic is two orders of magnitude below the power density of the main harmonic. For this value of K, the fundamental wavelength of the undulator radiation will be 0.29 nm and the

divergence due to a diffraction will be $\sigma'_{ph} = \sqrt{\lambda/L} = 9.8\,\mu\text{rad}$, which compares favorably with the horizontal divergence of the electron beam $\sigma'_e = \sqrt{\varepsilon_x/\beta_x} = 14.1\,\mu\text{rad}$ for 0.5 nm-rad emittance.

Inserting a pinhole, which can be realized as a slit, will allow measurement of the horizontal beam size. Knowledge of the divergence and beam size gives one the ability to measure directly the beam emittance (independent of the β-function).

Analysis of the width of the undulator spectrum provides information on the energy spread of the electron beam. It is also possible to measure the momentum compaction factor by observing the shift of the undulator spectrum with revolution frequency [7.8.13].

7.8.7   Other Diagnostics

7.8.7.1   Beam Loss Monitors

NSLS-II will utilize a distributed beam loss monitoring system based on pin-diodes, which are commercially available from Bergoz [7.8.2] (Figure 7.8.18). At least two beam loss monitors per beamline will be used for interlocks. This feature is especially important for the mini-gap undulators.

Figure 7.8.18   Beam loss monitor by Bergoz.

The loss monitors have a pulse output (one pulse per lost particle) and are insensitive to the synchrotron radiation photons. The monitors are small and can be easily relocated to the region of interest.

7.8.7.2   RF Frequency Monitor

Signal from the RF master oscillator will be provided to a counter in order to monitor the revolution frequency.

7.8.7.3   Scrapers

Two pairs of two-plane adjustable-position scrapers will be installed on the ring to be used both as protective devices as well as diagnostic instruments for accelerator studies. More details are described in Section 7.7.

One set of scrapers (horizontal and vertical) will be installed in the dispersive section to measure the energy distribution of the electron beam. Another set will be installed in a straight section with zero dispersion in order to have information on the transverse size of the electron beam and eliminate possible beam halos capable of affecting the insertion devices.

7.8.7.4   High-Level Accelerator Modeling

High level accelerator modeling required to extract data on the storage ring lattice from the experimental data [7.8.14]. It is described in the control system section. It will be also used for the development of real time orbit feedback system and coupling correction.

References

[7.8.1]   E.D. Johnson, W.S. Graves, and K.E. Robinson, "Periscope Pop-In Beam Monitor," Proc. of Beam Instrumentation Workshop 1998, AIP Conf. Proc. 451, pp. 479–484.

[7.8.2]   http://www.bergoz.com

[7.8.3]   R. Ursic et al., "Holy Trinity of the Instrumentation Development," Proc. of the 11th Beam Instrumentation Workshop, Knoxville 2004.

[7.8.4]   U. Mavric, "Innovative RF Design Unites Benefits of Multiplexed and Multichannel System," Proc. of the 11th Beam Instrumentation Workshop, Knoxville, 2004.

[7.8.5]   A.S. Fisher, "Instrumentation and Diagnostics for PEP-II," Proc. Beam Instrumentation Workshop 1998, AIP Conf. Proc. 451, pp. 95–109.

[7.8.6]   A. S. Fisher, M. Petree, U. Wienands, S. Allison, M. Laznovsky, M. Seeman, and J. Robin, "Upgrades to PEP-II Tune Measurements," Proc. of Beam Instrumentation Workshop 2002, AIP Conf. Proc. 648, pp. 267–274.

[7.8.7]   T. M. Brennan, P. Cameron, P. Cerniglia, R. Connolly, J. Cupolo, W. Dawson, C. Degen, A. DellaPenna, J. DeLong, A. Drees, D. Gassner, M. Kesselman, R. Lee, A. Marusic, J. Mead, R. Michnoff, C. Schultheiss, R. Sikora, and J.Van Zeijts, "Tune Measurement in RHIC," Proc. Beam Instrumentation Workshop 2002, AIP Conf. Proc. 648, pp. 134–149.

[7.8.8]   M. Dehler, R. Kramert, P. Pollet, and T. Schilcher, "Commissioning Results of the Multi Bunch Feedback System at SLS," Proc. of EPAC 2004, pp. 2508–2510.

[7.8.9]   S.N. Thanos and R. H. Hosking, "ELETTRA Photon Source Beam Stabilization," Proc. Beam Instrumentation Workshop 2002, AIP Conf. Proc. 648, pp. 248–253.

[7.8.10]   T. Mitsuhashi, "Measurement of Small Transverse Beam Size Using Interferometry," Proc. of DIPAC 2001, pp. 26–30.

[7.8.11]   http://www.hamamatsu.com

[7.8.12]   G. Decker and O. Singh, "Beam Stability at the Advanced Photon Source," Proc. of PAC 2005, pp. 3268–3270.

[7.8.13]   B. Yang, M. Borland, and L. Emery, "High Accuracy Momentum Compaction Measurement for the APS Storage Ring with Undulator Radiation," CP546, Beam Instrumentation Workshop 2000, American Institute of Physics, pp. 235–241.

[7.8.14]   J.A. Safranek, "Beam-based Accelerator Modeling and Control," Proc. of Beam Instrumentation Workshop 2000, AIP Conf. Proc. 546, pp. 23–5.